

University of Windsor

## Scholarship at UWindor

---

Electronic Theses and Dissertations

Theses, Dissertations, and Major Papers

---

2016

### Characterization of thermal spray coatings on aluminum engine bore

Jianping Zou  
*University of Windsor*

Follow this and additional works at: <https://scholar.uwindsor.ca/etd>

---

#### Recommended Citation

Zou, Jianping, "Characterization of thermal spray coatings on aluminum engine bore" (2016). *Electronic Theses and Dissertations*. 5777.

<https://scholar.uwindsor.ca/etd/5777>

This online database contains the full-text of PhD dissertations and Masters' theses of University of Windsor students from 1954 forward. These documents are made available for personal study and research purposes only, in accordance with the Canadian Copyright Act and the Creative Commons license—CC BY-NC-ND (Attribution, Non-Commercial, No Derivative Works). Under this license, works must always be attributed to the copyright holder (original author), cannot be used for any commercial purposes, and may not be altered. Any other use would require the permission of the copyright holder. Students may inquire about withdrawing their dissertation and/or thesis from this database. For additional inquiries, please contact the repository administrator via email ([scholarship@uwindsor.ca](mailto:scholarship@uwindsor.ca)) or by telephone at 519-253-3000ext. 3208.

Characterization of thermal spray coatings on aluminum engine bore

By

Jianping Zou

A Thesis

Submitted to the Faculty of Graduate Studies  
through Mechanical, Automotive & Materials Engineering  
in Partial Fulfillment of the Requirements for  
the Degree of Master of Applied Science  
at the University of Windsor

Windsor, Ontario, Canada

2016

© 2016 Jianping Zou

# Characterization of thermal spray coatings on aluminum engine bore

By

Jianping Zou

APPROVED BY:

---

M. Mirhassani

Department of Electrical and Computer Engineering

---

H. Hu

Department of Mechanical, Automotive and Materials Engineering

---

A. Edrisy, Advisor

Department of Mechanical, Automotive, and Materials Engineering

May 26 2016

## **DECLARATION OF CO-AUTHORSHIP**

I hereby declare that this thesis incorporates material, which is an outcome of a joint venture undertaken in collaboration with Ben Slattery from Fiat Chrysler Automobiles and the University of Windsor's Department of Mechanical, Automotive and Materials Engineering, under the supervision of Dr. A. Edrisy. The collaboration is covered in Chapters 3, 4 and 5 of this thesis.

I am aware of the University of Windsor Senate Policy on Authorship and I certify that I have properly acknowledged the contributions of other researchers to my thesis and have obtained permission from each of the co-authors to include the above materials in my thesis.

I certify that, with the above qualification, this thesis and the research to which it refers, is the product of my own work. I declare that, to the best of my knowledge, my thesis does not infringe upon anyone's copyright nor violate any proprietary rights and that any ideas, techniques, quotations, or any other material from the work of other people included in my thesis, published or otherwise, are fully acknowledged in accordance with the standard referencing practices. Furthermore, to the extent that I have included copyrighted material that surpasses the bounds of fair dealing within the meaning of the Canada Copyright Act, I certify that I have obtained a written permission from the copyright owner(s) to include such material(s) in my thesis.

I declare that this is a true copy of my thesis, including any final revisions, as approved by my thesis committee and the Graduate Studies office and that this thesis has not been submitted for a higher degree to any other University or Institution.

## **ABSTRACT**

Plasma transferred wire arc (PTWA) process was employed to deposit wear resistance coating (approximate 240  $\mu\text{m}$ ) on the aluminum engine bore surface. The PTWA coating has a lamellae structure with splats, pores, oxides, and unmelt particles. The volume fraction of porosity was 5.8 %.

The coated bore was subjected to non-firing floating-liner test. Cast iron bore was tested for comparison purposes. The friction force of the coated engine bore was recorded lower than that of cast iron engine bore.

The surface and cross-sectional microstructural analysis was performed at TDC and mid-stroke after the engine tests. The unworn region (virgin) was analyzed for comparison to determine the wear mechanisms. Abrasive wear and splat delamination contributed the wear of aluminum engine bore with the PTWA coating. Adhesion tests were performed on virgin part. A cohesion strength of 19.51 MPa and a adhesion strength of 29.03 MPa were recorded.

## **DEDICATION**

I dedicate this thesis to my loving parents and my husband for their support and unconditional love.

I dedicate this thesis work to my advisors Dr. A. Edrisy for her support and guidance in my research career.

## **ACKNOWLEDGEMENTS**

I would like to give special thanks to my advisor Dr. A. Edrisy for her supervision throughout the entirety of this project and for her guidance through this endeavor.

I also would to thank my committee members, Dr. Hu and Dr. Mirhassani for their comments in improving my research.

Many thanks to Ben Slattery from Fiat Chrysler Group for supporting this research and my colleagues in Dr. Edrisy's group for help in my research.

## TABLE OF CONTENTS

DECLARATION OF CO-AUTHORSHIP.....	iii
ABSTRACT.....	iv
DEDICATION.....	v
ACKNOWLEDGEMENTS.....	vi
LIST OF FIGURES.....	ix
LIST OF TABLES.....	xiii
LIST OF ABBREVIATIONS AND SYMBOLS.....	xiv
CHAPTER 1 INTRODUCTION.....	1
CHAPTER 2 LITERATURE SURVEY.....	4
2.1 Plasma transferred wire arc thermal spray coating deposition process.....	4
2.1.1 General introduction of thermal spray coating deposition processes...	4
2.1.2 Plasma transferred wire arc process.....	8
2.1.3 Application processes of PTWA coating.....	16
2.1.4 Parameters that influence the PTWA coating performance.....	23
2.2 Coating Properties.....	28
2.2.1 Microstructures.....	29
2.2.2 Mechanical properties.....	31
2.3 Wear mechanism.....	33
2.3.1 Introduction of wear modes.....	33
2.3.2 Introduction of lubrication.....	35
2.3.3 Wear behavior of thermal spray coatings.....	39
2.3.4 Internal Combustion Engine.....	41
2.3.5 Operating principles of the internal combustion engine.....	42
2.3.6 Piston assembly.....	43
2.3.7 Engine wear.....	45
CHAPTER 3 MATERIAL AND EXPERIMENT PRODUCERS.....	47
3.1 Materials.....	48
3.1.1 Plasma transferred wire arc (PTWA) coating on A380 aluminum bore	49
3.1.2 Cast iron bore.....	49
3.1.3 Plasma transferred wire arc (PTWA) coating on aluminum bore with different surface preparation.....	50
3.2 Optical surface profilometer.....	51
3.3 Non-firing floating-liner tests.....	53
3.4 Cross-Sectional preparation for microstructural observation.....	54
3.5 Microstructural analysis.....	56
3.5.1 Cross-sectional microstructure.....	56



3.5.2	Volume fraction of porosity within the coating .....	56
3.6	Hardness Evaluation.....	58
3.7	Adhesion Evaluation.....	58
CHAPTER 4	EXPERIMENTAL RESULTS .....	61
4.1	Optical surface profilometer results .....	61
4.1.1	Surface morphology .....	61
4.1.2	Surface roughness .....	64
4.1.3	Surface pore analysis for PTWA- A coating engine bore.....	65
4.1.4	Oil retention volume of the cast iron sample and the PTWA-A coating 69	
4.1.5	Surface morphology and surface roughness for PTWA-B coating .....	71
4.2	Non-firing floating-liner tests.....	73
4.3	Microstructural analysis .....	74
4.3.1	Surfaces before and after the non-firing floating-liner tests .....	74
4.3.2	Cross-sectional microstructure results of PTWA-A coating engine bore 79	
4.3.3	Cross-sectional microstructure results of cast iron.....	85
4.3.4	Surface and cross-sectional microstructure analysis for PTWA-B coating 87	
4.4	Hardness tests .....	95
4.5	Adhesion tests .....	95
CHAPTER 5	DISCUSSION .....	98
5.1	Sliding Behavior of PTWA-A coating engine bore in comparison with Cast Iron engine bore.....	98
5.1.1	Wear mechanism.....	100
5.1.2	Lubrication conditions .....	103
5.2	Evaluation of adhesion strength .....	104
CHAPTER 6	CONCLUSIONS.....	106
6.1	Conclusions .....	106
6.2	Recommendations for future research.....	108
REFERENCES	.....	109
VITA AUCTORIS.....		113

## LIST OF FIGURES

Figure 2-1 History a of thermal spray industry [7] .....	5
Figure 2-2 Industrial applications of thermal spray technology in Europe in 2001[10] ..	6
Figure 2-3 Principle of thermal spray process [13] .....	7
Figure 2-4 Schematic representation of plasma spray process [7].....	10
Figure 2-5 Schematic diagram of a plasma torch [7] .....	12
Figure 2-6 Schematic diagram of wire arc spray process [7] .....	13
Figure 2-7 (a) Plasma sprayed system [29]; (b) Plasma transferred wire arc system and schematic diagram of PTWA process [17]. .....	16
Figure 2-8 Micrograph of a 0.82% C-steel coating applied with the PTWA system. In the figure, the oxide phases appear darker than the Fe matrix [18] .....	31
Figure 2-9 Specimen arrangement and possible failure modes for tensile adhesion tests [23].....	33
Figure 2-10 Effects of viscosity, velocity and load on the coefficient of friction [39] ...	36
Figure 2-11 Elastic distortion of a sphere (shown exaggerated for clarity) under combined normal load and sliding motion [42].....	38
Figure 2-12 Main engine components in an internal combustion engine [39] .....	41
Figure 2-13 The Otto cycle of four stroke engine [39].....	43
Figure 2-14 Piston assembly and piston ring function from an internal combustion engine [37] .....	44
Figure 3-1 Flow chart illustrating the methodology used for engine bore characterization .....	47
Figure 3-2 The Schematic illustrating the mechanical interlock after surface activation .....	48
Figure 3-3 The Schematic illustrating the fabrication of the engine bores before and after applying PTWA coatings .....	49
Figure 3-4 The Schematic illustrating the surface inspection locations at (a) TDC and (b) mid-stroke respectively (provided by NanoFocus) .....	52
Figure 3-5 Sample section: (a) the main sides of an engine bore after non-firing floating-liner test; (b) the samples sectioned for further microstructural analysis, worn and unworn surface comparison; the area of each sectioned sample was 10 mmx20 mm .....	55
Figure 3-6 Example of binary mask of coating cross-section containing 2.0 % porosity by area [53] .....	57
Figure 3-7 Schematic illustration showing the adhesion test modification for surfaces with curvature [23][55] .....	59
Figure 3-8 Schematic graph for the curved sample glued to the sample holders.....	60
Figure 4-1 Unworn surface morphology of the cast iron sample at (a) TDC; (b) Mid- stroke, showing the presence of pores and honing marks .....	62
Figure 4-2 Worn surface morphology of the cast iron sample at (a)TDC; (b)Mid-stroke, showing the presence of pores, honing marks and wear scars .....	62
Figure 4-3 Unworn surface morphology of the PTWA-A coating sample at (a)TDC; (b)Mid-stroke, showing the presence of pores, honing marks and wear scars.....	63

Figure 4-4 Worn surface morphology of the PTWA-A coating sample at (a) TDC; (b) Mid-stroke, showing the presence of pores, honing marks and wear scars .....	63
Figure 4-5 Surface roughness results of the PTWA-A coating engine bore.....	64
Figure 4-6 Surface roughness results of the cast iron engine bore .....	65
Figure 4-7 Average number of pores for the PTWA-A coating sample .....	66
Figure 4-8 Average pore area ( $\mu\text{m}^2$ ) of the PTWA-A coating sample .....	67
Figure 4-9 Average pore volume ( $\mu\text{m}^3$ ) of the PTWA-A coating sample .....	68
Figure 4-10 Average pore depth ( $\mu\text{m}$ ) of the PTWA-A coating sample .....	68
Figure 4-11 Oil retention volume ( $\text{ml}/\text{m}^2$ ) of the cast iron sample after non-firing floating-liner test.....	70
Figure 4-12 Oil retention volume ( $\text{ml}/\text{m}^2$ ) of the PTWA-A coating sample after non-firing floating-liner tests.....	71
Figure 4-13 (a) A typical 2D profile of the PTWA-B coating surface showing presence of pores and honing marks, (b) several line profiles collected from the same area based on which the pore depth values were calculated. ....	72
Figure 4-14 Surface roughness results of the PTWA-B coating .....	73
Figure 4-15 Average Friction Force Results: Time History .....	74
Figure 4-16 Mixed SEM image of (a) unworn surface of the PTWA-A coating, (b) unworn surface of the cast iron sample .....	75
Figure 4-17 Detailed SEM images of the worn surface features of the PTWA-A coating: (a) Mixed SEM image shows the worn surface texture of the PTWA-A coating, (b) Back scattered image of the selected area in (a) shows that the surface pores tend to connect with each other and become a large surface defect. (c)BSE image shows the removed wear asperity adhered to the surface. (d)A mixed image shows the beginning of a severe wear scar. (e) BSE image shows a particle scale ready to flake off from the surface (rounded area) and the inside material was forced out of the surface resulting in deep and wide wear scars .....	77
Figure 4-18 Selected area for EDS analysis (b) elements mapping results; (c) result of EDS elements analysis of the selected area.....	78
Figure 4-19 Detailed SEM images of the worn surface features of the cast iron sample: (a) The worn surface of the cast iron showing wear direction, honing marks and wear scar started away from the honing grooves or surface pores, (b) The worn surface of the cast iron showing surface pores, micro cracks and the pile-up of the materials.....	79
Figure 4-20 OM image shows the cross-sectional view of the unworn PTWA-A coating .....	80
Figure 4-21 Back-scattered images giving detailed information of the cross-section microstructure of the PTWA-A coating at virgin region .....	81
Figure 4-22 (a) Selected area of the virgin part for EDS analysis (b) oxide concentration results (c) result of EDS elements analysis of the selected area around the central pore .....	82
Figure 4-23 (a) OM cross-sectional view of the PTWA-A coating at TDC, (b) magnified view of the selected area showing the presence of oxides, pores, lamellae and micro-cracks .....	83

Figure 4-24 (a) Selected areas for EDS analysis (b) oxide concentration results (c)(d) results of EDS elements analysis of the selected area 1 and selected area 2 respectively ..... 84

Figure 4-25 OM images showing cross-section microstructure of the PTWA-A coating at mid-stroke :( a) the surface defects as well as a crack propagated along the semi lamellae; Additionally, pores and micro-cracks are obvious within the coating. (b) The growing of a surface pore, in which the inside material was trying to escape out of the pore. (c) The magnified view of a half delaminated semi lamellae near the surface. (d) the result of the height scanning of (c), showing the semi lamellae near the surface was half delaminated.(e) The magnified view of several half delaminated semi lamellae near the surface. (f) The result of the height scanning of (e), proving the semi lamellae near the surface was half delaminated ..... 85

Figure 4-26 BSE images showing the cross-section microstructure of the cast iron sample (a) at virgin showing typical cast iron features while the surface is uniform; (b) at TDC, showing fractures happened along the intersection of graphite and surface; (c) Magnified view of the fracture at TDC in selected area; (d) at mid-stroke showing material deformation at graphite; (e) magnified view of material deformation on the surface of worn cast iron at the mid-stroke in selected area. .... 87

Figure 4-27 (a) A typical secondary electron (SE) image of the surface of the PTWA-B coating showing presence of hone marks and surface porosity. The enclosed location marked as “l” is where the higher magnification images shown in Figure 4-30 were taken (b) A back-scattered electron (BSE) image of the same area shown in Figure 4-28 (a) illustrating band contrast and floret-like structure which indicates presence of two different phases in the coating (light grey and dark grey regions)..... 88

Figure 4-28 (a) Back-scattered electron (BSE) image of the enclosed area marked as “l” in Figure 2 showing the morphology of on the surface of the PTWA-B coating, the enclosed area is the location where higher magnification image shown in “b” was taken. (b) A back-scattered electron (BSE) image of the enclosed area marked in “a” showing presence of unmelted particles within this region. (c) A 3D-optical profile of the area selected in “a” ..... 90

Figure 4-29 Back-scattered electron (BSE) image of the surface: The enclosed areas are the locations where elemental analyses (e.g., x-ray energy dispersive spectrometry (EDS)) was performed. (b) EDS spectrum collected from “selected area 1” and “selected area 3” showing abundance of iron and presence of carbon in these regions. (c) EDS spectrum corresponding to “selected area 2” showing abundance of iron and oxygen and presence of carbon in this region ..... 91

Figure 4-30 (a) A typical secondary electron (SE) image of the honed surface of the coating showing presence of cutting chip-like features and micro cracks. The enclosed area is the location where higher magnification image shown in “b” was taken. (b) SE image of the area marked in “a” showing the cutting chip-like features on the honed surface..... 92

Figure 4-31 (a) Cross-sectional back-scattered electron SEM images of the PTWA-B coating on the Al substrate: The coating had a dovetail morphology interface with the aluminum substrate. The layered structure of the coating is evident from the images (b) presence of unmelted particles, porosity and dark grey veins in the intersplat regions, (c) presence of micro cracks within the dark grey phase in the intersplat region ..... 93

Figure 4-32 (a) A cross-sectional microstructure (back-scattered SEM image) of the PTWA-B coating, (b) corresponding energy dispersive x-ray spectroscopy (EDS) map of the same area showing that the light areas were rich in iron and the dark grey regions consisted of oxygen. (c), (d) Typical EDS spectra of the O-rich (blue) and Fe-rich (red) regions indicating that the O-rich veins consisted of iron oxides and the Fe-rich regions were steel splats ..... 94

Figure 4-33 Stereo micrographs taken from the failure surfaces of the PTWA-B coating. (a) Top view of the failed surface showing the keyhole pattern made on aluminum prior to the deposition of the PTWA-B coating, (b) side view of the failed surface showing the detachment of the PTWA-B coating from the substrate at the coating/substrate interface; (c) a high magnification view of the failed surface shown in “b” illustrating the detachment of the coating at the aluminum substrate interface and the keyhole pattern made on the Al surface prior to the coating deposition..... 97

Figure 4-34 Adhesive failure surface of PTWA-A coating: (a)Top view of the failed surface, (b) side view of the failed surface showing the coating/substrate interface ..... 97

Figure 4-35 Cohesive failure surface of PTWA-A coating (a) Top view of the failed surface showing the failure on PTWA-A coating, (b) side view of the partial detachment of the PTWA-A coating from the substrate ..... 97

**LIST OF TABLES**

Table 2-1 Powder materials used in actually thermal spray application [13] ..... 8  
Table 2-2 Properties of the main grit materials [8]..... 19  
Table 3-1 Mechanical comparison of cast iron and A380 aluminum alloy [50][56] ..... 50  
Table 3-2 Information of specimens to be investigated ..... 50  
Table 3-3 Conditions attempted to find the optimum conditions for curing the FM1000  
adhesive film ..... 60  
Table 4-1 Results of adhesion pull tests..... 96

## **LIST OF ABBREVIATIONS AND SYMBOLS**

ASTM	American Society for Testing and Materials
BSE	backscattered electron
EDS	energy dispersive spectroscopy
OM	optical microscopy
PTWA	Plasma transferred wire arc
SE	secondary electron
SEM	scanning electron microscopy
Sk	core roughness depth
SpK	reduced peak height
SvK	reduced valley depth
TDC	top dead center

# CHAPTER 1 INTRODUCTON

The development of lightweight internal combustion aluminum-silicon engines represents one of the most significant technological developments in the automotive industry because, when compared to traditional cast iron engines, they are lighter and consume less oil. Using cast aluminum alloys components to replace the traditional cast iron components has become increasingly popular and replacing cast iron with aluminum for engine cylinder blocks has the potential for a sizable reduction in block weight: up to 45% [1]. However, limitations such as low wear resistances, low Young's modulus, low tensile strength and low hardness prevents the further application of cast aluminum parts in moving components [2]. In order to provide a suitable cylinder running surface, thick coats are applied to the engine bore surface. Coatings improve functional performance by allowing higher exposure temperature. They are referred to as thermal barrier coatings. The application of thermal barrier coatings can extend component life significantly by improving the wear resistance property of the engine bore surface. Various technologies are currently employed to provide coatings on the engine bore surface; however, few of them can reduce the overall cost while significantly improving wear resistance property at the same time. Thermal spray coating deposition technologies have found their way into the automotive industry and are common and have an expanding variety of uses because of their low cost and high compatibility. Thermal spray coating deposition technologies can deposit thick coatings ranging from 20 micrometers to several millimetres [3] on a large



area at high deposition rate, which gives them an advantage over other coating deposition processes, such as electroplating, physical vapour deposition and chemical vapour deposition. The coating materials employed in thermal spray deposition process include metals, alloys, ceramics, plastics and composites.

Plasma transferred wire arc (PTWA) process is one of the most commonly used thermal spray process. PTWA is a wire based rotating spray process with a combination of plasma spray process and twin wire arc spray process.

This thesis studies the performance and the wear mechanisms of plasma transferred wire arc (PTWA) coatings applied on engine bore. Plasma transferred wire arc (PTWA) deposition was employed to deposit wear resistant coatings on the aluminum engine bore surfaces to improve the tribological properties of the engine bore surface. The aluminum engine with the PTWA steel coating was investigated to provide a detailed metallographic characterization of the PTWA coating. The surfaces and cross sectional microstructure after non-firing floating-liner tests were analyzed to characterize the wear mechanisms. The adhesion strength of the PTWA coating was also evaluated. The surfaces and cross sectional microstructure of a cast iron engine bore were investigated under the same conditions as a comparison. The adhesion strength of a PTWA coating on BWM engine bore was investigated for comparison.

This thesis contains six chapters. Chapter one gives an introduction for this research. Chapter two focuses offers a literature review on PTWA coating deposition process and the properties of the PTWA coating. The relevant literatures on the internal combustion engine

theory, scuffing behaviour of internal combustion engines and the wear mechanism of thermal spray coatings are also reviewed.

Chapter three illustrates the materials and experimental procedures employed in this work. The experimental procedures that characterize the microstructures and the mechanical properties of the PTWA coatings are presented.

Chapter four describes the results. The surface roughness and porosity analysis of tested PTWA coatings after the non-firing floating-liner tests as well as the non-firing floating-liner tests results are presented, followed by microstructural analysis of unworn and worn region. The adhesion test results are also displayed.

Chapter five discusses the experimental observations. The sliding behaviours of PTWA-A coating engine bore in comparison with cast iron engine bore are discussed to characterize the relationship between the microstructures and wear mechanisms of PTWA coatings.

The conclusions and suggestions for future work are given in Chapter six.

## CHAPTER 2 LITERATURE SURVEY

In this chapter, the existing literature on the introduction of plasma transferred wire arc thermal spray coating deposition technology; the parameters influenced the coating as well as the microstructure of coating are reviewed. Also, the wear mechanisms and failure modes of thermal spray coating are studied. At last but not least, a review of wear of internal combustion engines is also given because the thermal spray coatings are developed for the engines to reduce the weight while keep the wear resistance.

### 2.1 Plasma transferred wire arc thermal spray coating deposition process

#### **2.1.1 General introduction of thermal spray coating deposition processes**

Thermal spray coating deposition technology is a way to offer an effective thick or thin coating upon the surface to change the properties of the surface. Thermal spray is a generic term for a group of coating processes where the coating is deposited on a prepared substrate by applying a stream of particles, metallic or nonmetallic, which flatten more or less to form platelets, called splats. With several layers of these splats the coating formed [4]. The droplets would adhere to the prepared surface, overlap and interlock when solidifying during impacting. The final thickness of coating can be built up through multiple passes of the coating device.

In 1911, M.U. Schoop of Switzerland [5] first invented the flame spray. He and his collaborators made the thermal spray able for commercial and started the investigation of thermal spray processes. Schoop recognized the importance of the droplet velocity and temperature on the coating [5]. Later in 1962, plasma spray was studied by R.M. Gage, O.H. Nestor and D.M. Yenni [6]. Till now, many researchers studied the thermal spray coating deposition technologies. Figure 2-1 [7] showed milestones in the development of the thermal spray industry.

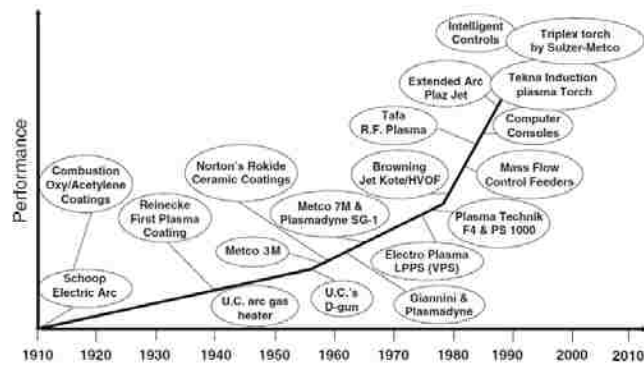


Figure 2-1 History of thermal spray industry [7]

There are many advantages of thermal spray coating processes. Almost any material that melts without decomposing can be used in thermal spray processes [8]. The second is that recoating the damaged surface would not change the properties of coating in most cases [9]. Another advantage is that even high melting point materials can also be applied to finely machined and heat-treated parts without changing the properties [6].

Choosing thermal spray techniques for applications according to a specific condition is complex. Figure 2-2 [10][11] illustrated the industrial applications of thermal spray. The main use of thermal spray coating deposition technologies is offering a protective surface

showing properties of wear resistance, corrosion resistance, thermal insulation and electrically conductive on aerospace, automotive, power and chemical industries [8][9][11][12]. The wear resistant coatings and corrosion resistant coatings are usually used to against erosion, abrasion, cavitation wear, galling, fretting and friction. Coatings can also achieve protection against high-temperature corrosion or oxidation. As listed, thermal spray coating deposition technologies are widely used to reduce the cost while improve the properties of the surface.

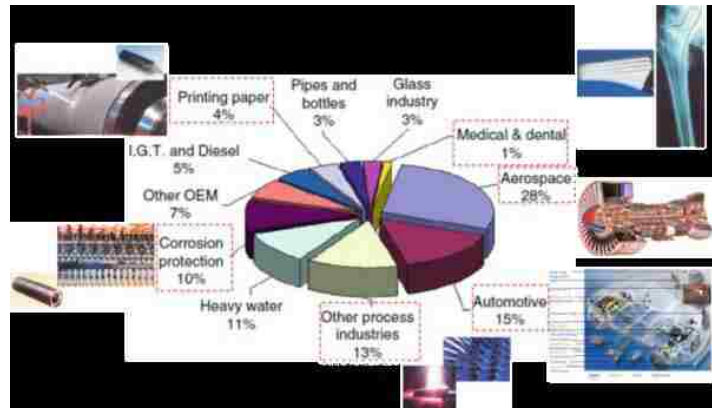


Figure 2-2 Industrial applications of thermal spray technology in Europe in 2001[10]

The working principle of thermal spray processes is that a heat source melts the feedstock in powder, wire, rod or cord form and then process gases accelerate the molten material or semi-molten material onto a prepared base material. At last the droplets would rapidly solidify and form a solid thin layer adhering to the top of the prepared base material. The formed thin layer would be impinged by the next droplets repeating the processes. Thus all the droplets are built up and a well bonded deposit is formed on the top of the base material. The Figure 2-3 shows the principle of thermal spray [13].

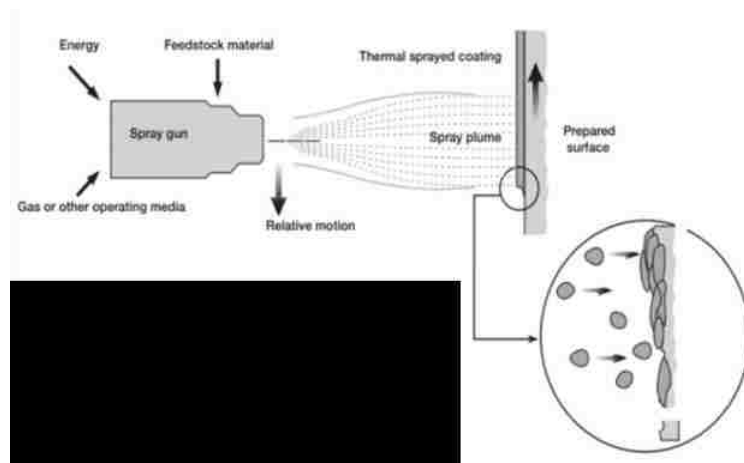


Figure 2-3 Principle of thermal spray process [13]

There are various types of thermal spray coating techniques, such as plasma spraying, detonation spraying, wire arc spraying, flame spraying, warm spraying, cold spraying and high velocity oxy-fuel. Spray torch, feeder, media supply, robot, power supply and control system are the main components in thermal spray process. Spray torch is the device that contains a combustion chamber used for melting and accelerating coating material. Feeder is used to preheat and supply the powder, wire or liquid to the torch. Media supply provides gases or liquids for combustion and carrying coating material. Robot manipulates the spray torch or substrate. Power provides electricity for the equipment and the control system connects all the mentioned components. Materials without decomposing during melting can be used for thermal spray coatings. The feedstock can be in wire or powder form depending on the required processes. Polymers and glass are used for powder spray processes. Refractory glass has been flame sprayed onto stainless steel where it formed hard, uniform and well-adherent coatings [4]. Among alloys the most popular is Ni-Cr for which adherence is very high on stainless steel substrates and is not affected by thermal

fatigue. Ceramics are also used to introduce the ceramic coatings. But ceramic coatings are not the strongest point of High velocity oxy fuel thermal spray process because the process is more prone to achieve high velocities than high temperatures. Titania is well melted in processes working with propylene. Alumina is mostly sprayed with chromia, which allows stabilizing the phase and it is suggested that sintering can play a role with good adhesive and cohesive coatings [4]. In Table 2-1 [13], some of the most frequently used classes of materials are listed, along with a typical example, characteristics and sample applications. Choosing a suitable material for specific applications requires special knowledge about the service environment as well as knowledge about the materials. Many factors such as coefficient of expansion, density, heat conductivity and melting point, additional factors, such as particle shape, particle size distribution and manufacturing process of powder material will influence coating performance.

Table 2-1 Powder materials used in actually thermal spray application [13]

Material class	Typical alloy	Characteristics	Example application
Pure metals	Zn	Corrosion protection	Bridge construction
Self-fluxing alloys	FeNiBSi	High hardness, fused minimal porosity	Shafts, bearings
Steel	Fe 13Cr	Anti-fretting	Repair
MCrAlY	NiCrAlY	Oxidation resistance, high hardness	Gas turbine blades
Nickel-graphite	Ni 25C	Wear resistance	Compressor inlet ducts

### 2.1.2 Plasma transferred wire arc process

Plasma transferred wire arc (PTWA) coating process was developed in order to increase fuel efficiency, automakers are placing emphasis on decreasing overall vehicle

weight as well as improving engine efficiency by reducing internal friction losses by Flame-Spray Industries and Ford Motor Company [14]. It is a wire based rotating spray process with combination of plasma spray process and twin wire arc spray process.

The plasma spray process is a thermal spray process in which arc generating plasma within a plasma torch works as a source of heat ionizing gas and melting the coating material, in-flight and propels it to the work piece. Plasma is an electrically neutral state resulting from the ionization of gas. It is composed of same amount of ions and electrons. The direct current arc struck between the cathode and the anode nozzle of the torch can increase the temperature to the required level [15]. The plasma gases which are usually Ar, H<sub>2</sub>, He, or N<sub>2</sub> are injected at the base of the cathode and heated by the arc. When the gas temperature reaches 7,000–8,000 K at atmospheric pressure, the thermal plasma will happen to ionize the plasma gases into the equilibrium mixture of ions and electrons, then exits the nozzle as a high temperature, high velocity jet. Thus the molten droplet will be accelerated towards the substrate by plasma and propellant gases. Figure 2-4 [7] is a schematic representation of plasma spray process. The plasma spray process is able to provide sufficient energy to melt almost any coating feedstock materials because the temperature in plasma spray process can reach as high as 15,000 °C [6], significantly above the melting point of any known material. Repeatable and predictable coating results can be obtained due to the accurately regulated gas flow and the applied current. Additionally, the shape and bore size of the nozzle, the point and angle that the material is injected into the plume, as well as the distance of the gun to the target surface are controlled, the



reproducible parameters for materials can be developed flexibly. But provisions for cooling or regulating the spray rate such as the distance of the plasma gun from the target components, the relative motion of the spray gun and target component to each other, as well as part cooling methods may be required to maintain substrate temperatures in the 95 to 205 °C range [8].

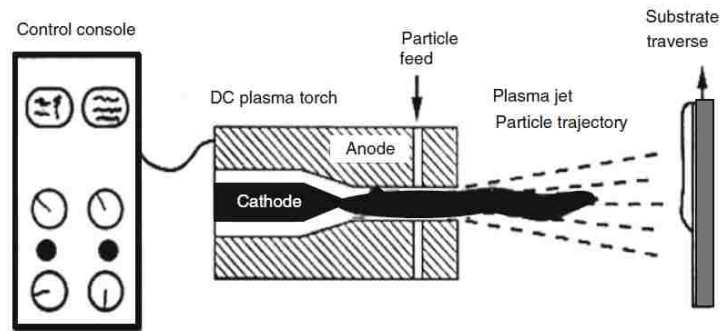


Figure 2-4 Schematic representation of plasma spray process [7]

The plasma spray system contains a plasma torch, cooling water supply, gas supply, power supply, high frequency starter and control unit. The control unit not only adjusts all the operating parameters such as arc initiation and current, plasma and carrier gas flow rates but also controls safety interlocks to avoid starting the arc without cooling water flow. The most central piece of the system is the plasma spray torch. The current flowing through the gas causes resistive energy dissipation resulting electric arc generating the high temperature plasma. It is reported that [16] the required temperatures for most plasma gases are 8,000 K and above at atmospheric pressure to cause ionization. There are cathode region, arc column region and anode region inside a plasma spray torch, shown in Figure 2-5 [7]. The cooling water supply is assembled by a closed loop of deionized water. As the boiling of water has to be avoided and the heat flux in the torch anode is

concentrated in a narrow area, the high pressure of the water is required. The water will be cooled in a heat exchanger after passing through the torch. About 50 % of the power supplied to the torch is carried away by the cooling water [7]. The cooling water is supplied to the torch through the power cables connecting the high frequency starter unit to the torch. The gas supply includes two or more high pressure gas cylinders with the gas flow rates controlled separately in control unit by mass flow controllers and sonic orifices. The gases are mixed and introduced into the plasma torch to push the arc root downstream. Argon is usually used as this primary gas due to its low energy density and low torch erosion rates and hydrogen or helium is used as secondary gas to provide a higher power density, gas velocity and the heat transfer rates. A current controlled rectifier works as the power supply in plasma spray process. Besides a starting circuit consisting of a high voltage transformer and capacitor is employed to initiate the arc breaking down a spark gap. The breakdown results in a high induced voltage spike in the power supply circuit leading to a breakdown of the arcing gap and initiation of the current flow. The final major component of the plasma spray process is the powder supply. A powder hopper is in the powder supply. By heating the powder hopper can avoid powder agglomeration and pick-up of moisture. The powder flow is controlled by a rotating wheel with a slot mounted at the bottom of the powder hopper and transported into the powder supply line is carried to the torch by the carrier gas.

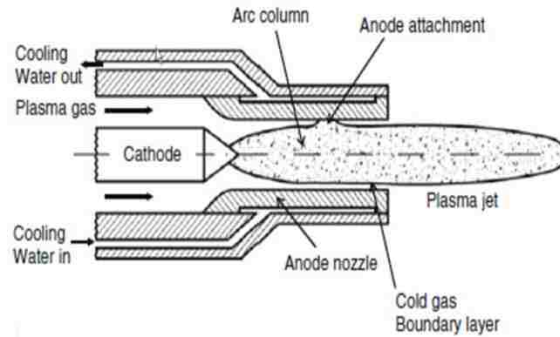


Figure 2-5 Schematic diagram of a plasma torch [7]

The wire arc spray process is one of the oldest thermal spray processes patented by Schoop MU [5]. Wire arc spray is a thermal spray process in which an arc is struck between two consumable electrodes of a coating material, compressed gas is used to atomize and propel the material to the substrate. In the process, an arc is formed by contact of two oppositely charged metallic wires, which are electrically connected to a power supply. The deposition material is introduced as wire and molten and atomized by an electric arc and a high-velocity gas flow. The high velocity gas flow between the wires and across the arc constantly removes the molten material from the wire tips, breaks down the larger droplets into smaller ones in a secondary atomization process and accelerates them toward the substrate. The process is shown in Figure 2-6 [7]. Most of the energy in wire arc spray is used for melting the metal so that the droplets experience only cooling during their flight to the substrate and heat flux of the droplet essentially determines the heat transfer to the substrate, which is lower than the heat flux experienced in processes in which a high-temperature gas flow is used. In this perspective, the low melting point substrates can be

coated with this process while for the substrates need preheating to improve the coating adhesion would require an additional heat source.

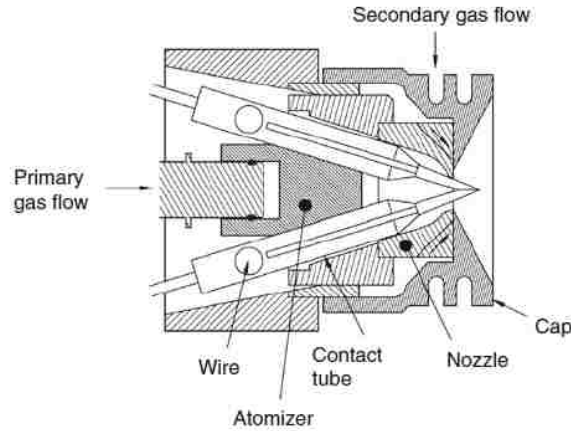


Figure 2-6 Schematic diagram of wire arc spray process [7]

The thermal spray coatings used for engine bores require special system. The thermal spray gun head has to be smaller than the diameter of the engines so that it can enter the bore easily to apply the process. Also, rotating the head gun is more preferable rather than rotating the engine. Based on those two considerations, the thermal spray system is characterized by rotating spindle. In industry manufacturing facilities, using wire is more controllable and less costly than using powder. Within all those perspectives, plasma transferred wire arc deposition process was invented and applied for the automotive industry.

The head gun mounted to a rotating spindle consists of a tungsten cathode, an air-cooled pilot nozzle made of copper and an electrically conductive consumable wire as the anode in PTWA process. The wire is fed perpendicularly to the center orifice of the nozzle. A high voltage discharge is initiated allowing the ionization and dissociation of gas mixture

happen between the cathode and the nozzle in the process. The plasma is forced to exit the nozzle at supersonic velocity because of a constricting orifice in the pilot nozzle. The elongated plasma is transferred to the consumable anode, the wire, completing the electrical circuit. A constant current power supply maintains the plasma from the cathode to the wire with an arc voltage of 100-120 V and a current of 60-100 amps to melt the tip of the wire and then the high-pressure plasma gas together with the atomizing gas strips the molten particles from the end of the wire [18]. Therefore a jet of finely atomized particles is created, which is accelerated toward the substrate at high speed. The atomizing gas can be any non-combustible gas, usually a mixture of argon and hydrogen will be used as the plasma and compressed air to atomize and accelerate the molten particles. In PTWA process, due to the high speed of the spray particles, dense coatings with a porosity of less than 2% will be created. So generally speaking, the PTWA thermal spray process utilizes a single wire as the feedstock material. The wire is melted, atomized and propelled to the substrate by a supersonic plasma jet that is formed by a transferred arc between a non-consumable cathode and the tip of the wire and then a large flow of forced air through the nozzle transports the stream of molten droplets onto the bore wall. The high kinetic energy causes the particles to flatten when they impinge on the surface of the substrate; the heat transfer between the flattened particles and the substrate causes a rapid solidification. Thus the coating is made up of these solidified droplets stacked one on top of another along the surface.

The equipment of a typical plasma spray system usually powered by two DC rectified constant current power supply devices. The plasma gun consists of a thoriated tungsten cathode and a copper anode in a water cooled brass housing. Plasma gases, power and cooling water are routed through a control panel to the plasma gun. Cooling water flow rates are stepped up from about 2 gpm incoming to 5-7 gpm at 200 psi to achieve proper spray gun cooling [29]. The wire feeder and wire straighteners are independent of the control panel and are adjusted directly on the individual device. Working distances are measured and set manually. Translation of the plasma jet is also performed manually. Further automation, even computer controlled operation, of the spray process could be implemented, however during the research phase it is impractical. The schematic diagram of the typical equipment of plasma spray, the PTWA system and the process are shown in Figure 2-7 [17], [29]

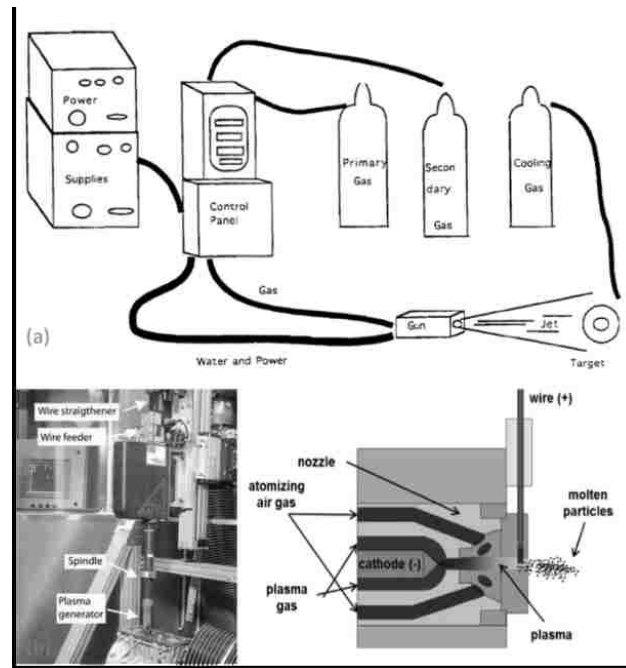


Figure 2-7 (a) Plasma sprayed system [29]; (b) Plasma transferred wire arc system and schematic diagram of PTWA process [17].

### 2.1.3 Application processes of PTWA coating

The PTWA process influences the quality of coatings. The process of PTWA coating application to the aluminum engine include four steps which are bore machining in order to give bores the correct diameter, surface activation to obtain the highest bonding strength for the coating, coating application and coating honing. The first two processes are known as the pre-treatment and the process after coating application is known as post-treatment for thermal spray coating deposition technologies to stable the coating formation and smooth the coating surface. The most critical step for apply coating is the preparation of substrate prior to spraying. There will be a high chance of failure of the coating without

surface preparation because coating adhesion quality is directly related to the cleanliness, the roughness and the proper machining for optimal coating performance [8].

Proper machining would be adapted before any steps to mill undercutting the substrate target area to accept the coating in the PTWA coating application to aluminum engine bores. Besides, machining is used for creating grooves or threads into the surface to improve the adhesion. The machining process includes as-casting and fine boning in this project. The inner diameter of aluminum engine bore is pre-machined to 82.8 mm in the as-casting process. Then the grooves are crated during the fine boning process as mechanical interlocks the pre-machined cylinder for better adhesion during the coating formation.

Cleaning is extremely important for the process after machining. All the contaminants have to be removed from the surface in cleaning. The most common contaminants that may exist on the surface are oil, grease and paint. Besides, the fingerprints and airborne debris are also considered as contaminants that need to be handled with clean fixtures and materials. Vapor degreasing, baking in an oven, ultrasonic cleaning, wet or dry blasting, acid pickling, brushing, dry ice blasting are the ways to get rid of the contaminants in industry [20].

The next step following is surface roughening. The aim of roughening is to enhance the surface roughness to provide a mechanical interlock for coatings. As a result, the spayed coating will adhere to the substrate. Dry abrasive grit blasting is probably the most commonly used roughening technique. Dry abrasive particles are propelled toward the substrate at relatively high speeds. In the process, the sharp angular particles act like



chisels, cutting small irregularities into the surface. The substrates itself, grit blasting equipment, blasting parameters as well as grit material all affect the surface roughness of substrate, which will in turn influence the adhesion of the coating and substrate.

Blasting must always be performed in an enclosure designed and equipped with exhaust and dust collection facilities for recycling the used grits and the environment considerations. In order to recycle the grit used, it must be cleaned, rescreened and sized after each use. Once finer particles and dust have been removed, reusable material is transferred back to the blasting tank. The blasting parameters such as the diameter, the specific mass, the hardness and the speed and angle at which it is directed toward the substrate of the impacting particle all influence the amount of substrate deformation and irregularity created at the surface [21]. Griffiths et al. [22] found that upon impact, two main types of surface damage were observed. One is produced by an impact from a sharp, angular grit particle. A crater formed by plastic indentation of the surface region and elastic compression of the hinterland immediately beneath will be appear as angular with steep sides and resembles the shape and form of the impinging grit. The other type is produced when an impinging particle strikes the surface and micro-machines a crater with a large lip or prow at its exit end. The metal is cut by the sharp edge of the particle, through which a new surface is created. The metal is pushed and folded over onto the undisturbed surface. The new crater still has very angular features especially in the region of the microchip but more cured than the previous one. Grit blasting influences the adhesion of the sprayed coatings strongly. Blasting parameters affect the coating–substrate bond. The efficiency of

impacting grit particles reduces because they collide in-flight when the blasting distance is short and the particle velocity decreases when the distance is too long. Blasting pressure, time and grit size can affect the bond strength as well. The most commonly used grits in grit blasting are: aluminum oxide, silicon carbide and steel grit. Aluminum oxide is an angular and durable blasting abrasive and can be recycled many times. Usually aluminum oxide is used for hard surfaces because aluminum oxide is hard. If applied aluminum oxide on soft surfaces, embedding may happen. Silicon carbide is the hardest blasting used and it is manufactured to be blocky grain shape. As a result, splinters and makes grit particles having rather sharp edges. Because the silicon and carbon with oxygen exist both in base material and coating, damage to the base material and coating deterioration may happen [21]. Steel grit has two functions depending on its hardness. The softer one with hardness of 40-50 HRC is mainly used for stripping oxides and cleaning and the harder one with hardness of 55-65 HRC provides a good cutting action [8]. Table 2-2 [8] shows the properties of the main grit materials.

Table 2-2 Properties of the main grit materials [8]

<b>Grit Material</b>	<b>Properties</b>
Alumina	Hard, angular, durable, easily recycled, embedded in soft surfaces
Silicon carbide	Hardest, very angular, break down easily, produces sharp peaks
Angular chilled iron	Soft (40-50 HRC) rounds off rapidly, hard (40-50 HRC) maintains angular sharp
Silica	Inexpensive, angular, breaks down very fast, may cause silicosis

After grit blasting, it is necessary to cleaning again to get rid of residue. The cleaning processes include blowing compressed air at a pressure of 0.4–0.5 MPa with a nozzle for a

few tens of seconds and then immersing the substrate in an acetone bath solution ultrasonically agitated.

After all the pre-treatments to substrate, the surface of substrate is ready for coating process. Generally speaking, in thermal spray coating deposition processes the feedstock particles with certain temperatures and velocities impact and flattens on the prepared substrate forming splats no matter what form the feedstock are. While in PTWA coating process, the molten particles are from the tip of wire fed perpendicularly to the center orifice of the nozzle. The temperature of feedstock will increase to melt or semi-melt the wire tip and this is accomplished by introducing the wire to high-pressure plasma gas together with the atomizing gas. And then those molten or semi-molten particles are accelerated toward the substrate at high speed. Once the accelerated particles impact the prepared surface, particles deform into flattened splats on the substrate surface conforming to the substrate topography. Once the particles hit the substrate, they quenched rapidly forming a mechanical interlock and a diffusion bonding with the substrate. Many researchers [24][25] studied how the coating formation happened by illustrating particle flattening on a smooth substrate. They noticed that solidification usually started even when flattening was not completed and digitations appear after a relatively symmetrical flattening stage, which is up to 1.4 ms. This is how the fingered splats formed and strongly depending on the dynamic wetting angles, drop surface tension and velocity and on solidification taking place before flattening is completed and modification of the liquid flow.

Usually one particle impacts on the substrate, the next particle would impact one the previous one. The time between two successive impacts is typically in the range of ten to a few tens of  $\mu\text{s}$ , so the next particle impacts on an already solidified splat. Coatings appear as layered splats, containing porosities, unmelted or partially melted particles and oxides for metals and alloys. Porosities are often caused by the poor ability of the flattening particle to follow the cavities present in the previously deposited layer. The feedstock feeding rate, process deposition efficiency and finally the spray pattern including the relative torch–substrate velocity control the formation of splat layers together. Microstructure of sprayed coating is affected by defects and it depends strongly on spray parameters. The parameters are including the working parameters (such as the spray distance and pattern), the temperature control of substrate and coating during the preheating, spraying and cooling phases and the shaped, size, thickness and preparation of the substrate shape and coating particles (such as composition, size distribution and injection parameters).

Scrivani et al. [26] investigated the effect of particle impact velocities and temperatures, as well as of the surrounding atmosphere by using same CoNiCrAlY commercial powder sprayed with three different processes. They found that these different temperatures and especially velocities, as well as the surrounding atmosphere, will result in various coating properties. That is because of the reaction between the oxygen and the hot particles in-flight. Usually the oxygen comes from air and the combustion oxygen. Beside, oxidation can occur at the surface of successive passes [4][7], while temperature control of

the coating can limit this oxidation. Moreover, oxidation present can also modify composition of sprayed materials. Villiers Lovelock [27] studied the microstructure and phase composition of WC–Co (12 and 17 wt%) during spraying powders and he found that the WC–Co powder experienced oxidation, decarburization and reduction because the powder react with the oxygen during plasma spraying. Reaction between WC and the cobalt binder metal during spraying was also studied. This results the formation of hard and brittle phases such as  $W_2C$ ,  $Co_3W_3C$ ,  $Co_6W_6C$ ,  $Co_2W_4C$ ,  $Co_3W_9C_4$  and even  $WO_3$  and tungsten [27]. Particle size distribution and morphology as well as their injection conditions influence the temperatures and velocities of particles. Narrow size distribution is required to limit particle trajectory dispersion, which depend on their injection force.

When the coating processes finish, post treatments of thermal spray coating are necessary as they can relax partially or totally residual stress, create compressive residual stress, close or reduce porosity, enhance the bond strength, create a barrier to corrosive or oxidizing products, improve coating homogeneity, improve splat or particle cohesion, obtain hard phase precipitation, or induce chemical modifications. Some commonly used post treatments include annealing for thermal spray coating performed at high temperature but below the coating melting temperature at atmospheric pressure in air or more generally in a controlled atmosphere or under vacuum; Austempering to promote diffusion at the substrate and coating interface and to collapse the internal pores and it is usually performed in molten salt bath; Sealing to prevent corrosive liquids or gases to

penetrate the coating and attack the interface between coating and substrate; limit the lodging of wear debris in the coating and enhance inter-splat cohesion [24][26].

#### **2.1.4 Parameters that influence the PTWA coating performance**

There are lots of parameters from feedstock to equipment settings effect the quality of the PTWA coatings on the coating microstructure and performance. The coating formation and quality depend on the particle or droplet impact, flattening, splat formation and cooling and splat layering first on the prepared substrate and then on already deposited layers. All the spray parameters such as the feedstock, equipment working parameters, the spray distance and pattern, temperature control of substrate and coating before, during and after the process as well as the situation of substrate will affect the particle or droplet impact, flattening, splat formation and cooling and splat layering. In this section, the effects of those parameters will be discussed.

The feedstock will influence the coating formation and quality strongly as the composition, particle size and particle distribution of feedstock have a significant impact on the coating performance. For different suppliers, the chemical composition as well as the size distribution and particle morphology can be different. In this project, the 1080 steel with composition of 0.75-0.88 carbon, 0.6-0.9 manganese; ( $\leq$ ) 0.04 phosphorus and ( $\leq$ ) 0.05 sulphur in the wire form will be used as feedstock in the process.

In the process, the wire should be ductile materials that allow smooth and consistent wire feeding and propelled by the plasma. Only when the wire feeding is in a continuous

feeding rate can it make sure that little variation of the arc gap occurs. At the beginning of the process, a desired voltage is set and the electrodes are consumable resulting in a varying arc length, the rectifier uses voltage control. When the arcing gap gets too small resulting in too low voltage values, or if the wires even touch to each other resulting in a momentary short, the current will increase to increase the melt rate. And when the melt rate of the wires is higher than the feed rate, the arc voltage will increase surpassing the set desired voltage, the power supply control will respond by reducing the arc current and therefore the melt rate until the set voltage value is again reached. Since the loss of a metal droplet from the wire tips usually leads to a stepwise increase in the arc voltage, one has continuous fluctuations of the arc voltage and arc current with the principal frequencies between 500 and 2,000 Hz. These fluctuations can be minimized by judiciously adjusting the arc voltage; the wire feed rate and the atomizing gas flow. The wire has to be as perfectible aligned as possible to minimize voltage fluctuations. The wire made of ductile and electrically conductive material frequently run through a wire straightener, consisting of an assembly of rolls forcing the wire through a straight path to reduce the wire curvature resulting in even melt rates. Additionally, density of material and particle size is consideration of both powder and wire.

The molten particles are mostly spherical during flight and upon impact flatten, the material flows outward and then solidifies into a final shape. The impact flatten is dependent largely upon particle temperature, the atmospheric pressure and the composition, impact velocity, viscosity and surface tension of the droplet.

The particle temperature affects the oxidation happening between the in-flight particles and the oxide as the process is operated in air. Oxidation of the sprayed metal can take place either in the vapor phase surrounding the droplet or at the surface of the droplet. Oxidation can also occur at the surface of successive passes, but the coating temperature control can significantly limit this phenomenon. The in-flight particle oxidation is controlled by diffusion and convection. Formed oxide layer can result in a considerable reduction of the evaporation rate from the droplet surface [7]. Besides, as the operation is in the air, the atmospheric pressure and the composition have a strong influence on the jet appearance and the heat and momentum transfer to the spray particles because the surrounding gas is mixed with the plasma gas. The plasma gas mixing with air results in the strongest quenching of the jet. The quenching will be even stronger when there is a high humidity in the air. Lower atmospheric pressures not only will result in less quenching and longer jets but will also reduce the heat and momentum transfer to the particles. Substrate temperature is found to be an important factor that will influence the splat shape because it can cool down the melted particles when the particles hit the substrate. Bianchi et al. [47] found if droplets landed on a cold substrate, the splats formed in irregular shape, because the droplets splashed extensively after impact by using scanning electron micrographs of individual alumina and zirconia splats deposited by plasma torches on a stainless steel plate. If droplets landed on a hot substrate, splats formed almost perfectly circular and were shaped like disks. Sampath et al. [33] confirmed this conclusion by studying how the substrate temperature effects the formation of splat as well as microstructure and



additionally affect the properties of the deposit coatings. They found that there is a critical substrate temperature regime above which the splats will form as round contiguous disks and below which they are fragmented and without easily definable shape. When the temperature is high, substrates will yield well layered lamellae. While when the substrate temperature is low, disarray deposits will display containing the small particles which are the products of the fragmented splat. The structures evolve from fragmented particles formed on low temperature substrates shows a higher chance to contain porosity than these evolve from high temperature substrates.

Impact velocity also affects the splat formation. The porosity and poor adhesion at the substrate interface and poor cohesion within the coating thickness can happen as the splat cannot penetrate into all the surface cavities if the particle velocity is too low. While if the particle velocity is too high, the larger splats may shatter upon impact yielding a malformed splat with poor adhesion. Usually high impact velocities and small particle sizes are optimized for the spray parameters as they can help the formation of low porosity, tightly adhering and small grained coatings.

The working distance for the spray process is important. It must be far enough to attain full melting and high speeds, yet close enough not to allow vaporization of small particles. Fully melting and high particle speed, resulting from heat and momentum transfer from the plasma jet to the particles is required to achieve dense, low porosity coatings. If the working distance is too long, the particles especially heavy particles will fall below the center of the splat resulting in falling out of the high temperature, high velocity

region, possibly missing the target entirely. While if the distance is too short, unmelted particles will bounce off and partially melted particles will be held as inclusions in the resulting coating.

In PTWA, the plasma torch and jet characterization will influence the spray process. Most plasma torches operate in a current control mode which is kept constant through a feedback control loop in the power supply which compensates by changing the voltage in order to maintain the current at the required set value. A specific plasma torch is characterized by the time-averaged arc voltage, its standard deviation and the cooling water temperature rise and these two quantities allow determination of the torch operation, its energy efficiency and the power carried into the plasma jet, as well as the average specific enthalpy of the plasma gas, its average temperature and velocity. The plasma gas, gas injector design, anode nozzle design, cathode shape are the parameters influence the arc voltage and torch efficiency. The argon usually used as the plasma gas and a small addition of hydrogen to the argon results in a strong increase in arc voltage and in torch efficiency as the fast diffusion of the smaller hydrogen atoms into the arc column fringes would happen increasing thermal conductivity. But a large addition of hydrogen will increase electrode erosion which is not advisable [8]. The radial injector, the axial injector and the vortex or swirl injector are the most commonly used plasma gas injector designs. It is reported that lower temperatures for using the radial injection, while higher voltage and power with using the axial the axial injector. As for anode nozzle design, a smaller nozzle diameter or a constriction of the nozzle downstream of an arcing chamber will result in

shorter arcs, lower temperatures at the nozzle exit, but possibly higher velocities for the same current and mass flow rate. The effect of a divergent anode nozzle or a Laval-type anode nozzle has been shown to result in less cold gas entrainment and higher deposition efficiencies [30][31]. The cathode shapes especially the tip influence the current density in the cathode attachment of the arc consequently the acceleration of the plasma gas into the nozzle. The peak velocities and steeper radial profiles of the cathode with the sharp-tip appear higher than the cathode with rounded tip. Besides, narrow conical cathode tip will be molten during operation and therefore eroding quickly due to ejection of small molten droplets, resulting in a change of cathode shape within the first hour of operation.

The pre-treatments and the post-treatment of processes also determine the quality of the coatings as discussed in the application processes.

## 2.2 Coating Properties

The thermal spray coatings are typically applied to components where high wear resistance is required to provide an acceptable service life. Extremely wear and corrosion resistant coatings can be applied by thermal spraying processes without changing the properties of the base material. Particularly, in the development of the light weight combustion engines, the light metal alloys combined with cylinder bores are more and more widely used. To ensure the optimum tribology of those light metal alloys engines, the thermal spray coatings which can be applied directly to the cylinder bores in the block are used. The required coating properties are reviewed in the remainder of this section to aid in the depiction of the required properties of a high quality thermal spray coating.

### **2.2.1 Microstructures**

The microstructure of a polished cross-section of coating can be observed using an optical or electron microscopy. The microstructure of thermal spray coatings can indicate the quality of the coatings. The microstructure of thermal spray coatings can be described as a layered structure. The high temperature and speed of particles in the thermal spray processes usually result in droplet deformation. The deformed particles will be on impact at a prepared surface, which will produce a thin layers or lamellae. This is always referred as splat. Generally speaking, the coating is an accumulation of individual particles built up during spraying. The particles impact, flatten and solidify with a sufficient time lapse between one particle impacting and the next one that hits the same spot such that solidified droplets can be built up particle by particle, layer by layer rapidly as a continuous stream of droplets impact to form continuous rapidly solidified layers. The single splat is very thin, with a thickness of 1 to 20  $\mu\text{m}$ , but as the coating is built up layer by layer, its thickness can be up to hundreds of microns. In the spray process, the individual particle tends to form an elongated splat rather than the idealized flat, round pancake splat when impact on the prepared substrate as the spray gun rotates. The solidified particles are of varying random size distribution when they hit the substrate. As a result, these factors combine to produce a layered microstructure with uneven thickness in layers. This mixture of individual splat shapes and sizes make up individual lamella with different thicknesses and with size and shape variations within the layers. This results in a coating with

undulations in the lamellar microstructure. The orientation of the lamellae is generally in a curvature that follows the surface shape of the substrate [29].

In addition, structure coating porosity is also a good indication of the quality. For PTWA coating the porosity is usually low because of good control over the process with high-deposition rates. Coating porosity is formed because of the insufficient particles velocity or insufficient thermally softened resulting in the particles ineffectively interlock with the previously deposited splats. Coating pores in a kind of coating defects. The coating defects also include inter-lamellar cracks and delamination features. The pores in the coating can be classified into a closed void network or an open void network based on the void connectivity within the coating microstructure. A closed void network is used to describe the condition where the voids are not connected and reside within the interior of the structure, where an open void network accounts for all the pores and cracks are connected to the coating surface.

Another feature of the microstructure is the interface between the coating and the substrate. The interface is important as it suggests the adhesion of the entire coating. Usually the interface provides a mechanical interlock suggesting the interface should be sufficiently roughened by a process that does not promote particle embedment, as embedded particles have been suggested to act as stress-risers at the interface. Figure 2-8 [18] shows a typical micrograph of PTWA coating. In the micrograph, we can clearly see the layered structures, the porosity, the oxides and the interface.

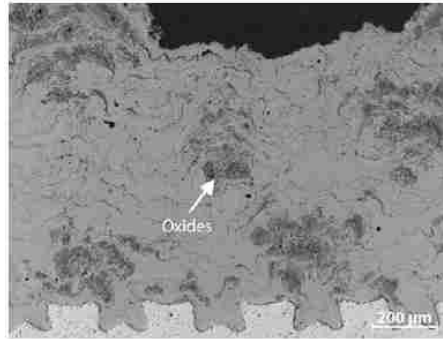


Figure 2-8 Micrograph of a 0.82% C-steel coating applied with the PTWA system. In the figure, the oxide phases appear darker than the Fe matrix [18]

### 2.2.2 Mechanical properties

The quality and performance of thermal spray coatings are strongly dependent on the adhesion between the coating and substrate because the debonding of coating will result in the collapse of the sprayed system. The basic bonding mechanisms between thermal spray coatings are actually depends on really contact between the coating and substrate which is between about 15 and 60 % of their surface [7]. Fauchais [4] defined adhesion as “Adhesion can be defined through fracture mechanics that consider the energy required to initiate or propagate cracks and evaluate the adhesion of the coating system in terms of fracture toughness“. The adhesion between the coating and substrate decide the quality and performance of thermal spray coatings. The spray process, operating conditions, feedstock particle size distribution and morphology, the substrate material, the residual stress and the environment conditions decide the coating adhesion. Zaat [35] proposed that the bonding mechanisms between the thermal spray coating and the substrate are categorized into mechanical interlocking, metal to metal bonding and chemical bond. The metal to

metal bonding is caused by diffusion and chemical bonding which is caused by the formation of an intermetallic compound with a substrate. Kvernes [36] mentioned that residual stress can also enhance or decrease the adhesion of the coatings especially for the thick ones.

The metallic feedstock melts and flows at the substrate surface easily and imparts a high specific area of contact, which cause high adhesion between the intermediate coatings and the ceramic overlay. In the meanwhile, the bond coat acts as a compliant layer between the ceramic overlay and substrate so that lower stresses are transferred to the ceramic coating [28]. The adhesion of thermally sprayed coatings is the combination problem of lamella structures within the coating, the interface between the substrate and coating, residual stresses, crack population and pore size and distribution [32]. According to the ASTM C366, the failure modes of the thermal spray coating under tensile test conditions are interfacial failure, cohesive failure and mixed mode failure. If the failure happens in the interface between the coating and substrate, the adhesion strength of the coating has been measured. If the failure happens within the coating, the cohesive strength of the coating has been measured. Sometimes if the strength of the adhesive is greater than the minimum required adhesion or cohesion strength of the coating, the epoxy failure happens. If the failure happens in a combination of the first two modes, it is mixed mode failure [19]. It has been reported [34] that the coating cohesive failure would happen either within the bond coat, within the ceramic top coating or at the interface between bond coat and ceramic if the coating is a duplex system such as a thermal barrier coating.

The failure happens in a region and then expanding to other ones. No matter what failure it is, the strength represents the weakest part of the tensile test system. The possible failure locations are shown in Figure 2-9 [23].

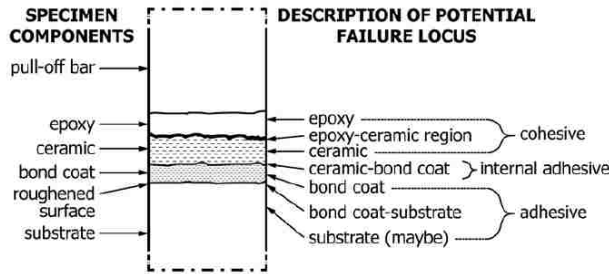


Figure 2-9 Specimen arrangement and possible failure modes for tensile adhesion tests [23]

## 2.3 Wear mechanism

### 2.3.1 Introduction of wear modes

The damage to a solid surface, generally involving progressive loss of material, due to relative motion between the surface and a contacting substance is defined as wear [41]. And friction is the resistance of the relative movement between two bodies. The wear usually includes abrasive wear, chemical and oxidative wear, erosion, fretting wear, impact wear, sliding wear, etc.

Abrasive wear is due to hard particles or hard protuberances forced against and moving along a solid surface. Abrasive wear typically operates by the cutting or plowing of a surface by particles of equal or greater hardness. These particles can be embedded within the counterface or loose within the contact zone. Two-body abrasive wear and three-body abrasive wear are the most commonly known abrasive wear. The two-body abrasive wear



is caused by hard pits on the counterface and the three-body abrasive wear is caused by free rolling hard particles between sliding surfaces [51].

The chemical and oxidative wear is due to the reaction happening on wearing surfaces in almost any environment. The cause of the chemical and oxidative wear is a chemical reaction between the worn material and a corroding medium that can be a chemical reagent, reactive lubricant or even air. This reaction will influence wear and frictional behavior of the tribosystem [39]. When the surface is worn because of the presence of air or oxygen under unlubricated conditions, the oxidative wear happens. During the sliding wear, the load and sliding speeds are high enough to increase the frictional contact temperature, wear debris will change from metallic to metallic oxides, the oxidative wear will be dominant. If the oxide films are present on the worn surface, it is the mild wear, while if the oxide films are absent or removed, the severe wear happens.

Erosion is usually caused by the repeated particle impacts of small hard particles suspended in a fluid. It usually results in thinning of components and occasionally roughening of the exposed surface. These can lead to stress increasing due to the removal of material, leading to premature failure. Fretting wear is a phenomenon taking place between two surfaces having oscillatory motion of small amplitude occurring over a large number of cycles and impact wear is defined as the loss and/or displacement of surface material resulting from the mechanical interaction and collision of two or more solid bodies [39].

Sliding wear is the most common and most complex wear which can be referred to as dry sliding wear and lubricated wear. It is a relative motion between two moving bodies.

Delamination, subsurface fatigue, oxidation, material transformation from one surface to another and other behaviors are often found in sliding wear. Adhesion was found to be one of the sliding wear which would happen under lubricated or dry sliding conditions. When the surfaces contact to each other, asperity junctions would take place and then softer surface would happen to adhere to the harder surface resulting in formation of adhesive wear fragment [38]. Some other mechanisms such as surface fatigue caused by plastic deformation on ductile surface, surface fatigue due to cracking by void nucleation and propagation and delamination of die highly strained subsurface layers on ceramics solids and tribochemical reaction and cracking of reaction films are also found in sliding wear [39].

### **2.3.2 Introduction of lubrication**

Lubricant is a material of low shear strength between two sliding surfaces of higher shear strength. It can reduce the strengths of junctions formed and minimize asperity contact. By using lubricant the wear rate will be reduced in sliding wear. Lubricants typically consist of base oils and additives. Mineral oils and Viscosity are the most important properties of in lubricate. Hydrodynamic lubrication, elastohydrodynamic lubrication, boundary lubrication and solid lubrication are the most common types of lubrication systems.

When the sliding surfaces are separated by a relatively thick film of fluid lubricant and the pressure generated hydrodynamically within the film supports the normal load, the hydrodynamic lubrication happens. In hydrodynamic lubrication, opposing surfaces must be

conformal and only a small gap allowing converge for a hydrodynamic film between the sliding surfaces and is filled with lubricating fluid. The relative motion between the sliding surfaces generates viscous force which will result in the pressure within the lubricant to support the normal load. The viscous force is sufficient to keep the two sliding surfaces from having any contact and that the only friction is the system was the viscous resistance of the lubricant. Viscosity of the lubricant is an important feature. The friction and the thickness of hydrodynamic film will increase as the viscosity increase. But the heat generated by friction will reduce the viscosity, the thickness of the film and may result in metal to metal contact. The distance between the two surfaces decreases with higher loads on the bearing, less viscous fluids and lower speeds. The increase of the load and decrease of the speed cause the increase of the pressure within the film, which results a rise in the film viscosity, possible elastic deformation under the high load and asperity contact. As a result, coefficient of friction will rise at high loads and low sliding velocities [39], showing inFigure 2-10.

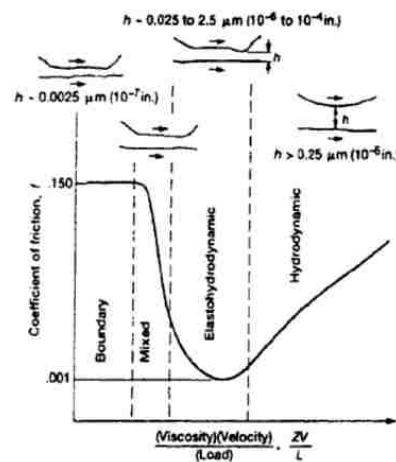


Figure 2-10 Effects of viscosity, velocity and load on the coefficient of friction [39]

When the contacting surfaces are counterformal, the local pressures in the contact zone are higher than those in hydrodynamic lubrication and elastic deformation of the contacting bodies and the changes of viscosity with pressure play fundamental roles, the elastohydrodynamic lubrication happens. The elastohydrodynamic lubrication is also referred as EHL, including a soft EHL and a hard EHL. The soft EHL is used to describe the contact surfaces have soft elastic bodies while the hard EHL is used for the bodies have higher elastic modulus [42]. The high pressure in EHL will increase the viscosity of the lubricant, resulting in the film thickness increasing so that elastic distortion of the surfaces will have a large impact on EHL. Figure 2-11 [42] shows an elastic sphere pressed on a rigid plane through modified Hertzian equations. It is shown that the film is nearly parallel for the most of its length and then develops a sharp constriction in the exit region, where its thickness reduced. For hard EHL contact of a sphere on a plane the minimum film thickness can be represented as:

$$h_{\min} = 1.79R^{0.47} \alpha^{0.49} \eta^{0.68} U^{0.68} E^{-0.12} W^{-0.07}$$

Where E is the reduced modulus of the surface, R is the radius of the shape. The minimum film thickness for soft EHL can be represented as:

$$h_{\min} = 2.8R^{0.77} \eta^{0.65} U^{0.65} E^{-0.68} W^{-0.21}$$

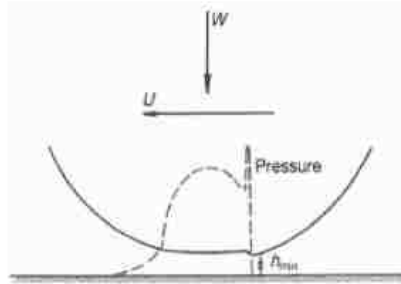


Figure 2-11 Elastic distortion of a sphere (shown exaggerated for clarity) under combined normal load and sliding motion [42]

Under high contact pressures or at low sliding speeds, hydrodynamic lubrication cannot maintain even a thin EHL film between sliding surfaces and the direct contact will occur between asperities. The wear rate and the friction will increase sharply unless the boundary lubrication happens [42]. Boundary lubricants function by forming absorbed molecular films on the sliding surfaces; repulsive forces between the films help support the load. The lubricant molecules adhere strongly to the oxide layer present in the metal, align perpendicular to the surface and are stabilized by mutual repulsion. This results in a lowered frictional force and substantially less wear. Many oils naturally contain some molecular species with boundary lubrication properties that a lubricant of only one molecule thick is sufficient to protect a surface [42]. Under severe conditions in the contact zone these additives react with the sliding surfaces and produce compounds with low shear strength, in turn creating a lubricating film at precise locations. Therefore, a comparison of the chemical attack to the mechanical damage is of great importance for optimum effectiveness of anti-wear additives [37].

Solid lubricants can also provide lubrication under the conditions that oil usually cannot be used such as at extremes of temperature, under vacuum conditions or in the presence of strong radioactivity. Solid materials usually exhibit low coefficients of friction. The scope of solid lubrication has been extended for depositing the solid film onto the wearing surface to produce a self-lubricating system. The lubricant deposition method is critical to the efficiency of the lubricating medium, since even the most powerful lubricant will be easily scraped off a wearing surface if the mode of deposition is incorrect.

### **2.3.3 Wear behavior of thermal spray coatings**

Lots of efforts have been made in order to investigate the wear mechanism and failure modes of thermal spray coatings. Critical sliding speed and pressure depending on the composition of steel and the transitions between mild wear and sever wear were reported by studying the wear behavior of steel and because of the friction heating process, the phase of the steel will change resulting from a self-quench hardening process. Ashby and coworkers [44] summarized the wear mechanisms of steel are mainly four kinds wear mechanisms which are seizure, melt-dominated, oxidation dominated and plasticity dominated wear through accounting for the frictional heating and calculating the flash temperatures. The oxidation dominated wear can also be grouped as mild wear and sever wear. The plasticity dominated wear also referred as delamination wear. Similarities between wear of steel and thermal spray steel coatings have been found. The oxidation dominated wear and the delamination wear are the most commonly wear in thermal spray

steel coatings. Based on Quinn's model of oxidational wear in which oxide film and that the film might flake off from the rubbed surfaces when the oxide reached a critical thickness (usually 1–3  $\mu\text{m}$ ) and appear as wear debris, So and coworkers [45] detailed studied the oxidational wear through microscopic analysis on the wear surfaces and by the measurement of the main factors occurring in the rubbing process of the pin-on-disc configuration. They pointed out that the oxidational wear actually depends on the combination effects of normal load and sliding speed. When the load and speed increased over certain limit, thick ferrous oxide films will be continuously formed covering a large area of the worn surface and the oxidational wear prevails. They proved that some part of the oxide film might crack and flake off from the rubbed surfaces causing by fatigue mechanism.

Rabiei et.al [43] studied the microstructure, deformation and cracking characteristics of thermal spray ferrous coatings found that cracks prefer to propagate within the FeO, along the interface of Fe and FeO and along the intersplat oxide. The thin oxide layers between splats comprise the dominant sites for cracking while thicker oxides and the inclusion are relatively resistant to cracking. The oxide phase presents in the material and preferred pathways for local cracking, especially thin intersplat oxide layers emerge as preferential sites. The low fracture toughness of the interfacial oxide could cause splat delamination upon frictional contact in thermal spray ferrous coatings. High wear rates were associated with the formation and propagation of subsurface cracks within the oxide veins, which is the weakest links in the coating, resulting in the removal of entire splats

during the sliding process by using thermally sprayed cylinder liners and piston rings on a bench-top wear tester. They showed splat delamination was also the common wear mechanism in thermal spray coatings.

### 2.3.4 Internal Combustion Engine

The reciprocating internal combustion (as shown in Figure 2-12) is considered as the most important component in vehicles as well as other transportation devices [37]. The high performance, reliability and versatility of the reciprocating internal combustion make it widely used in transportation devices. The most common types of engines are four stroke engine, two stroke engine and diesel engine. The main difference of those types of engine is which fuel is used and how the fuel is ignited. Usually the diesel engine is used in large vehicles such as trucks because diesel engines are associated with increased pollutant outputs and heavy engine blocks that exert high power and torque [39].

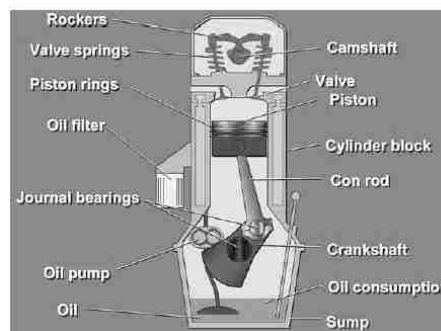


Figure 2-12 Main engine components in an internal combustion engine [39]



### **2.3.5 Operating principles of the internal combustion engine**

The basic principle of all the internal combustion engines is converting the converting the chemical energy to mechanical energy by burning a mixture of fuel and air in a narrow cylinder.

The four stroke spark ignition engines are used in almost all passenger vehicles because of its low fuel consumption and exhaust emissions comparing to two stroke spark ignition engines [39]. The working principle of the four stroke engine consists of four stages. The first stage is intake stroke, the second is compression stroke, the third stage is called expansion or power stroke and the last stage is exhaust stroke. Figure 2-13 shows the four stages schematically [39].

In the intake stroke stage, the intake valve would open and the piston moves downward to let the mixture of the air and fuel into the combustion chamber. The air and fuel can mix in a carburetor or intake port. In this stage, the pressure is equal to the atmospheric pressure. After the mixture of fuel and air comes in, the inlet and exhaust valve would both close. The piston is raised to compress the mixture of the fuel and air and the compression stroke happens. The spark plug is initiated and explosively ignites the compressed mixture when the piston reaches the top dead center of the cylinder. The power stroke happens. In this stage, the pressure increases because of the explosion which force the piston move downwards. At last, exhaust valve opens and the piston moves upwards to push the burned fumes out of the chamber. The cycle would repeat to provide energy for the automotive.

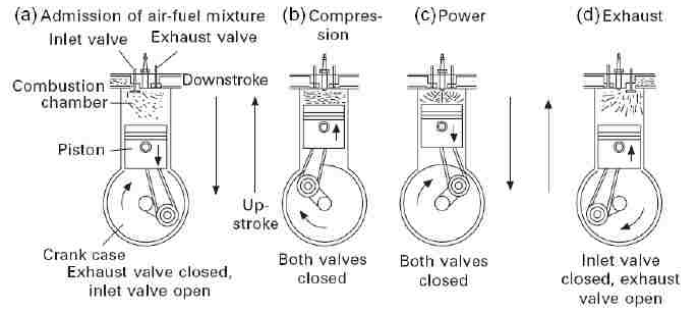


Figure 2-13 The Otto cycle of four stroke engine [39]

### 2.3.6 Piston assembly

The piston assembly forms a critical linkage in transforming the energy generated by combustion of the fuel and air mixture into useful kinetic energy. Typically, the piston consists of ring pack, the piston head, piston pin bore, skirt, pin, ring grooves and ring lands. The ring pack is a series of the metallic rings. Figure 2-14 [37] is a schematic representation of a piston assembly from a modern automotive engine. The role of the piston rings is to maintain an effective gas seal between the combustion chamber and the crankcase, to transfer heat from the piston into the cylinder wall and thence into the coolant and to limit the amount of oil that is transported from the crankcase to the combustion chamber. There basically are two types of the piston rings. One type is compression rings and the other type is oil-control rings. The top two piston rings are referred as compression rings. The top compression ring is the major gas seal and encounters the highest loads and temperatures as the ring nearest the combustion chamber. The second compression ring is designed to assist in limiting upward oil flow in addition to providing a secondary gas seal. The oil control ring is the bottom ring in the ring assembly. It has two running faces, or lands and a

spring element to enhance radial load. The role of the oil control ring is to limit the amount of oil transported from the crankcase to the combustion chamber and it has no gas sealing ability [37].

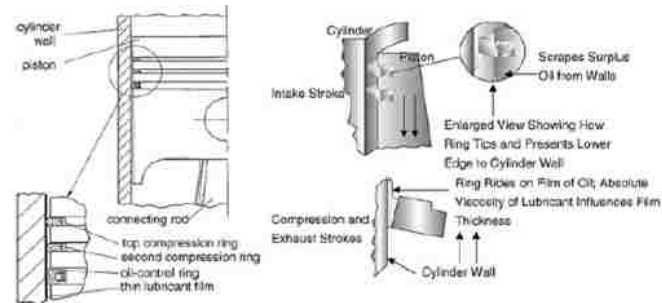


Figure 2-14 Piston assembly and piston ring function from an internal combustion engine [37]

The most complicated tribological component in the internal combustion engine is the piston ring because the piston rings would experience large variations of load, speed, temperature and lubricant availability [37]. The cylinder, piston and piston rings, lubricating oil and crankcase air are the elements in piston assembly tribosystem.

In the engine cycle, piston moves up and down, while the piston bears unevenly against the walls of the cylinder. This results thrusts against the sides of the cylinder. The side thrust load varies with cylinder pressure. The thrusts are referred as the major and minor thrusts. The major thrust side happens in the power stroke and it is more important as it bears the large side load and longer contact durations. The major thrust side is on the right side when viewing the engine from the flywheel end with the crankshaft rotating counterclockwise. The minor thrust side is a less thrust because the downward force from compression is much less than the downward force of combustion and it is on the opposite side of the major thrust side.

The internal combustion engine works under extreme environment including large variations in load, speed, temperature and lubrication. B. Slattery [39] described that in a single stroke of the piston, the piston ring interface with the cylinder wall can experience hydrodynamic (full), elastohydrodynamic (mixed) and boundary lubrication. At the top dead center and the bottom dead center, the velocity of piston is zero and the preloaded piston ring will squeeze the lubricated oil out of the gap generate pressure. In this position, the oil film thickness is less than the surface roughness, thus a mixed regime is observed. On the other hand, during the engine cycle between TDC and BDC the piston approaches its maximum velocity that hydrodynamic lubrication caused by the increased piston velocity is typically observed.

### **2.3.7 Engine wear**

Usually, the reciprocating engines operate with lubrication. The motor oil is used for engine lubrication of easy starting, to prevent wear, minimize friction by removing heat from engine surfaces, protect against rust and corrosion, keep engine parts clean by flushing away wear particles and seal combustion chamber etc. Engines operate under varying conditions as the temperatures, stress, sliding speed, even the lubrication change. All those factors influence the engine wear. Three major stages are found in the wear of engine. They are break-in stage, progressive wear stage and the final catastrophic wear stage. The cylinder will experience different wear mechanisms with the variations of cylinder gas pressure, temperature, the sliding speed of the piston rings on the cylinder

liner, load and quantity of lubricant and frequency of use, dirt, corrosion, surface finish [51]. The most common wear mechanisms found in engine are scuffing, abrasion and corrosion, each can occur separately or together [38][39][51].

Scuffing is also referred as adhesive wear. It is caused by the insufficient lubrication in the piston ring-cylinder wear system. It usually happens in the early stages of engine life when the oil film thickness is less than the surface roughness. The situation of insufficient lubrication causes a plastic deformation in surface liners and removing of the contacting asperities. With combination of high temperatures generated by friction and pressure exerted by the piston rings [38] can result in breakdown of the lubrication film, thus leading the agglomeration of removed asperities forming large work hardened particles [39]. As a result, the welding or adhesion of the surface happens.

Abrasion especially the three-body abrasive wear caused by the cutting and ploughing action of hard particles [51] is reported to be responsible for the normal mechanical wear that occurs in the majority of liners [38]. When the engine runs in extremely temperature, the corrosion wear is observed. Corrosive wear occurs in oxidizing or corrosive environment. At cold temperature, the oil loses its fluidity resulting in a thin oil layer. This allows moisture to make contact with the engine bore thus oxidizing or corrosive environment forms. The combined action of abrasion and corrosion appears to produce a smooth surface with well-defined graphite and a pitted and etched surface which may aid the retention of lubricant on the surface [38].

## CHAPTER 3 MATERIAL AND EXPERIMENT PRODUCERS

The materials preparation methods and experimental procedures employed to characterize the microstructural and mechanical properties of plasma transferred wire arc (PTWA) coating were described in this chapter. The engine bore with the PTWA coating as well as one traditional cast iron engine bore have been thoroughly examined using a variety of materials characterization techniques. The methodology used in this research is presented in Figure 3-1. Optical microscopy (OM), scanning electron microscopy (SEM) with energy dispersive spectroscopy (EDS) and X-ray diffraction (XRD) with Rietvelt refinement methods were employed to characterize microstructures, morphologies and compositions of the engine surface. Pull-out adhesion and hardness measurements were carried out to evaluate the mechanical properties of the engine surface.

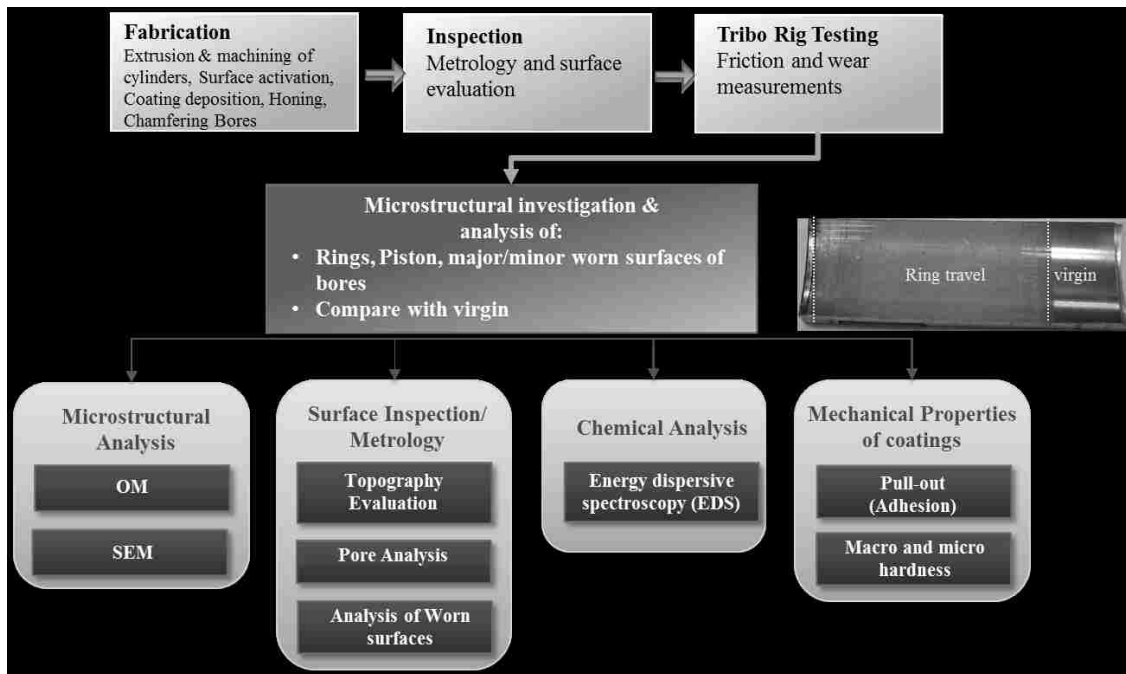


Figure 3-1 Flow chart illustrating the methodology used for engine bore characterization

### 3.1 Materials

Coatings were deposited on A380 aluminum cylinder bores by plasma transferred wire arc spray process. The substrate selected for the engine to be coated was A380 aluminum alloy. A380 aluminum alloy is one of the most commonly specified aluminum alloys offering the best combination of casting, mechanical and thermal properties as well as exhibiting excellent fluidity, pressure tightness and resistance to hot cracking. The typical composition of A380 was: Si 7.5-9.6 % wt, Fe max 1.3% wt, Cu 3.0-4.0% wt, Mn max 0.1% wt, Ni max 0.5% wt, Mg max 0.1% wt, Zn max 0.3% wt and Sn max 0.35% wt [49].

Prior to deposition, the inner diameter of bores were subjected to functional honing, roughening and pre-machining to final diameter of 82.8mm. The substrate surfaces were machined prior to the deposition to provide a mechanical interlock for the coating adhering to the substrate. The surface after activation was shown in Figure 3-2. Figure 3-3 showed the change of the inner diameter of cylinder bore during the process of surface preparation and coating deposition.

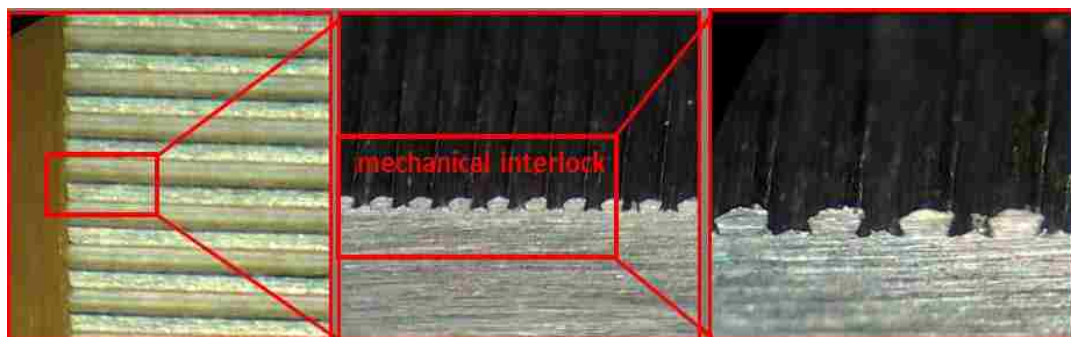


Figure 3-2 The Schematic illustrating the mechanical interlock after surface activation

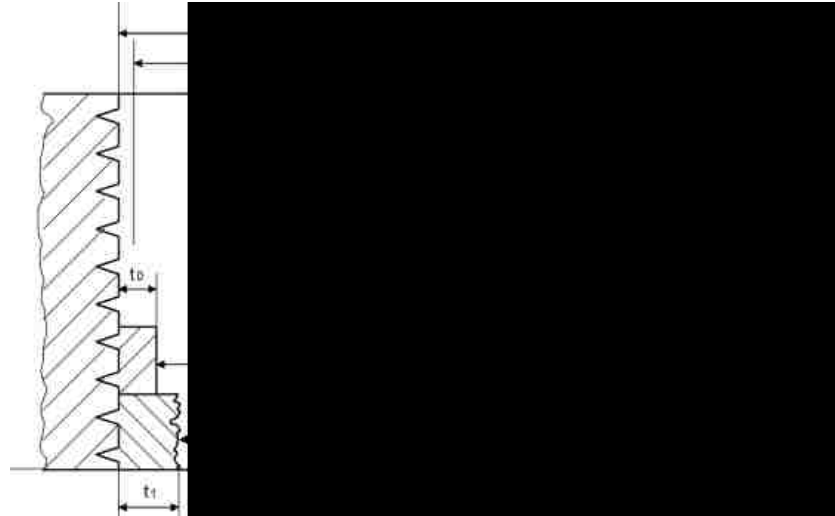


Figure 3-3 The Schematic illustrating the fabrication of the engine bores before and after applying PTWA coatings

### 3.1.1 Plasma transferred wire arc (PTWA) coating on A380 aluminum bore

The feedstock used for the PTWA coatings was 1080 steel wire with a composition of 0.75-0.88 % wt C, 0.6-0.9 % wt Mn, less than 0.04 % wt P and less than 0.05 % wt S. The coating was deposited on A 380 aluminum, which was referred to as PTWA-A coating in this thesis.

### 3.1.2 Cast iron bore

A cast iron sample was used for friction analysis comparison with the PTWA-A coating sample. The composition of cast iron liner was 2.5-4.0 % wt C, 0.1-1.0 % wt Mn, 1.5-3.0 % wt Si, 0.01-0.1 % wt P and 0.01-0.03 % wt S. It was a cast iron engine bore. The mechanical properties comparison of cast iron and A380 aluminum alloy is shown in Table 3-1 [50][56].



Table 3-1 Mechanical comparison of cast iron and A380 aluminum alloy [50][56]

Mechanical properties	A380 aluminum alloy	Cast iron
Density (g/cm <sup>3</sup> )	2.74	7.2
Modulus of Elasticity (GPa)	76	66-160
Elongation to Failure (%)	3	1
Fatigue Strength (MPa)	140	69-169
Shear Strength (MPa)	190	179-610
Ultimate Tensile Strength (MPa)	320	140-430
Yield Strength (MPa)	160	98-276
Melting Onset (°C)	530	1090

### 3.1.3 Plasma transferred wire arc (PTWA) coating on aluminum bore with different surface preparation

A ferrous-based PTWA coating deposited on B aluminum engine bore was also received as a case study to characterize the unworn part and for adhesion comparison with the PTWA-A coating sample. The coating was referred to as PTWA-B in this thesis.

The information of samples was shown in the Table 3-2.

Table 3-2 Information of specimens to be investigated

ID	Deposition Technique	Description
PTWA-A coating	PTWA	1080 steel wire used as feedstock deposited on A380 aluminum alloy (0.75-0.88C, 0.6-0.9 Mn, <0.04 P, <0.05 S, Bal. Fe)
Cast Iron	Casting	Cast Iron liner engine (2.5-4.0 C, 0.1-1.0 Mn, 1.5-3.0 Si, 0.01-0.1 P, 0.01-0.03 S, Bal. Fe)
PTWA-B coating	PTWA	A thermally sprayed aluminum engine bore was received as case study as well as adhesion comparison with PTWA-A coatings

## 3.2 Optical surface profilometer

The surfaces of PTWA-A coating engine bore and cast iron engine bore were examined before and after the non-firing floating-liner tests using a 3D optical confocal measurement system at NanoFocus. The inspections were performed at top dead center (TDC), which was 23 mm from the deckface and at mid-stroke, which was 50 mm from deckface. At TDC, 8 locations, which were 45° from each other and each one was of 2x2mm, were chosen for the surface inspection, showing in Figure 3-4 (a). While at mid-stroke, 4 locations, which were 90° from each other and each one was of 2x2mm, were chosen for the surface inspection, showing in Figure 3-4 (b).

Surface roughness, surface pore analysis and oil retention volume were measured through the 3D optical confocal measurement system.

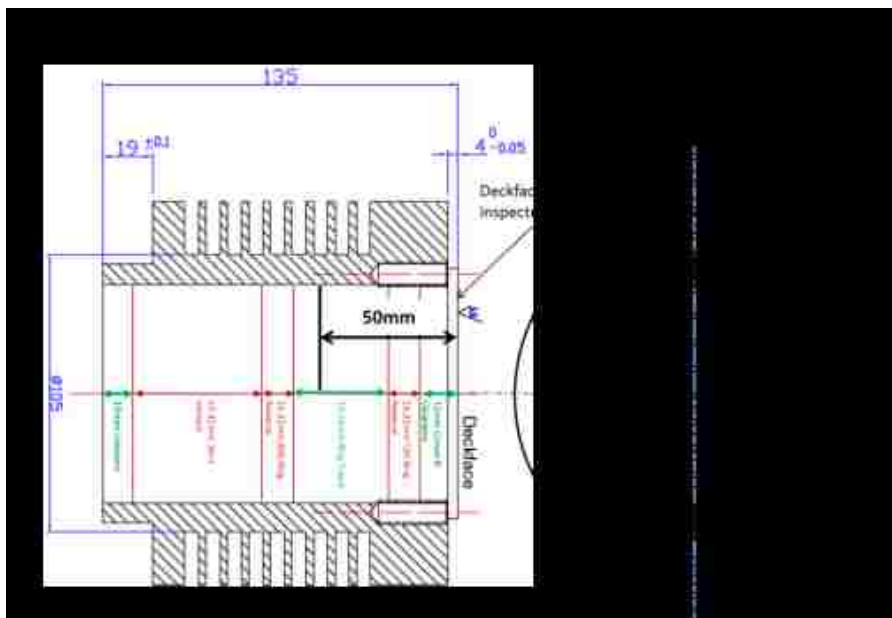
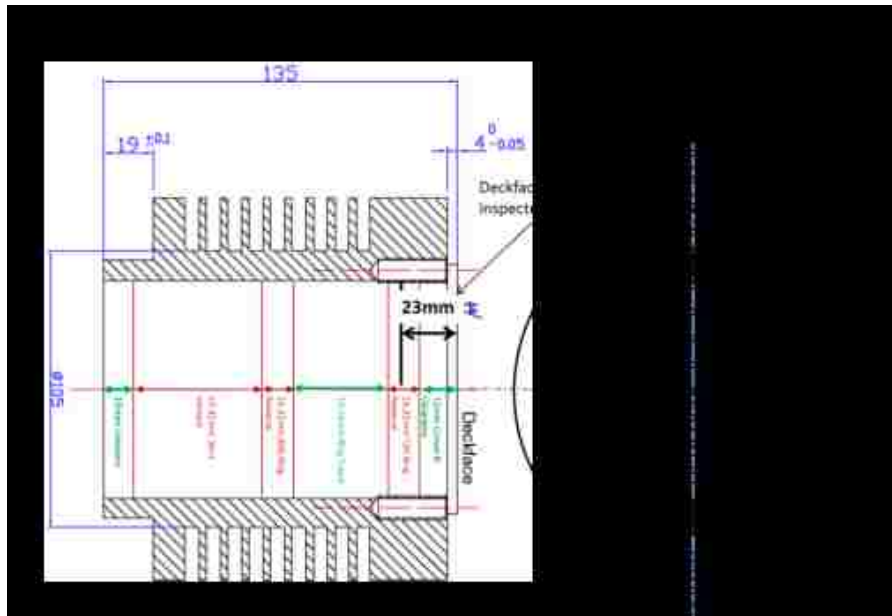


Figure 3-4 The Schematic illustrating the surface inspection locations at (a) TDC and (b) mid-stroke respectively (provided by NanoFocus)

A 10 mm\*20 mm sample was cut from the virgin region on the PTWA-B coating sample. Care was taken to ensure that the residual stresses to the sample were kept to a minimum and the oil residue on the surface was not cleaned during sample cutting. The sample was

rinsed with hexanes and dried in cool air. The surface topography and the surface roughness of the coating were examined using an optical profilometer (Veeco, Wyko). The analysis of surface roughness and morphology were performed based on similar profiles using an image analyzing software.

The surface statistic results of PTWA-A coating sample, cast iron sample and PTWA-B coating sample were based on average value of core roughness depth ( $S_k$ ), reduced peak height ( $S_{pk}$ ) and reduced valley depth ( $S_{vk}$ ). The core roughness depth  $S_k$  is the height difference between the intersection points of the found least mean square line. The reduced peak height  $S_{pk}$  is the average height of the protruding peaks above the roughness core profile. The reduced valley depth  $S_{vk}$  is the average depth of the profile valleys projecting through the roughness core profile.

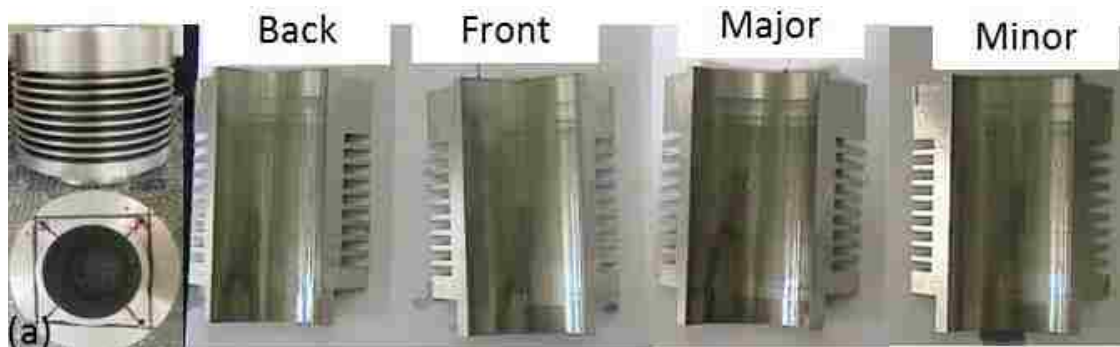
### 3.3 Non-firing floating-liner tests

The non-firing floating-liner tests were performed on the cast iron engine bore and the PTWA-A coating engine bore. The tests were performed under the lubrication of Shell 0W20 for 100 hours at 100 °C. The speed of the engine was set as 1200 rpm and the pressure at TDC was 25 bar. During non-firing floating-liner tests, the engine bore moved along the axis of the cylinder under the influence of the friction force between piston and cylinder. Even if firing condition was not applied, oil temperature, lubrication and in-chamber pressure condition were set, the pairing components contact is properly

reproduced and friction and sliding surfaces performance were evaluated. The friction force data were recorded for 2 minutes every 5 hour by means of three piezoelectric sensors.

### 3.4 Cross-Sectional preparation for microstructural observation

To analysis and compare the unworn and worn microstructures of the samples, cross sections of the samples were prepared. Individual engine bore was cut from coating to substrate by a saw band into major thrust side, minor thrust side, back and front side for further sectioning. As the major thrust side was the most worn part of the engine bore, a low speed saw fitted with a 150 mm diameter circular diamond rotating at approximately 250 rpm with a dead load of approximately 500g was used to section worn samples into 10 mm\*20mm from TDC and mid-stroke. The unworn samples were cut into 10 mm\*20mm by diamond low speed saw at the location where was 15 mm away from the end of the virgin region from the back side or the front side. Figure 3-5 showed the sample section. Care must be taken during sectioning the samples to avoid placing the coating and interface in tension which will affect the soundness of the coating and the interface between the coating and the substrate.



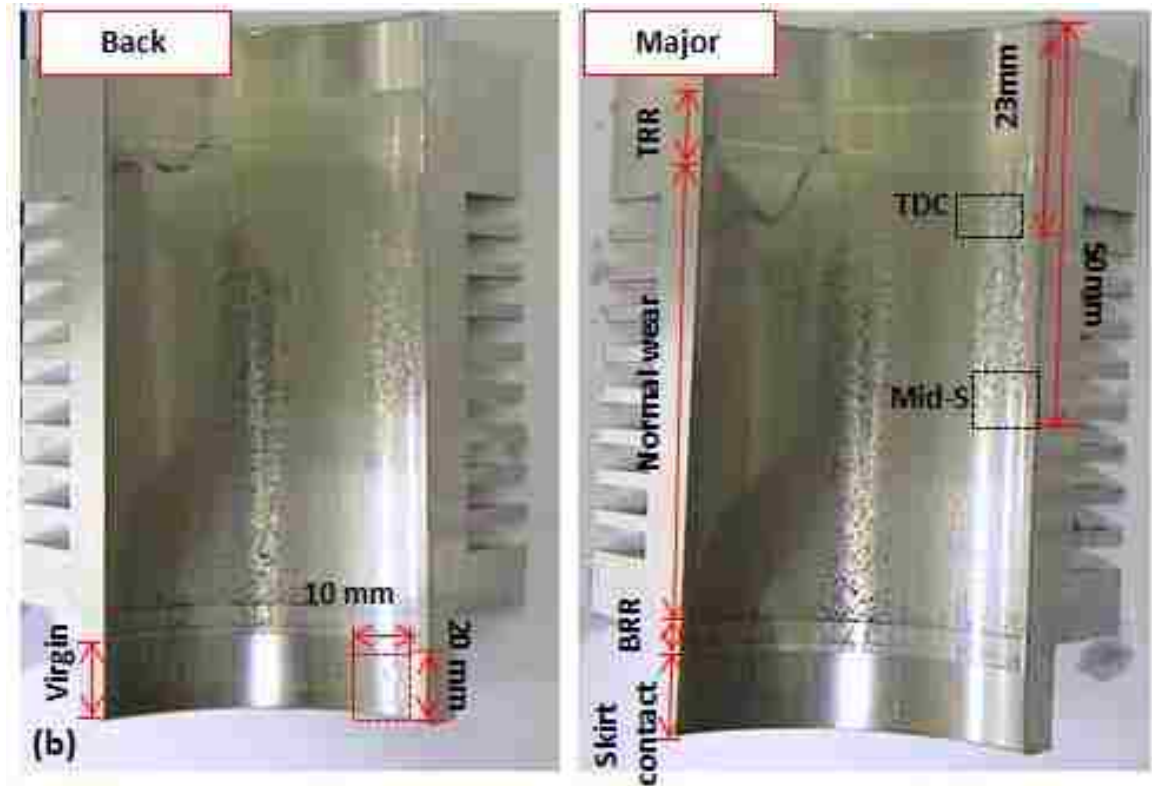


Figure 3-5 Sample section: (a) the main sides of an engine bore after non-firing floating-liner test; (b) the samples sectioned for further microstructural analysis, worn and unworn surface comparison; the area of each sectioned sample was 10 mmx20 mm

After sectioning, each sample was rinsed with hexanes to remove oil and dust and then cleaned in an ultrasonic acetone bath for five minutes to remove remaining residue and dried in cool air. After cleaning, samples were mounted using VariDur 3000 20-3580 cold mounting epoxy.

The morphology of the plan view unworn and the worn cylinder surface as well as the polished cross-section microstructure of samples were examined using a light microscope and a scanning electron microscope (SEM) fitted with an energy dispersive X-ray spectrometer (EDS) under high vacuum to determine the coatings microstructural characteristics and morphology.

## 3.5 Microstructural analysis

### 3.5.1 Cross-sectional microstructure

Metallography is a critical step to characterize coatings. Because PTWA coating microstructure consists of layered splats with porosities and unmelted particles, ceramic coatings that are more brittle than substrate and mixtures of many phases, this makes a challenge for metallography. If inappropriate metallographic methods are used, the apparent amount of porosity and linear detachment will increase by excessive edge rounding, or decrease by smearing of material into voids. Therefore a properly prepared metallographic surface based on standard guide for metallographic preparation of thermal sprayed coatings must be made. For cross-sectional microstructure analysis, the mounted samples were polished using a Buehler MetaServ 250 semi-automatic grinder/polisher under the instruction of ASTM E1920 – 03 [52].

### 3.5.2 Volume fraction of porosity within the coating

Porosity is a key microstructural feature of thermal spray coatings. Porosity analysis can be quantified based on the light reflectivity from a polished cross-section of the coating. Splat breakup and cracking due to rapid solidification, splat shrinkage upon cooling and trapped unmelted particles are some of the traditional explanations for porosity formation. After the cross-sections are properly prepared, the image of cross section can be captured and post processed using image analysis software to measure the porosity percentage.

To measure the porosity of coatings, ASTM E-2109 [53] was used for instruction. The optical images of prepared cross section samples were cropped to best fill the screen with the entire coating thickness. Then threshold the porosity in the field of view to adjust the range of gray values used to create a binary image result in pores appearing as dark pixels with the background as white pixels [53]. After threshold was set, the statistical analysis was performed by presenting the porosity percent as a ratio of black pixels to white pixels, which translates into the coatings porosity by percent area. Figure 3-6 was an example of the binary mask of a coating cross section containing 2.0 % porosity by area from ASTM E-2109-14 [53]. To measure the coating thickness, the scale of the software was set according to the optical or SEM image scale so that the software converted the scale into terms of pixels per micron. And then, draw ten lines along the coating cross-section and measured in length of pixels which can then be converted into microns by using the set scale. The average length and standard deviation were then calculated from the ten measurements.

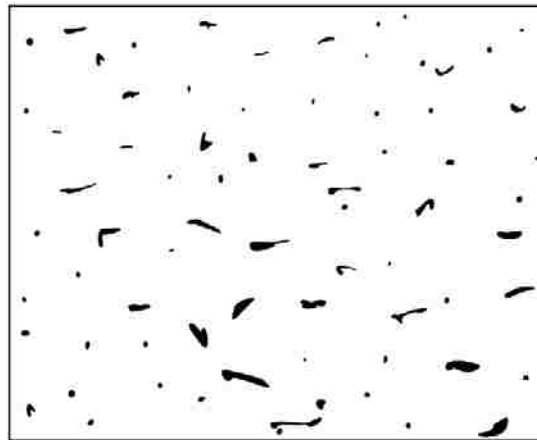


Figure 3-6 Example of binary mask of coating cross-section containing 2.0 % porosity by area [53]



### 3.6 Hardness Evaluation

ASTM E-18 [54] was used as instruction to measure the macro-hardness of all the samples by using a Mitutoyo Rockwell hardness tester. Before using the Mitutoyo Rockwell hardness tester, calibration test was conducted on a calibration block to confirm the hardness tester was calibrated and operating normally. In the measurements, a diamond indenter was used with an indentation force of 60 kgf. For each sample, at least seven tests have to be performance and then removed the highest and lowest outliers. To get the hardness, the middle five readings were averaged out, as well as the standard deviation. When performing the measurements, the distance between each indentation has to be at least three times than the diameter of the previous indentation to avoid error associated with strain hardening of the sample. Besides, after measuring one sample, calibration test has to be conducted to confirm the equipment was still operating accurately before switching to the tests of next sample.

### 3.7 Adhesion Evaluation

Adhesion tests were performed in accordance with the ASTM 633 standard test method [23] to evaluate the adhesion tensile strength of PTWA-A coating sample and PTWA-B coating sample. Samples of 10 mm × 10 mm area were cut from the virgin region of the bores. The samples were rinsed with hexanes and dried in cool air. Loading fixtures with self-aligning capability were designed and fabricated to accommodate the curvature on the surface of samples. Figure 3-7 showed a schematic illustration of adhesion test fixture modified for surfaces with curvature.

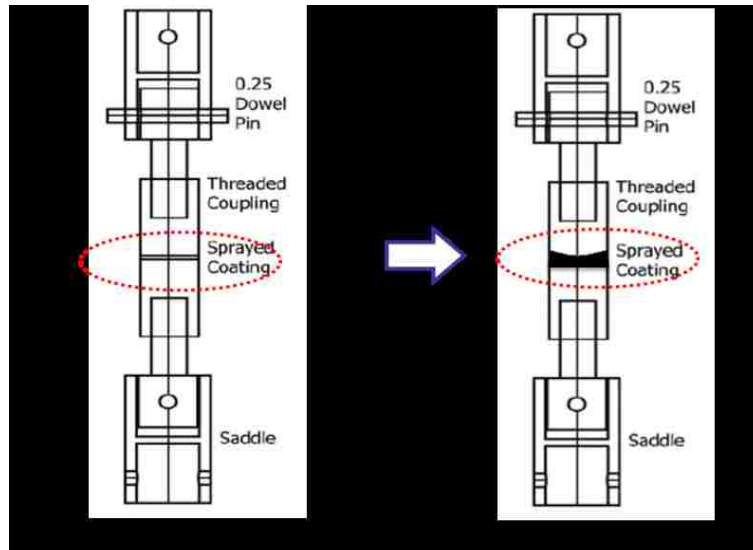


Figure 3-7 Schematic illustration showing the adhesion test modification for surfaces with curvature [23][55]

The test sample was glued to the sample holders in the loading fixture using polyamide-epoxy FM-1000 adhesive film. The surfaces of the sample holder and the uncoated side of the test sample were roughened for maximum mechanical bonding with the adhesive. Roughening was performed by blasting the surfaces with glass beads in a sand blaster. The optimum conditions for curing the adhesive film to its maximum strength were found after several attempts (tabulated in Table 3-3). The optimal curing cycle of the adhesive tape was heating at 190°C for 120 minutes under a 5 lb weight. After 120 minutes, the furnace was turned off and the assembly was allowed to cool down to room temperature. A bond strength of 6.3 kN (corresponding to 63 MPa) was recorded for the adhesive film. Tensile load was applied at a constant cross-head speed of 0.03 inch/min (0.013 mm/s) using until rupture and the maximum applied load was recorded (MTS

Criterion model 45). The test set-up and the self-aligning assembly mounted inside the tensile testing machine are shown in Figure 3-8.

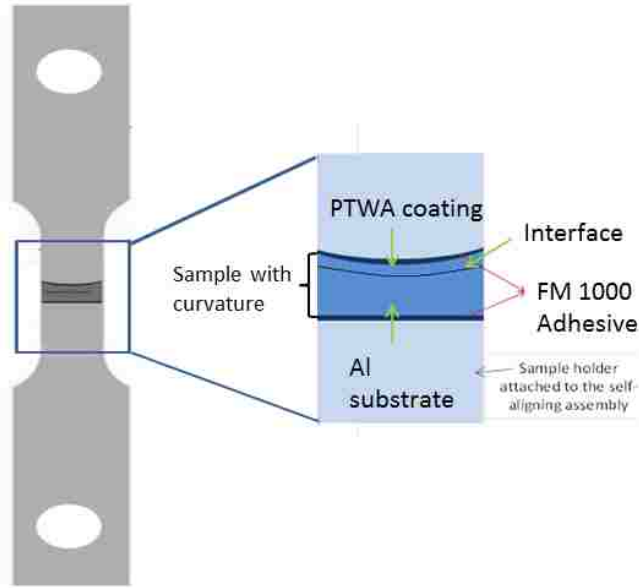


Figure 3-8 Schematic graph for the curved sample glued to the sample holders

Table 3-3 Conditions attempted to find the optimum conditions for curing the FM1000 adhesive film

Temperature (°C)	Time (min)	Failure load (kN)	Adhesive strength (MPa)
190	100	4.06	40.6
190	120	6.3	63
190	140	-	adhesive was over-cured

# CHAPTER 4 EXPERIMENTAL RESULTS

In this chapter, the results obtained from the tests are presented. The order of test results in this chapter follows the order of experiments represented in the previous chapter for convenience.

## 4.1 Optical surface profilometer results

This section described the optical surface profilometer results of the PTWA-A coating sample and the cast iron sample including the surface morphology, surface roughness and porosity analysis of the inspected locations at TDC and mid-stroke regions.

The optical surface profilometer for the PTWA-A coating engine bore and the cast iron engine bore were studied using a 3D optical confocal measurement system by NanoFocus. Eight measurements were obtained at TDC and 4 measurements were obtained at mid-stroke. Surface roughness, porosities were averaged out based on these measurements.

### 4.1.1 Surface morphology

The surface morphologies of the cast iron sample and the PTWA-A coating sample were studied using a 3D optical confocal measurement system by NanoFocus.

Figure 4-1 shows the surface morphology of the cast iron sample before the non-firing floating-liner test at TDC (Figure 4-1a) and mid-stroke (Figure 4-1b). The pores and honing marks are observed in the graphs at TDC and mid-stroke. Figure 4-2 shows the surface morphology of the cast iron sample after the non-firing floating-liner test at TDC (Figure

4-2a) and mid-stroke (Figure 4-2b). The graphs also show the wear traces besides surface pores and honing marks. It is shown that surface pores were decently removed after non-firing floating-liner tests.

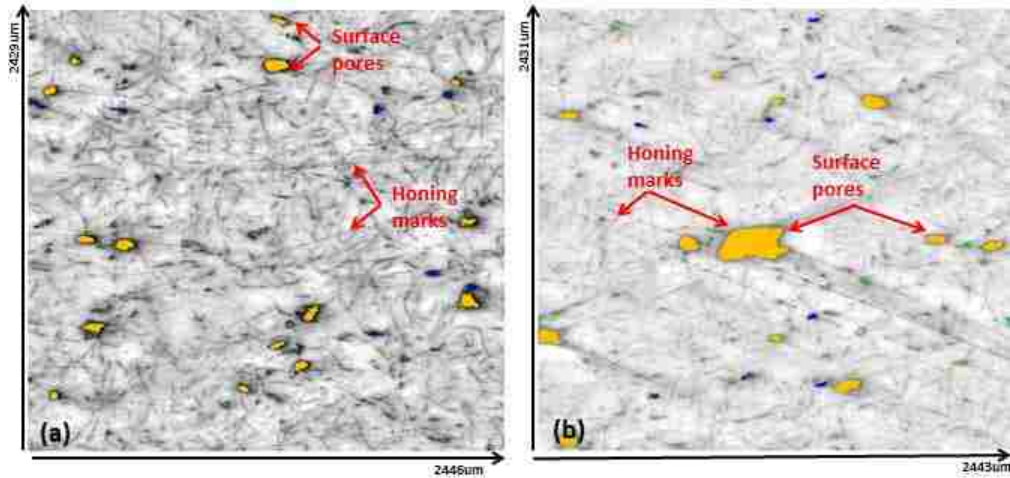


Figure 4-1 Unworn surface morphology of the cast iron sample at (a) TDC; (b) Mid-stroke, showing the presence of pores and honing marks

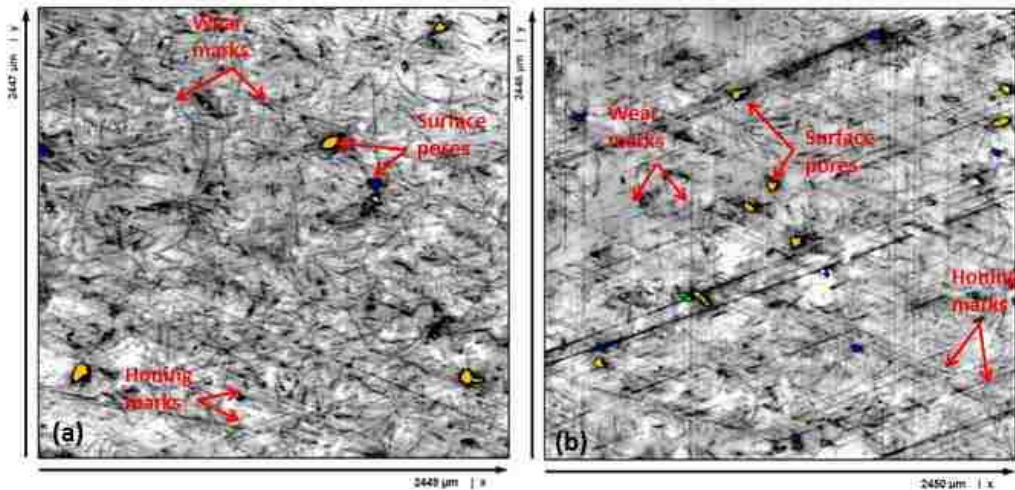


Figure 4-2 Worn surface morphology of the cast iron sample at (a)TDC; (b)Mid-stroke, showing the presence of pores, honing marks and wear scars

Figure 4-3 shows the surface morphology of the PTWA-A coating sample before the non-firing floating-liner test at TDC (Figure 4-3a) and mid-stroke (Figure 4-3b). The presence

of pores and honing marks are obvious in the graphs at TDC and mid-stroke. Figure 4-4 shows the surface morphology of the PTWA-A coating sample after the non-firing floating-liner test at TDC (Figure 4-4a) and mid-stroke (Figure 4-4b) respectively. The graphs also showed the wear traces besides surface pores and honing marks.

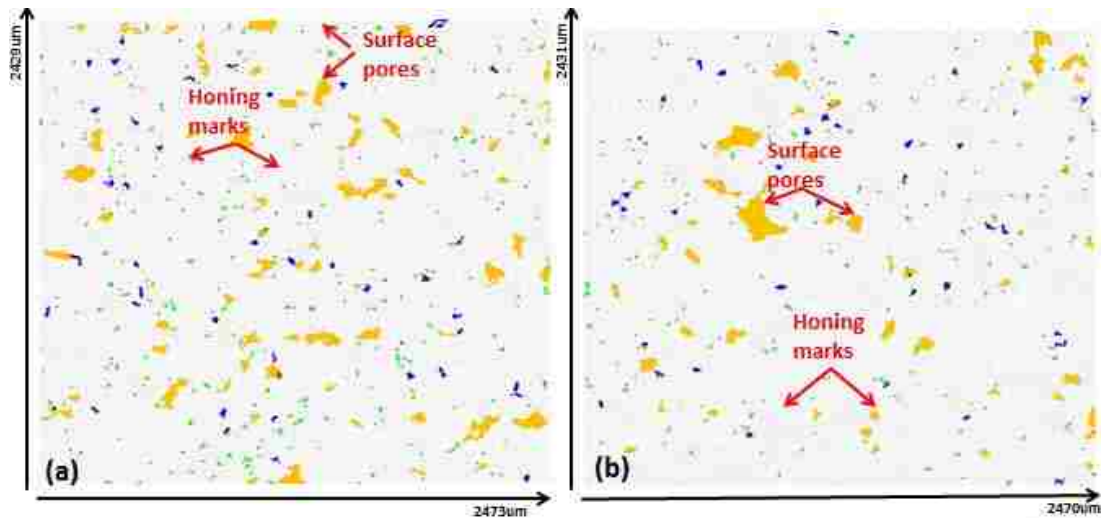


Figure 4-3 Unworn surface morphology of the PTWA-A coating sample at (a)TDC; (b)Mid-stroke, showing the presence of pores, honing marks and wear scars

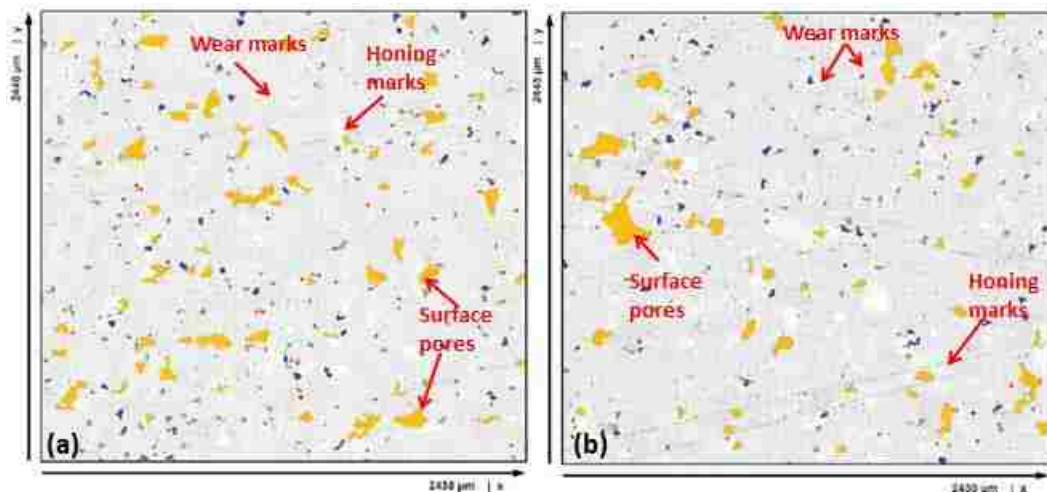


Figure 4-4 Worn surface morphology of the PTWA-A coating sample at (a) TDC; (b) Mid-stroke, showing the presence of pores, honing marks and wear scars

### 4.1.2 Surface roughness

The surface roughness of the PTWA-A coating engine bore and the cast iron engine bore were studied at TDC and mid-stroke using a 3D optical confocal measurement system by NanoFocus. Eight measurements were obtained at TDC and 4 measurements were obtained at mid-stroke. Surface roughness of cast iron and PTWA-A coating were averaged out based on these measurements.

The average  $S_k$ ,  $S_{pk}$  and  $S_{vk}$  of PTWA-A coating bore at TDC before the non-firing floating-liner test were  $0.177 \pm 0.133 \mu\text{m}$ ,  $0.111 \pm 0.015 \mu\text{m}$  and  $1.872 \pm 0.513 \mu\text{m}$ . These values increased to  $0.255 \pm 0.198 \mu\text{m}$ ,  $0.138 \pm 0.026 \mu\text{m}$  and  $3.551 \pm 0.613 \mu\text{m}$  after the non-firing floating-liner test. The  $S_k$  decreased from  $0.19 \pm 0.058 \mu\text{m}$  to  $0.171 \pm 0.102 \mu\text{m}$  and  $S_{pk}$  decreased from  $0.116 \pm 0.012 \mu\text{m}$  to  $0.089 \pm 0.006 \mu\text{m}$ , while  $S_{vk}$  increased from  $1.705 \pm 0.102 \mu\text{m}$  to  $2.525 \pm 1.551 \mu\text{m}$  at mid-stroke. The results are showed in Figure 4-5.

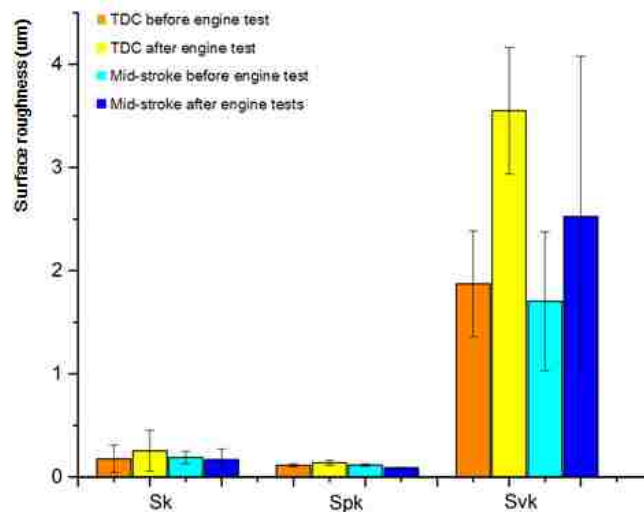


Figure 4-5 Surface roughness results of the PTWA-A coating engine bore

The cast iron engine bore had an average  $S_k$  of  $0.155 \pm 0.020 \mu\text{m}$ ,  $S_{pk}$  of  $0.048 \pm 0.011 \mu\text{m}$  and  $S_{vk}$  of  $0.271 \pm 0.097 \mu\text{m}$  at TDC before the non-firing floating-liner test. These values changed to  $0.141 \pm 0.021 \mu\text{m}$ ,  $0.048 \pm 0.012 \mu\text{m}$  and  $0.219 \pm 0.081 \mu\text{m}$  after the non-firing floating-liner test. The average  $S_k$  of cast iron engine bore decreased from  $0.165 \pm 0.044 \mu\text{m}$  to  $0.146 \pm 0.027 \mu\text{m}$ , the average  $S_{pk}$  dropped from  $0.058 \pm 0.022 \mu\text{m}$  to  $0.046 \pm 0.003 \mu\text{m}$  and the average  $S_{vk}$  reduced from  $0.382 \pm 0.181 \mu\text{m}$  to  $0.249 \pm 0.084 \mu\text{m}$  at mid-stroke after the non-firing floating-liner test. The results are showed in Figure 4-6.

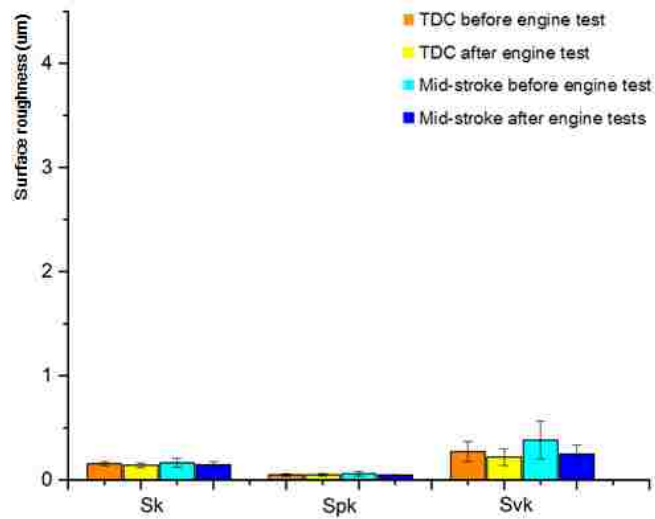


Figure 4-6 Surface roughness results of the cast iron engine bore

### 4.1.3 Surface pore analysis for PTWA- A coating engine bore

The surface pore analysis for the PTWA-A coating sample was analyzed through the 3D optical confocal measurement system by NanoFocus. The observed area for each measurement was  $2\text{mm} \times 2\text{mm}$ . The features of porosities including average pore number, depth, area and volume, all of which were all analyzed before and after the non-firing



floating-liner tests. The surface pore analysis was also performed on the cast iron sample, but as the flake graphite in the surface of cast iron acted as pores during the analysis. This made the pore analysis of the cast iron sample incomparable with PTWA-A coating sample.

The average number of pores for the PTWA-A coating sample at TDC and mid-stroke were  $703.50 \pm 131.70$  and  $677.00 \pm 32.76$  before the non-firing floating-liner test. The average numbers of pores at TDC and mid-stroke decreased to  $664.37 \pm 113.43$  and  $575.75 \pm 73.13$  respectively after the non-firing floating-liner test. The results are showed in Figure 4-7.

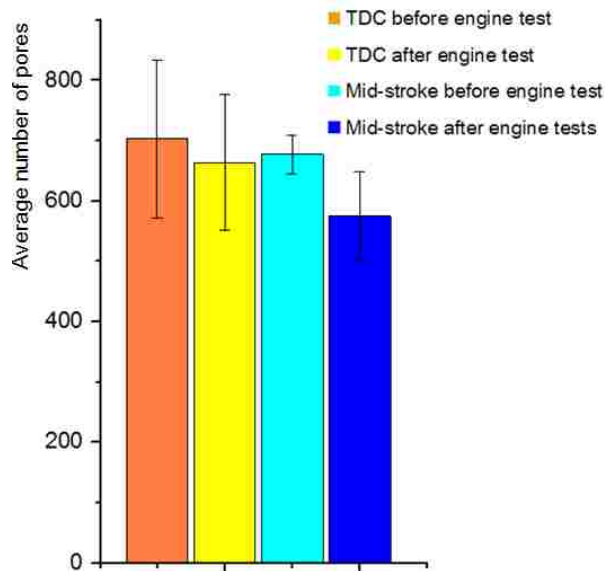


Figure 4-7 Average number of pores for the PTWA-A coating sample

A slight increase happened to the average areas of pores for the PTWA-A coating sample at TDC from  $377.77 \pm 42.74 \mu\text{m}^2$  to  $388.26 \pm 46.30 \mu\text{m}^2$  and at mid-stroke from  $304.18 \pm 41.26 \mu\text{m}^2$  to  $336.32 \pm 53.01 \mu\text{m}^2$  after the non-firing floating-liner test. The results are showed in Figure 4-8.

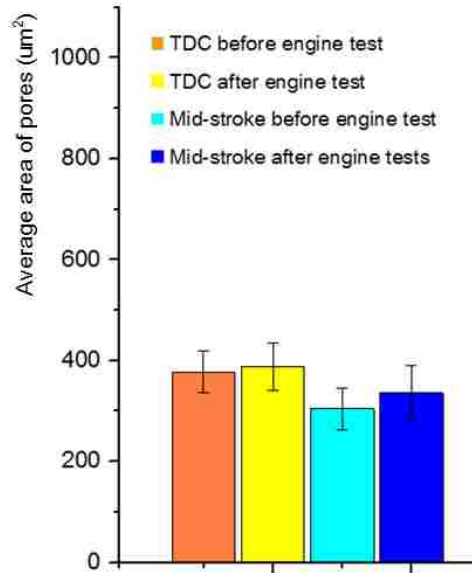


Figure 4-8 Average pore area (um<sup>2</sup>) of the PTWA-A coating sample

The average volume of pores for the PTWA-A coating sample raised from  $1650.81 \pm 391.72 \mu\text{m}^3$  to  $2260.30 \pm 508.79 \mu\text{m}^3$  at TDC and from  $1337.46 \pm 519.40 \mu\text{m}^3$  to  $1971.55 \pm 648.05 \mu\text{m}^3$  at mid-stroke after the non-firing floating-liner test. The results are showed in Figure 4-9.

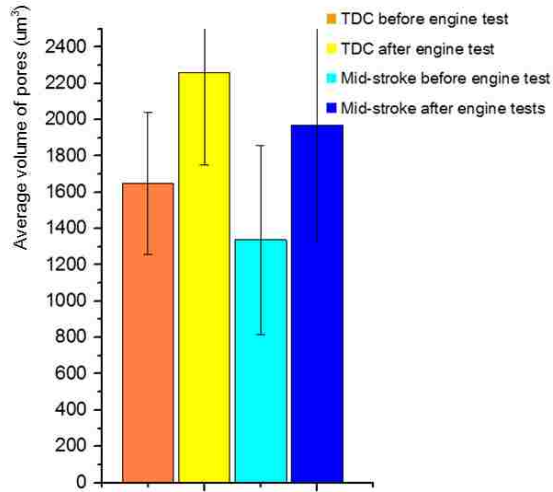


Figure 4-9 Average pore volume (um<sup>3</sup>) of the PTWA-A coating sample

The average depths of pores for the PTWA-A coating sample went up from  $2.97 \pm 0.45$   $\mu\text{m}$  to  $3.06 \pm 0.45$   $\mu\text{m}$  at TDC and from  $2.78 \pm 0.31$   $\mu\text{m}$  to  $3.26 \pm 0.29$   $\mu\text{m}$  at mid-stroke after the non-firing floating-liner test. The results are showed in Figure 4-10.

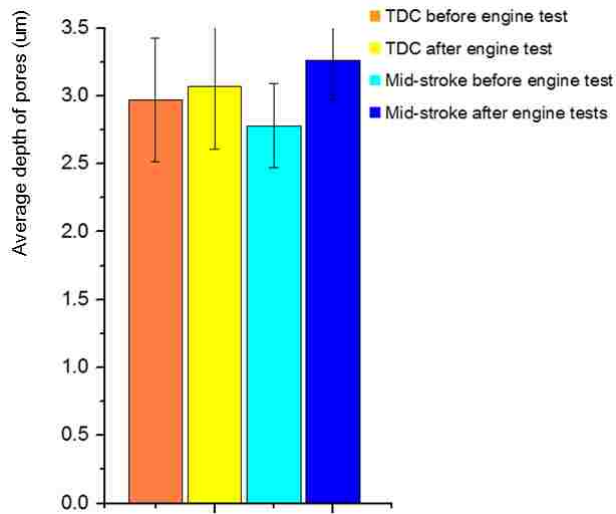


Figure 4-10 Average pore depth (um) of the PTWA-A coating sample

#### **4.1.4 Oil retention volume of the cast iron sample and the PTWA-A coating**

The oil retention volumes of the cast iron sample and the PTWA-A coating after the non-firing floating-liner tests were established. Data were only available after the non-firing floating-liner tests as the oil retention was oil residual of the lubricant oil. The oil retention volume was measured based on the pore size distributions.

The oil retention volume for the pores with size of  $10-50\mu\text{m}^2$ ,  $50-100\mu\text{m}^2$ ,  $100-500\mu\text{m}^2$ ,  $500-1000\mu\text{m}^2$  and  $1000-999999\mu\text{m}^2$  were  $0.013\pm 0.009$  ml/m<sup>2</sup>,  $0.021\pm 0.013$  ml/m<sup>2</sup>,  $0.093\pm 0.048$  ml/m<sup>2</sup>,  $0.078\pm 0.045$  ml/m<sup>2</sup> and  $0.513\pm 0.344$  ml/m<sup>2</sup> at TDC and  $0.020\pm 0.008$  ml/m<sup>2</sup>,  $0.020\pm 0.014$  ml/m<sup>2</sup>,  $0.104\pm 0.054$  ml/m<sup>2</sup>,  $0.075\pm 0.012$  ml/m<sup>2</sup> and  $0.447\pm 0.30$  ml/m<sup>2</sup> at mid-stroke. The oil retention volume results of the cast iron sample are shown in Figure 4-11.

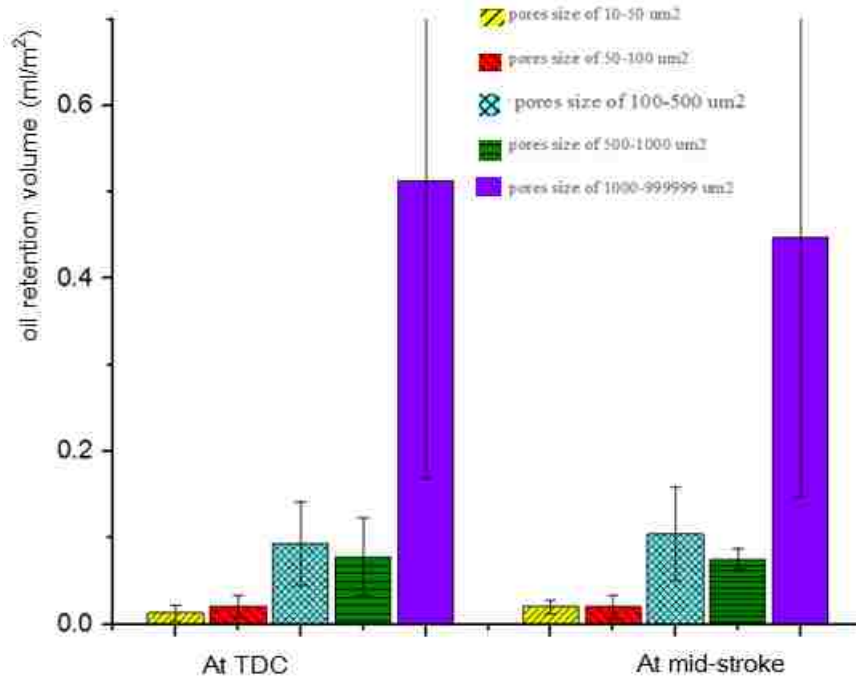


Figure 4-11 Oil retention volume (ml/m<sup>2</sup>) of the cast iron sample after non-firing floating-liner test

The pores with size of 10-50μm<sup>2</sup>, 50-100μm<sup>2</sup>, 100-500μm<sup>2</sup>, 500 -1000μm<sup>2</sup> and 1000-99999μm<sup>2</sup> for the PTWA-A coating sample had an oil retention volume of 0.135±0.021 ml/m<sup>2</sup>, 0.158±0.018 ml/m<sup>2</sup>, 1.061±0.187 ml/m<sup>2</sup>, 1.233±0.374 ml/m<sup>2</sup> and 22.041±3.559 ml/m<sup>2</sup> at TDC and 0.127±0.017 ml/m<sup>2</sup>, 0.162±0.017 ml/m<sup>2</sup>, 1.077±0.094 ml/m<sup>2</sup>, 1.223±0.396 ml/m<sup>2</sup> and 16.242±5.465 ml/m<sup>2</sup> at mid-stroke. The oil retention volume results of the PTWA-A coating are shown in Figure 4-12.

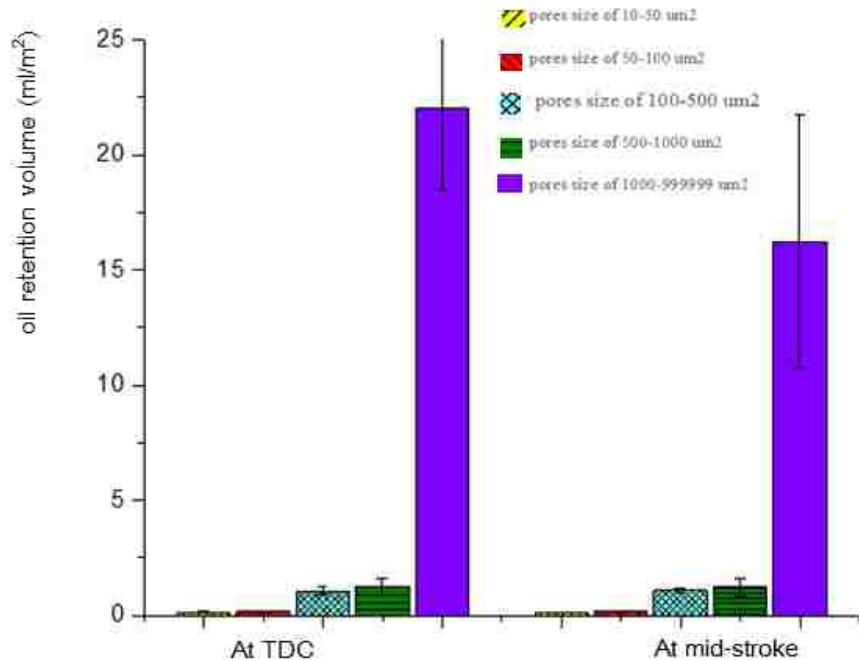


Figure 4-12 Oil retention volume (ml/m<sup>2</sup>) of the PTWA-A coating sample after non-firing floating-liner tests

#### 4.1.5 Surface morphology and surface roughness for PTWA-B coating

The ferrous based thermal spray engine bore, which was referred as the PTWA-B coating, was received as a case study as well as an adhesion test comparison sample. The surface topography of the PTWA-B coating was examined using an optical profilometer (Veeco, Wyko). Figure 4-13a shows the two-dimensional optical profile of the coated surface and Figure 4-13b shows the typical line profiles collected from the same area. The pore depth values were calculated based on this area and the result were  $6.82 \pm 3.21 \mu\text{m}$ .

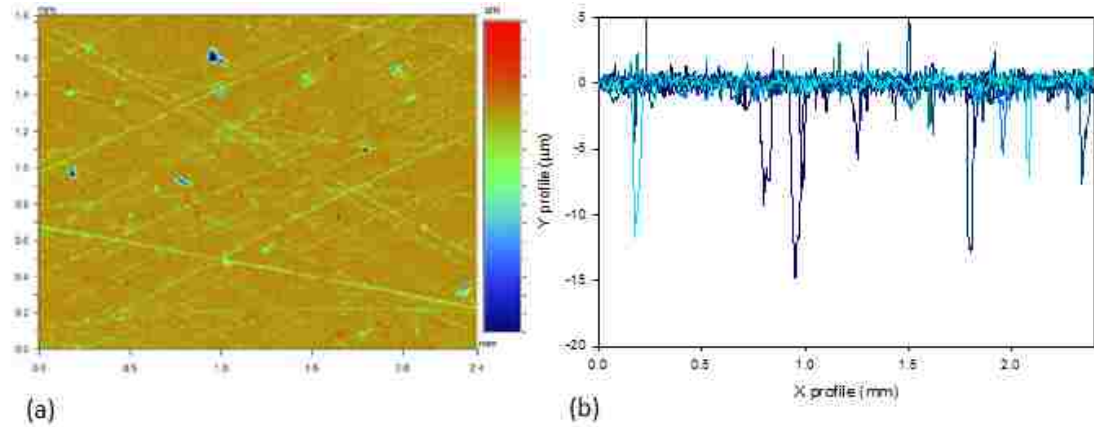


Figure 4-13 (a) A typical 2D profile of the PTWA-B coating surface showing presence of pores and honing marks, (b) several line profiles collected from the same area based on which the pore depth values were calculated.

The analyses of surface roughness and pore morphology were performed using an image analyzing software. The  $S_k$ ,  $S_{pk}$  and  $S_{vk}$  of the PTWA-B coating were  $805.7 \pm 64.3$  nm,  $446.8 \pm 105.9$  nm and  $1152.9 \pm 170.2$  nm. The surface roughness results were shown in Figure 4-14.

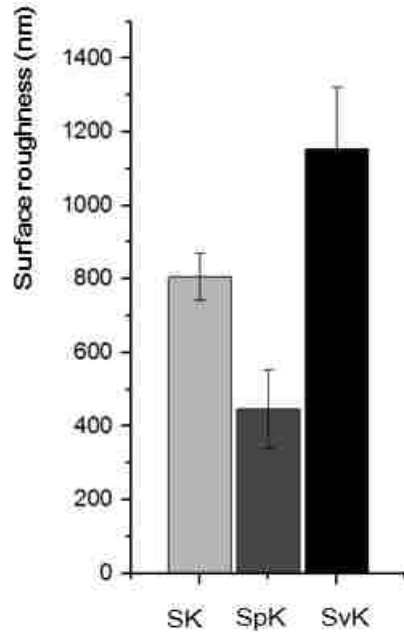


Figure 4-14 Surface roughness results of the PTWA-B coating

## 4.2 Non-firing floating-liner tests

The PTWA-A coating engine bore and cast iron engine bore were performed for durability tests to obtain friction force measurements. Figure 4-15 showed the friction force measured during the non-firing floating-liner tests. The initial friction of the PTWA-A coating engine bore was 230 N and then it dropped to 205 N. The friction force of the PTWA-A coating engine bore remained stable with some fluctuations after the break-in period. The initial friction force of the cast iron engine was 269 N, which was much higher than that of the PTWA-A coating engine bore. However, the friction force of the cast iron engine continued to decline.



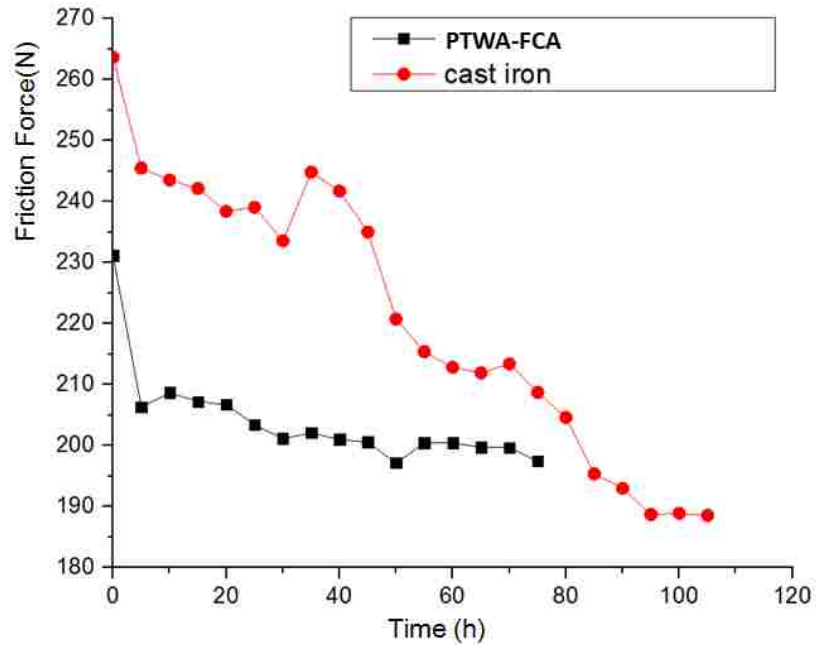


Figure 4-15 Average Friction Force Results: Time History

### 4.3 Microstructural analysis

In this section, the surfaces and cross-section microstructural of the samples before and after the non-firing floating-liner tests were presented.

#### 4.3.1 Surfaces before and after the non-firing floating-liner tests

The unworn surface areas were sectioned from the virgin part and the worn surfaces were sectioned from TDC of engine bores as discussed in section 3.4.

Figure 4-16 shows detailed SEM images of the unworn surfaces of the PTWA-A coating (Figure 4-16a) and the cast iron sample (Figure 4-16b). Honing grooves were observed running up and down at an angle. Surface pores and micro-cracks were apparent

all over the surface. Ridges were observed on the surfaces. In addition, graphite flakes were also obvious all over the surface of the cast iron sample.

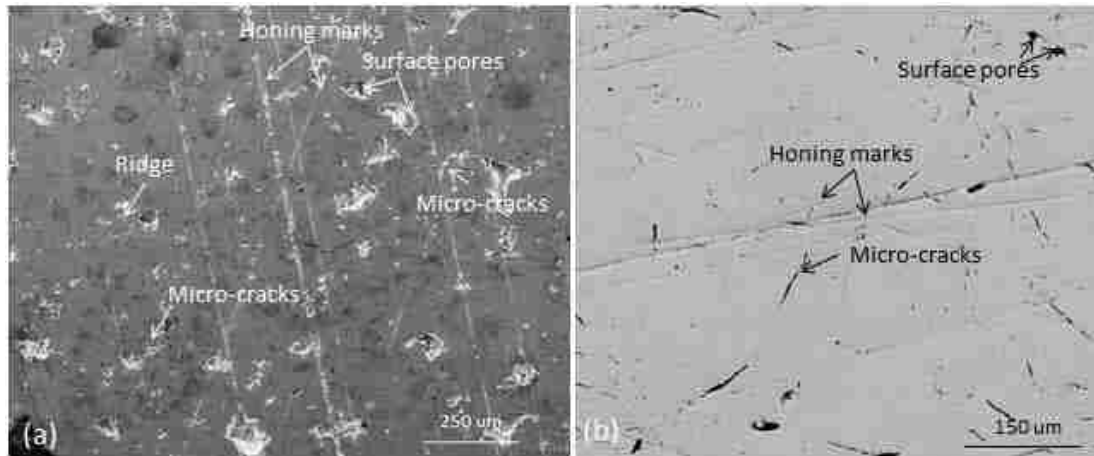


Figure 4-16 Mixed SEM image of (a) unworn surface of the PTWA-A coating, (b) unworn surface of the cast iron sample

Figure 4-17 shows detailed SEM images of the worn surface of the PTWA-A coating, showing the wear direction, surface defects, wear scars and other characteristics. Figure 4-17a shows surface texture of the PTWA-A coating after the non-firing floating-liner test. Honing grooves and wear scars of different width and length along the piston ring sliding direction were visible. The lamellae structure of the PTWA-A coating can be seen in Figure 4-17a, showing that the coating was built up layer by layer. Figure 4-17b is a back scattered (BSE) image of the selected area in Figure 4-17a and shows that the surface pores tended to merge into each other and become a large surface defect. The surface cracking can be seen and particles were ready to flake off from the surface. The particles would eventually be removed by the movement of piston ring. This indicated that the surfaces were quite weak around the pores and were good sources for removing materials. Figure 4-17c is a BSE

image that shows the removed wear debris adhered to the surface. A mixed image (Figure 4-17d) shows the beginning of a severe wear scar being formed from removed debris at the edge of a poorly adhered splat close to the surface. This wear scar started from a micro-crack, suggesting the weak edges of the micro crack would naturally deform or break off during the initial engine break-in period and cause wear of the cylinder liner and piston rings. The BSE image shows a particle scale ready to flake off from the surface (rounded area) and that the inside material was forced out of the pore resulting in deep and wide pore. An EDS spectroscopy was adopted to analysis Figure 4-18c and the result is shown below in Figure 4-18. The detection of the elements such as iron, carbon, oxide and Mn. showed the wear debris originally from the cylinder.

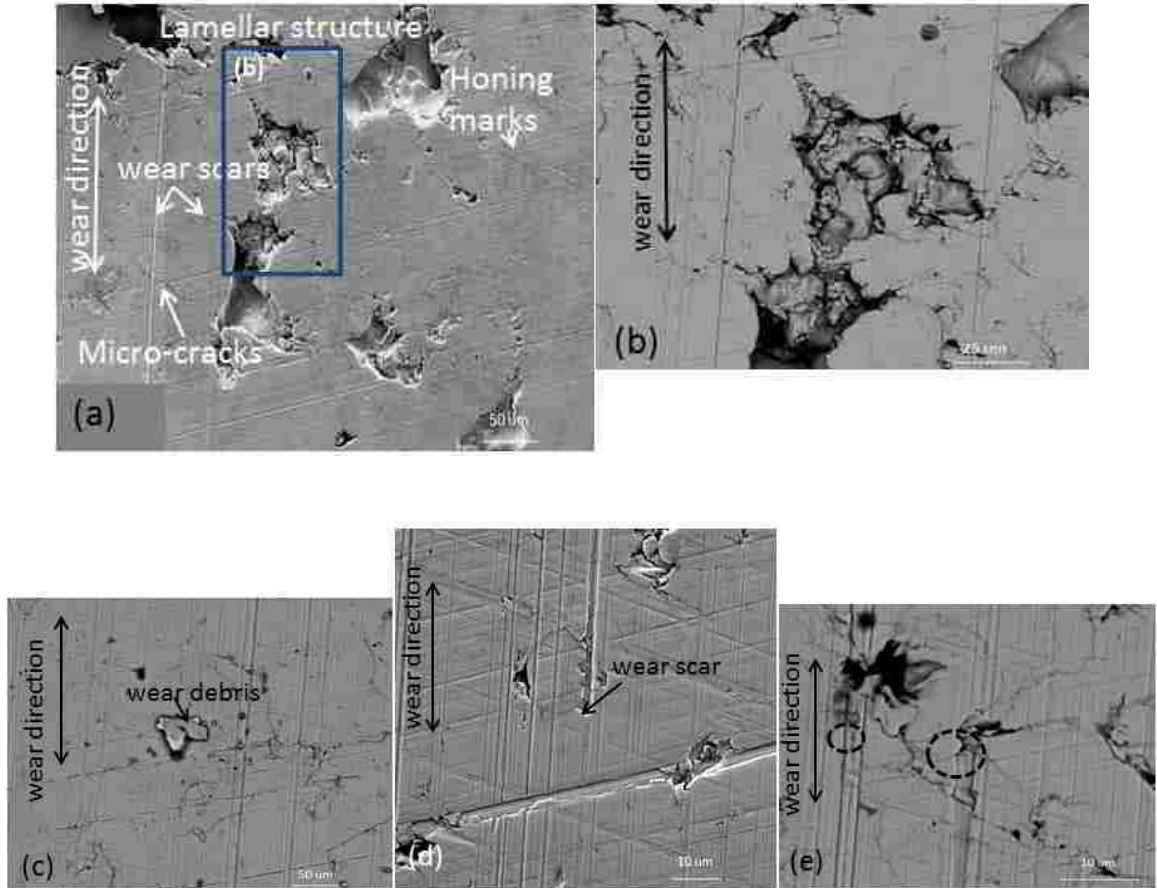


Figure 4-17 Detailed SEM images of the worn surface features of the PTWA-A coating: (a) Mixed SEM image shows the worn surface texture of the PTWA-A coating, (b) Back scattered image of the selected area in (a) shows that the surface pores tend to connect with each other and become a large surface defect. (c) BSE image shows the removed wear asperity adhered to the surface. (d) A mixed image shows the beginning of a severe wear scar. (e) BSE image shows a particle scale ready to flake off from the surface (rounded area) and the inside material was forced out of the surface resulting in deep and wide wear scars

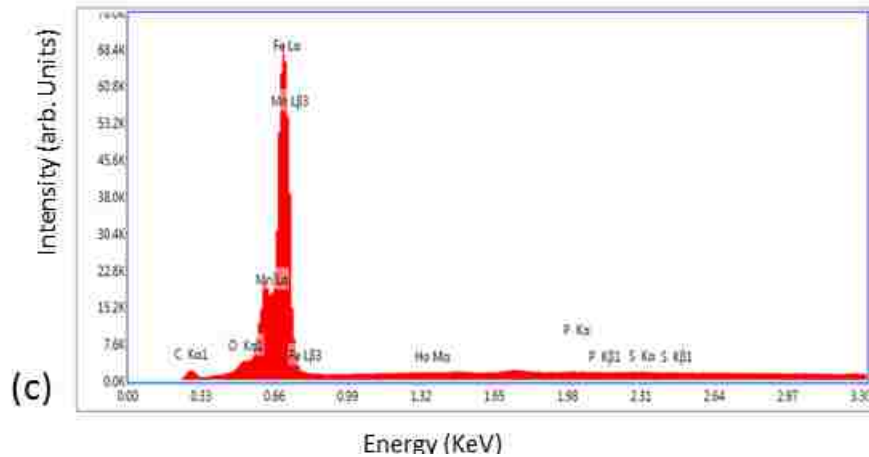
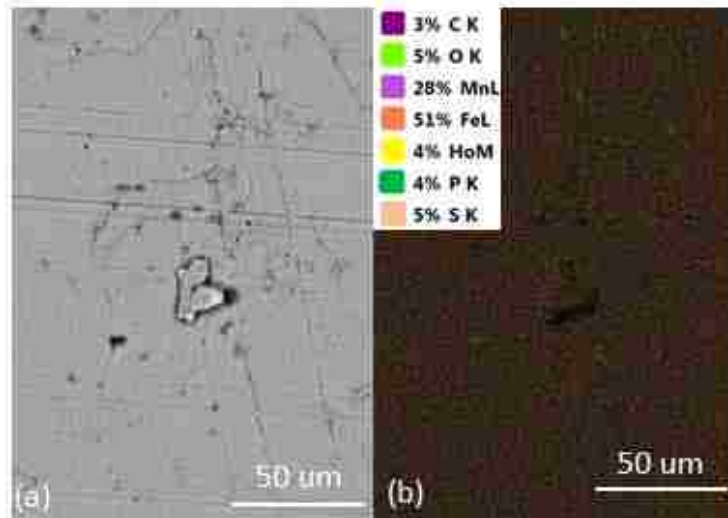


Figure 4-18 Selected area for EDS analysis (b) elements mapping results; (c) result of EDS elements analysis of the selected area

The worn surface of the cast iron sample was presented in Figure Figure 4-19. Wear direction, wear scars, micro-cracks and surface defects were all visible. Honing grooves can be seen in Figure 4-19a. The micro cracks exist around the pores suggest that the edges of pores are the weak parts of the surface (Figure 4-19b). Moreover, the graphs illustrates that wear scars started away from the honing grooves or surface pores.

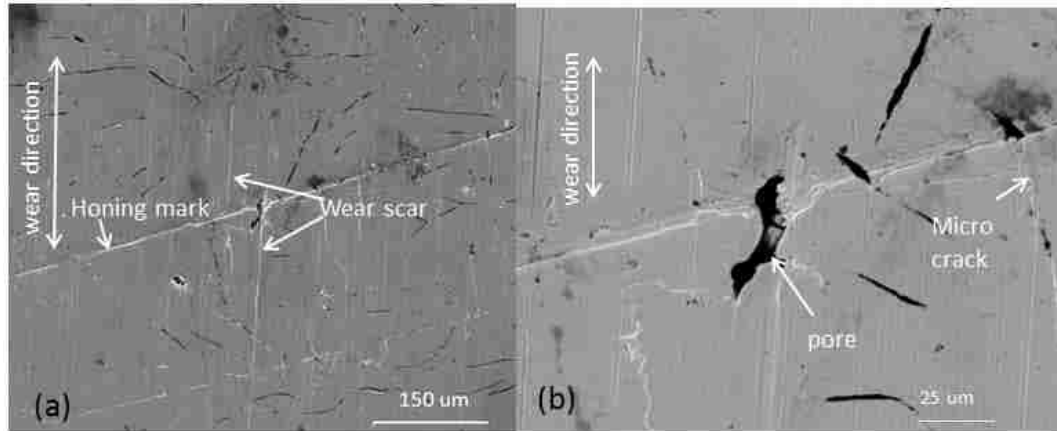


Figure 4-19 Detailed SEM images of the worn surface features of the cast iron sample: (a) The worn surface of the cast iron showing wear direction, honing marks and wear scar started away from the honing grooves or surface pores, (b) The worn surface of the cast iron showing surface pores, micro cracks and the pile-up of the materials

### 4.3.2 Cross-sectional microstructure results of PTWA-A coating engine bore

Figure 4-20 showed the cross-section microstructure of the PTWA-A coating at virgin region. In the image, the pores, micro cracks, oxides and surface pores were apparent. The coating was approximately 237.6  $\mu\text{m}$ . ASTM E-2109 was used to locate the porosity within the unworn microstructure of the PTWA-A coating. The average volume fraction of porosity within the coating was 5.8 %.

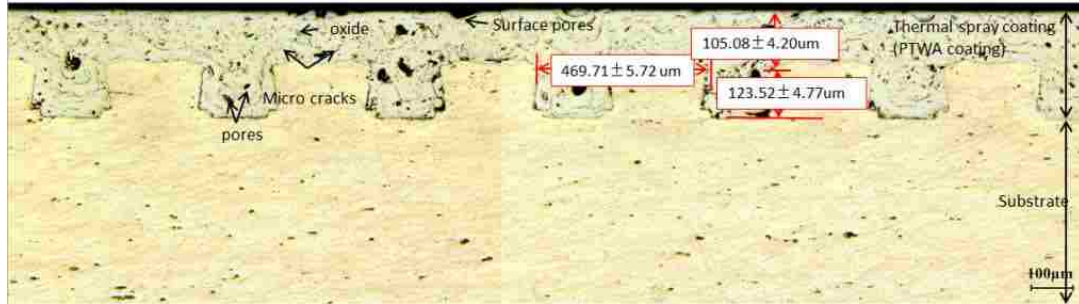


Figure 4-20 OM image shows the cross-sectional view of the unworn PTWA-A coating

Figure 4-21 shows back-scattered images and presents detailed information of the cross-section microstructure of the PTWA-A coating at virgin region. Figure 4-21 (a) is a BSE image that shows grooves and semi-circular stacking lamellae. Figure 4-21 (b) is a BSE image that shows a close-up of the semi-circular stacking lamellae of the unworn PTWA-A coating and the surface defects caused by thermal spray processes and honing process. Figure 4-21(c) is a BSE image that displays a close-up of the groove that contains the central pore and pores around interface. Figure 4-21 (d) is a close-up of the selected area in Figure 4-21 (c) and shows the presence of oxides, micro-cracks and the unmelt particles.

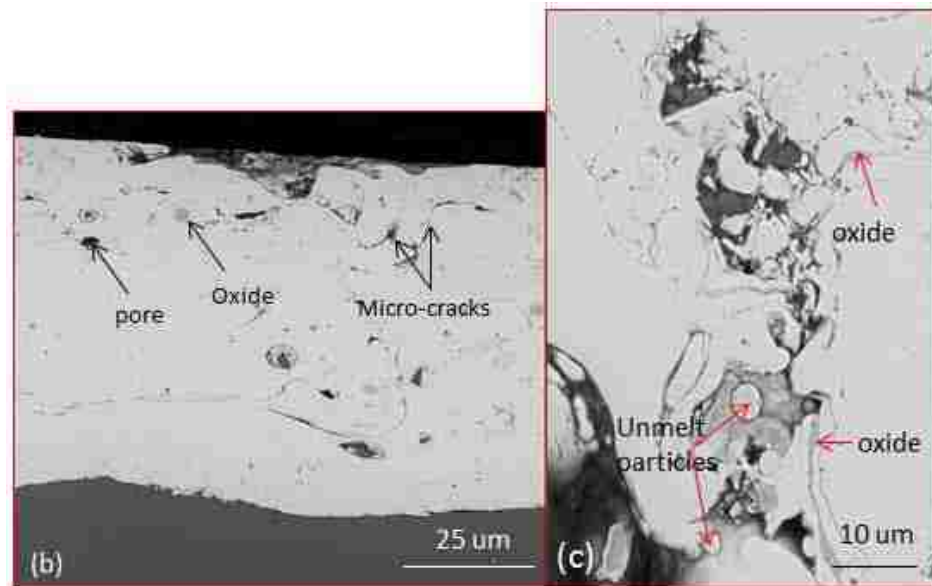
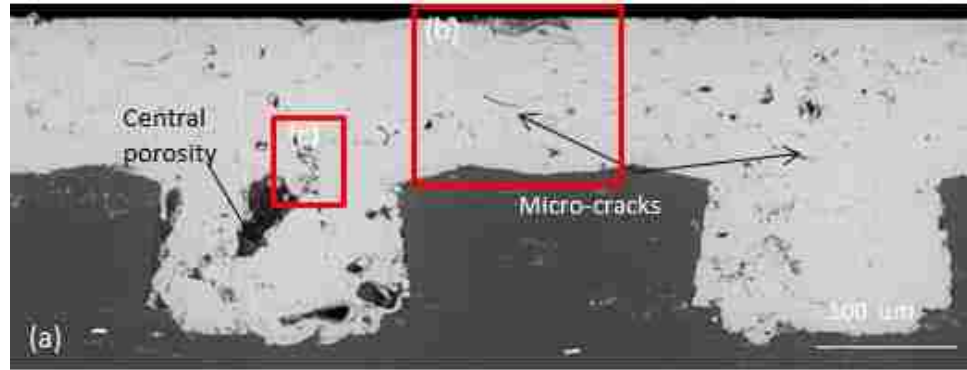


Figure 4-21 Back-scattered images giving detailed information of the cross-section microstructure of the PTWA-A coating at virgin region

Figure 4-22 establishes the EDS analysis results of central porosity in Figure 4-21(c). Figure 4-22(a) shows the selected area for EDS analysis. In Figure 4-22(b), the oxides concentrated around the edge of pore and within the pores can be seen. Figure 4-22(c) is the result of element analysis of the selected area, showing abundance of oxide within and around the central pore. It also shows the abundance of iron and the presence of carbon in this region.



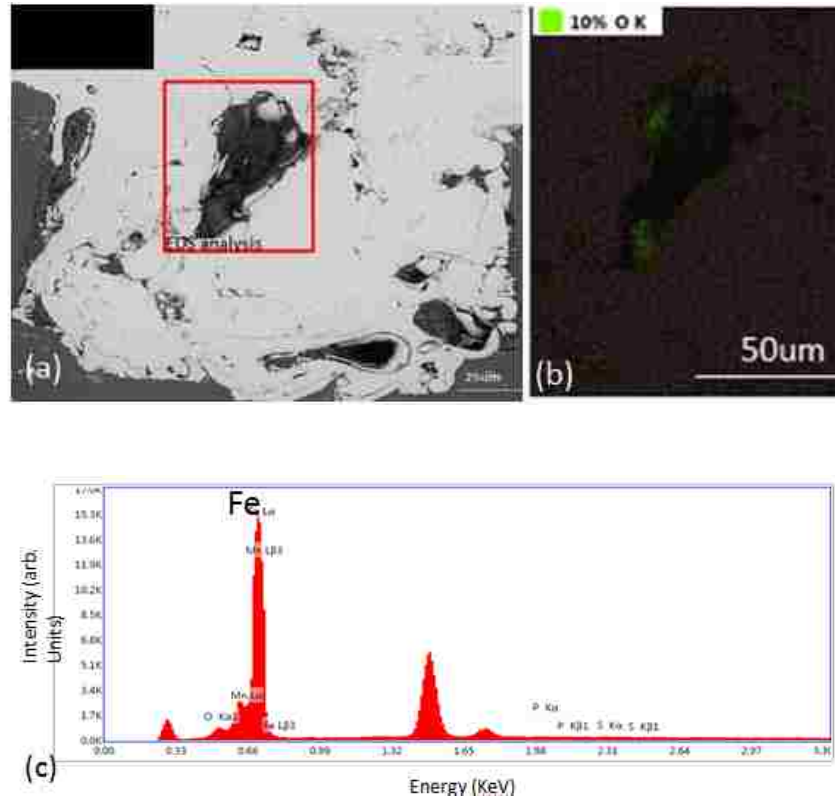


Figure 4-22 (a) Selected area of the virgin part for EDS analysis (b) oxide concentration results (c) result of EDS elements analysis of the selected area around the central pore

Figure 4-23 (a) shows the cross-sectional microstructure of the PTWA-A coating at TDC and Figure 4-23 (b) is a magnified view of the selected area. In the graphs, the gray regions were found to be oxides and the semi-circular stacking lamellae structure was obvious. The micro-cracks and pores were also apparent. Moreover, the surface at TDC displayed more defects compared to the surface of virgin area, especially in Figure 4-23 (b), where the poorly adhered, oxide-rich surface lamellae separation from the coating was evident.



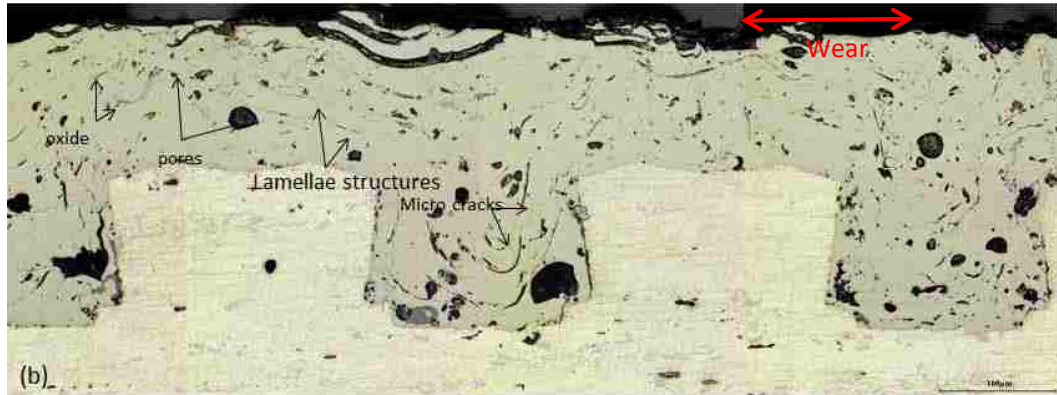


Figure 4-23 (a) OM cross-sectional view of the PTWA-A coating at TDC, (b) magnified view of the selected area showing the presence of oxides, pores, lamellae and micro-cracks

Figure 4-24(a) illustrates the selected areas at TDC for EDS analysis. Figure 4-24(b) established the oxide concentrations of the selected areas shown in Figure 4-24(a). Figure 4-24(c) and (d) are the elements analysis results of selected area 1 and 2 respectively. The result of selected area 1 indicated an abundance of oxide and iron as well as the presence of carbon in this region. The result of selected area 2 indicated abundance of iron and the presence of carbon and oxide in this region.

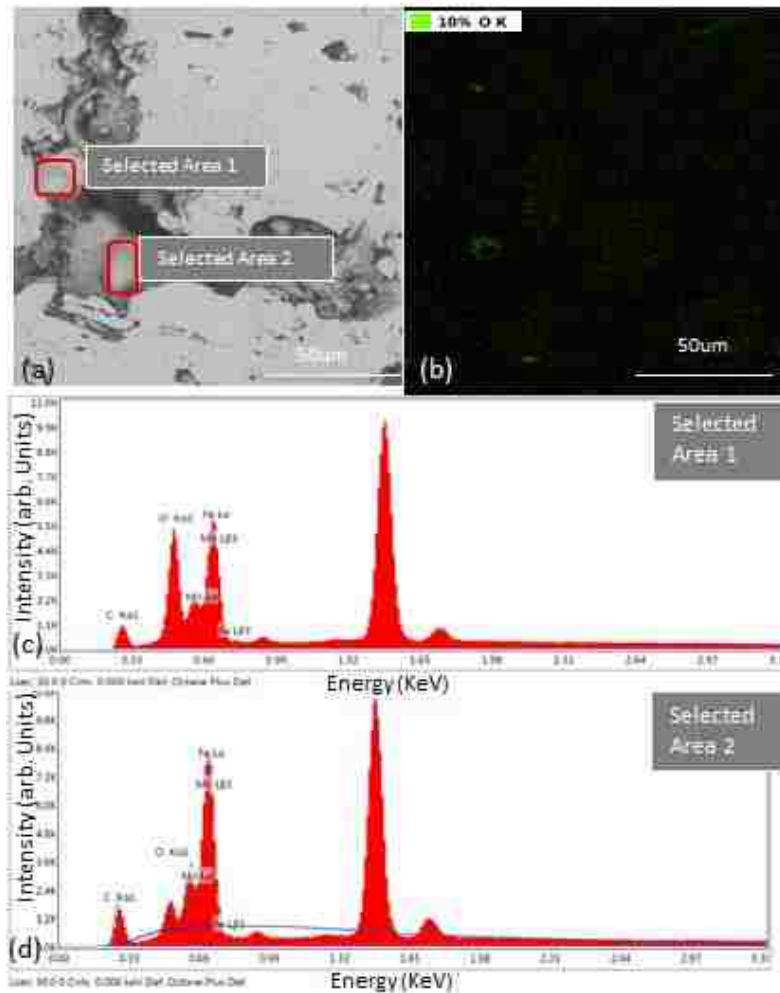


Figure 4-24 (a) Selected areas for EDS analysis (b) oxide concentration results (c)(d) results of EDS elements analysis of the selected area 1 and selected area 2 respectively

The graphs in Figure 4-25 show the cross-sectional microstructure of the PTWA-A coating at mid-stroke. Figure 4-25(a) shows the surface defects as well as a crack propagated along the semi lamellae. In addition, pores and micro-cracks were obvious within the coating. Figure 4-25(b) displays a surface pore, in which the inside material was trying to escape out of the pore. This would have resulted in the depth growing of the surface pore. Figure 4-25(c) and Figure 4-25(e) show the delamination of semi lamellae

near the surface and this was confirmed by the height scan result, shown in Figure 4-25(d) and (f) respectively.

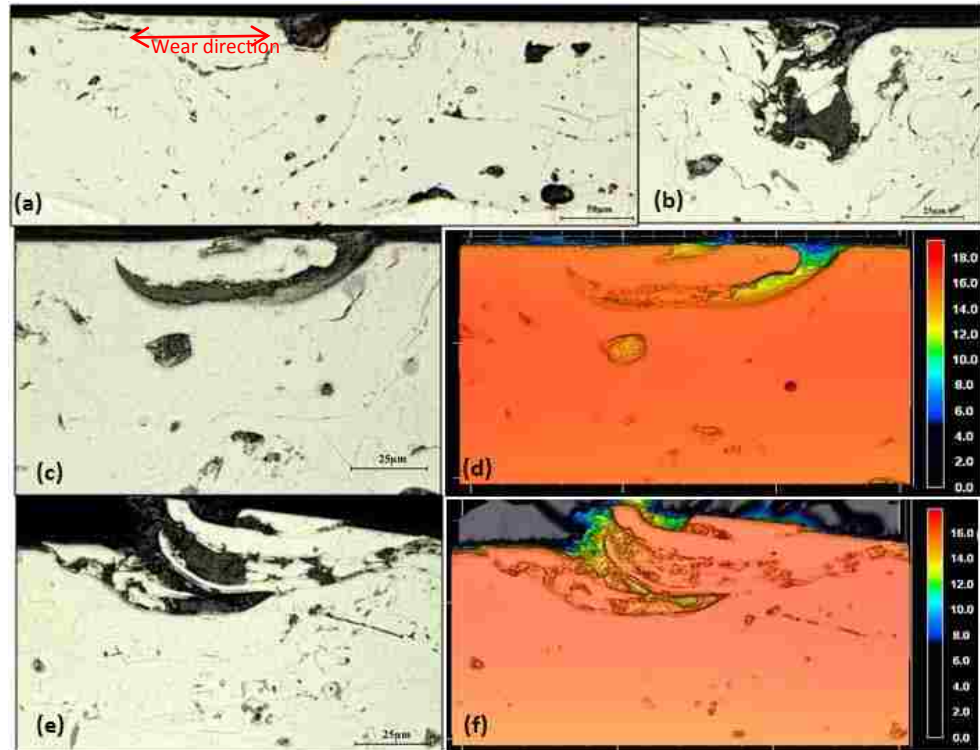


Figure 4-25 OM images showing cross-section microstructure of the PTWA-A coating at mid-stroke :( a) the surface defects as well as a crack propagated along the semi lamellae; Additionally, pores and micro-cracks are obvious within the coating. (b) The growing of a surface pore, in which the inside material was trying to escape out of the pore. (c) The magnified view of a half delaminated semi lamellae near the surface. (d) the result of the height scanning of (c), showing the semi lamellae near the surface was half delaminated.(e) The magnified view of several half delaminated semi lamellae near the surface. (f) The result of the height scanning of (e), proving the semi lamellae near the surface was half delaminated

### 4.3.3 Cross-sectional microstructure results of cast iron

The microstructures of the cast iron sample before non-firing floating-liner test and after non-firing floating-liner test were similar, except that after engine the microstructure near the surface showed some fragments fractures along the intersection of graphite and surface and material deformation on the surface. Figure 4-26(a) shows the unworn

microstructure of the cast iron sample. The cross-section view showed typical cast iron features with graphite appeared in the matrix as randomly oriented coarse distorted flakes and fine rosettes. Figure 4-26(b) is the cross-sectional view of the worn cast iron surface at TDC. It demonstrates that fractures happened along the intersection of graphite and surface. The magnified view of the fractures near surface is shown in Figure 4-26(c). Figure 4-28(d) is the cross-sectional view of the worn cast iron surface at mid-stroke. It illustrates material deformation at graphite. The magnified view of material deformation on the surface of worn cast iron at the mid-stroke was given in Figure 4-26(e).

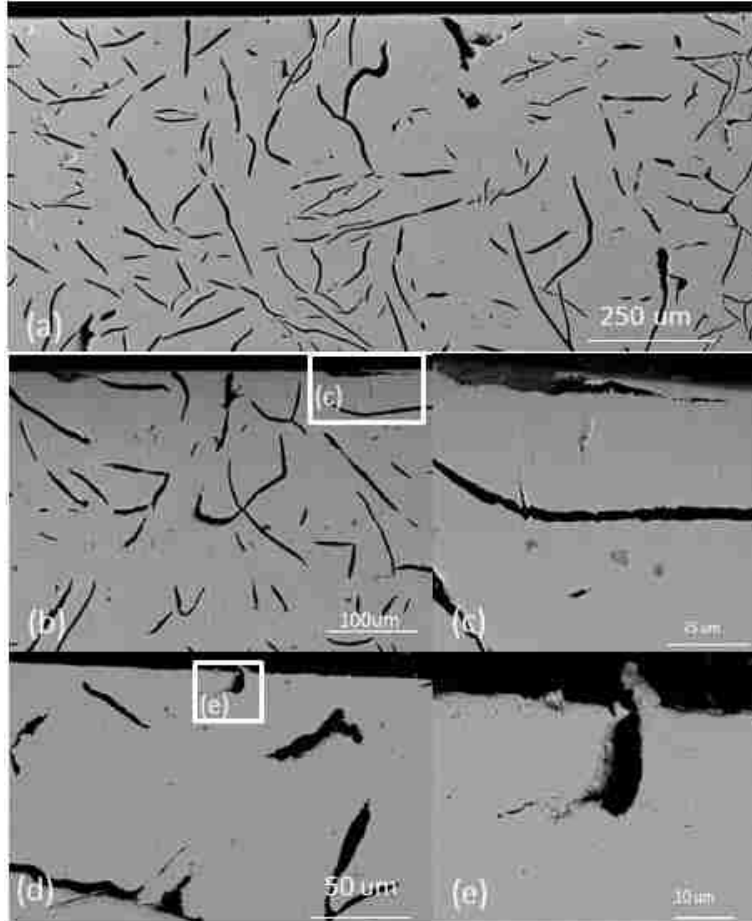


Figure 4-26 BSE images showing the cross-section microstructure of the cast iron sample (a) at virgin showing typical cast iron features while the surface is uniform; (b) at TDC, showing fractures happened along the intersection of graphite and surface; (c) Magnified view of the fracture at TDC in selected area; (d) at mid-stroke showing material deformation at graphite; (e) magnified view of material deformation on the surface of worn cast iron at the mid-stroke in selected area.

#### 4.3.4 Surface and cross-sectional microstructure analysis for PTWA-B coating

The PTWA-B coating was received as a case study to characterize the unworn part and for adhesion comparison with the PTWA-A coating engine bore. For surface features and a cross-section microstructural analysis, cross-sectional sample was prepared as discussed in section 3.5.2 and studied under optical and electron microscopes (OM, SEM/EDS).

Figure 4-27(a) is a typical secondary electron (SE) SEM image of the PTWA-B coating and shows the presence of hone marks and porosity on the surface. The back-scattered electron (BSE) view of the same location is illustrated in Figure 4-27(b).

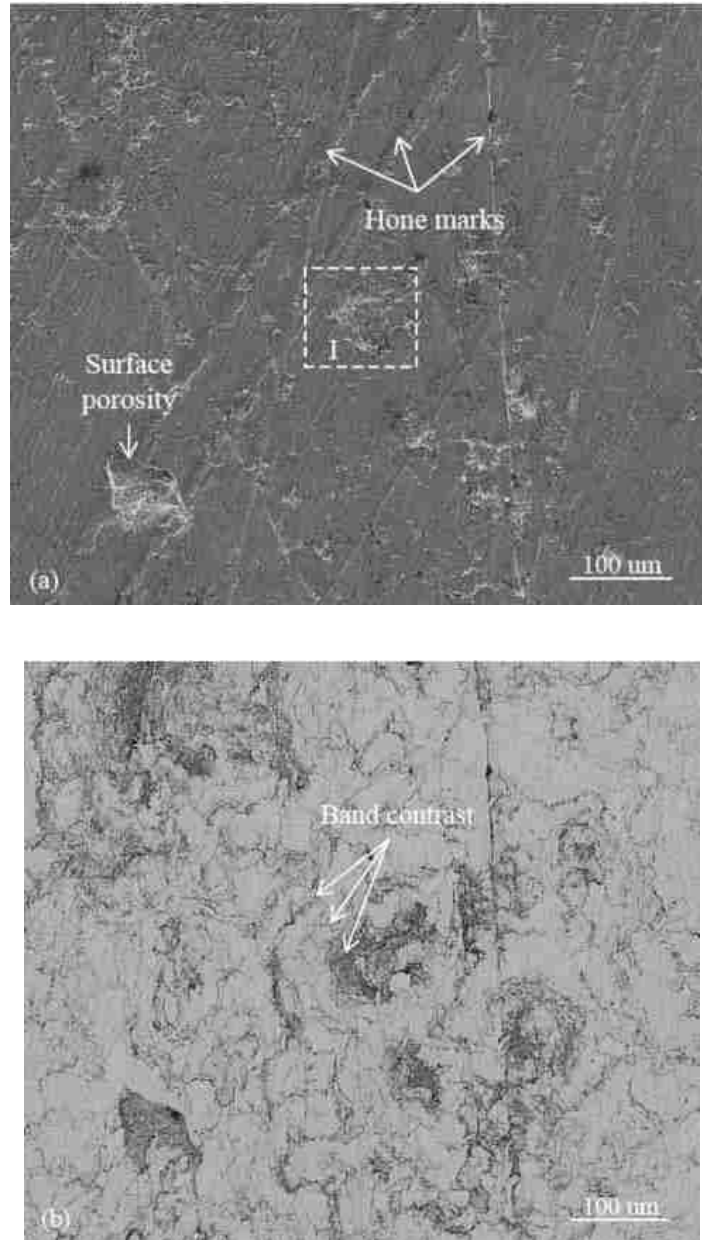
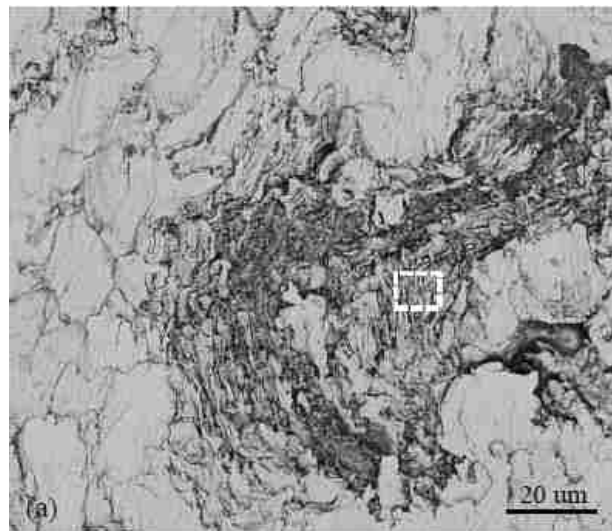


Figure 4-27 (a) A typical secondary electron (SE) image of the surface of the PTWA-B coating showing presence of hone marks and surface porosity. The enclosed location marked as "I" is where the higher magnification images shown in Figure 4-30 were taken (b) A back-scattered electron (BSE) image of the same

area shown in Figure 4-28 (a) illustrating band contrast and floret-like structure which indicates presence of two different phases in the coating (light grey and dark grey regions)

The elemental contrast in this image indicated the presence of floret-like structure and presence of two different phases in the coating (light grey and dark grey regions). Figure 4-28(a) and Figure 4-28(b) are higher magnification images of this area that show the presence of unmelted particles and layers of dark grey and light grey phases in the coating. Figure 4-28(c) is a three-dimensional optical profile of the same region shown in Figure 4-28(b). Figure 4-28(a) shows a typical back-scattered electron (BSE) image of the surface and the enclosed areas were the locations where elemental analyses, such as EDS, were performed.





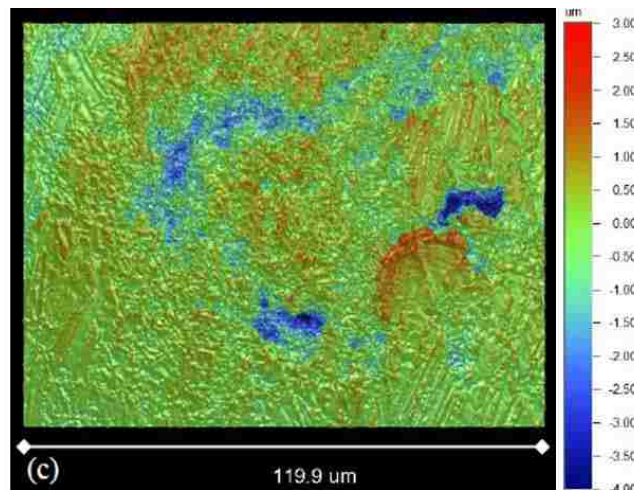
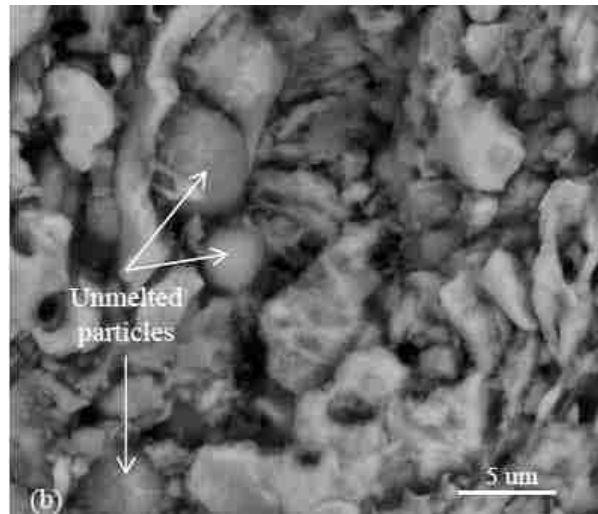


Figure 4-28 (a) Back-scattered electron (BSE) image of the enclosed area marked as “1” in Figure 2 showing the morphology of on the surface of the PTWA-B coating, the enclosed area is the location where higher magnification image shown in “b” was taken. (b) A back-scattered electron (BSE) image of the enclosed area marked in “a” showing presence of unmelted particles within this region. (c) A 3D-optical profile of the area selected in “a”

Figure 4-29(b) shows the EDS spectrum collected from “selected area 1” and “selected area 3” and highlights the abundance of iron and presence of carbon in these regions. Figure 4-29(c) shows the EDS spectrum corresponding to “selected area 2” and illustrates the abundance of iron and oxygen and the presence of carbon in this region.

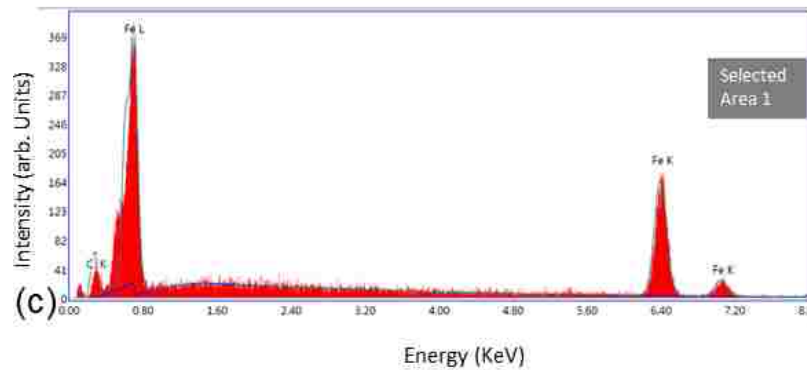
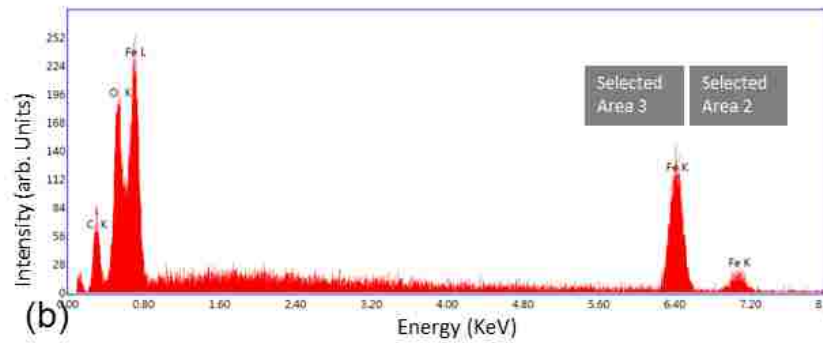
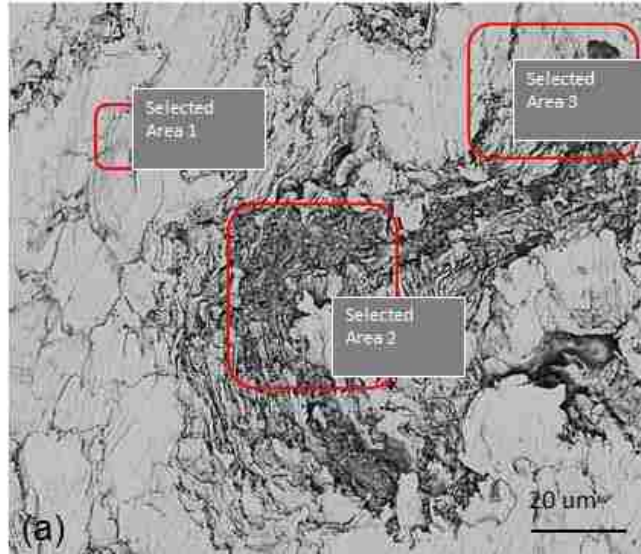


Figure 4-29 Back-scattered electron (BSE) image of the surface: The enclosed areas are the locations where elemental analyses (e.g., x-ray energy dispersive spectrometry (EDS)) was performed. (b) EDS spectrum collected from “selected area 1” and “selected area 3” showing abundance of iron and presence of carbon in these regions. (c) EDS spectrum corresponding to “selected area 2” showing abundance of iron and oxygen and presence of carbon in this region

Figure 4-30 shows typical secondary electron (SE) images of the honed surface of the PTWA-B coating bore. Features such as cutting chip-like and micro cracks were observed on the surface. For cross-sectional microstructural analysis of the coating, the sample was cut using a low-speed diamond saw and mounted in an epoxy. Conventional metallography procedure for ferrous alloys was followed and the (unetched) microstructure was investigated under optical and scanning electron microscopes.

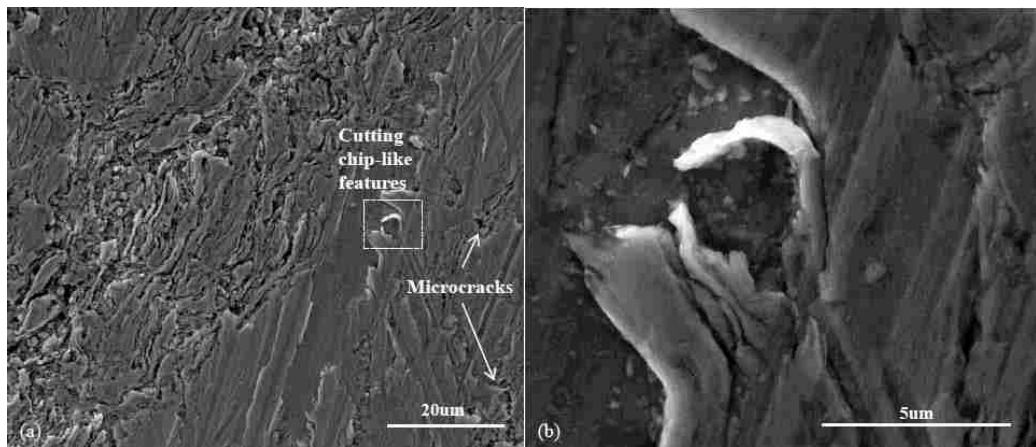


Figure 4-30 (a) A typical secondary electron (SE) image of the honed surface of the coating showing presence of cutting chip-like features and micro cracks. The enclosed area is the location where higher magnification image shown in “b” was taken. (b) SE image of the area marked in “a” showing the cutting chip-like features on the honed surface.

Figure 4-31(a) shows a typical cross-sectional back-scattered electron SEM image of the PTWA-B coating on the Al substrate. The layered structure of the coating and presence of porosity are some of the features evident in this image. The coating thickness was measured at  $490.0 \pm 9.6 \mu\text{m}$  using an image analyzing software. Porosity in the form of voids and micro-voids were observed within the coating. The coating had a lamellar microstructure consisting of light grey splats and dark grey veins were observed between the splats. Moreover, the presence of unmelted particles and micro-cracks within the dark

grey phase were also observed within the intersplat regions. Figure 4-31(b) shows the presence of unmelted particles, porosity and dark grey veins in the intersplat regions, while Figure 4-31(c) shows the presence of micro-cracks within the dark grey phase in the intersplat region. ASTM E-2109 was used to locate the porosity within the microstructure. The average fraction of porosity within the coating was 2.5 %.

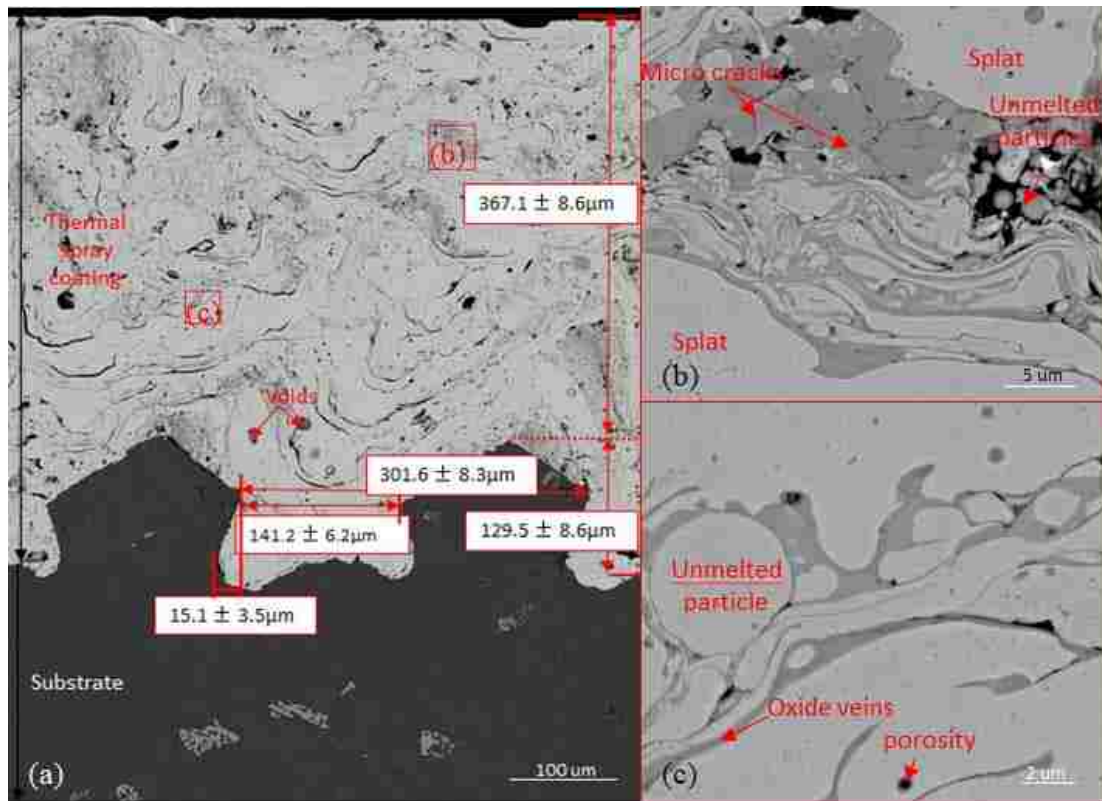


Figure 4-31 (a) Cross-sectional back-scattered electron SEM images of the PTWA-B coating on the Al substrate: The coating had a dovetail morphology interface with the aluminum substrate. The layered structure of the coating is evident from the images (b) presence of unmelted particles, porosity and dark grey veins in the intersplat regions, (c) presence of micro cracks within the dark grey phase in the intersplat region

Elemental analysis revealed that the light grey regions were rich in iron in the form of steel splats and that the dark grey regions were rich in oxygen and iron, possibly as a result of the iron oxide phase. The EDS map obtained from the location shown in Figure

4-32(a) was given in Figure 4-32(b). The corresponding EDS spectra of the iron-rich splats and oxygen-rich areas between the splats were also given Figure 4-32(c) and Figure 4-32(d).

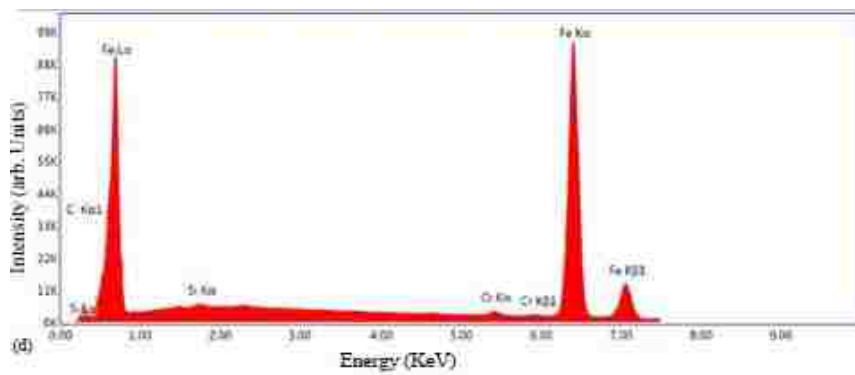
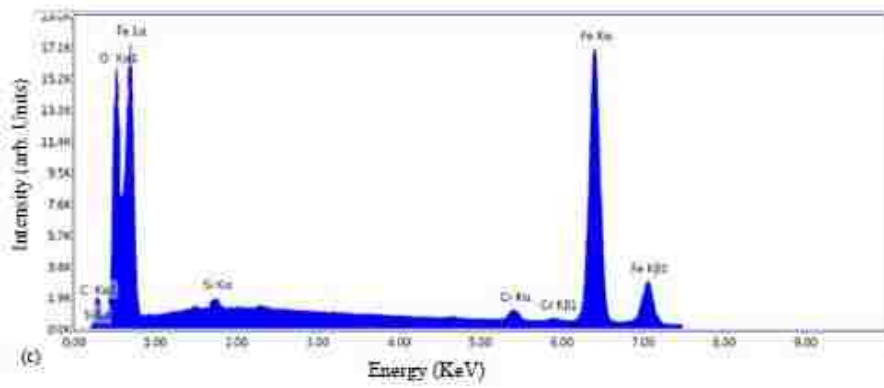
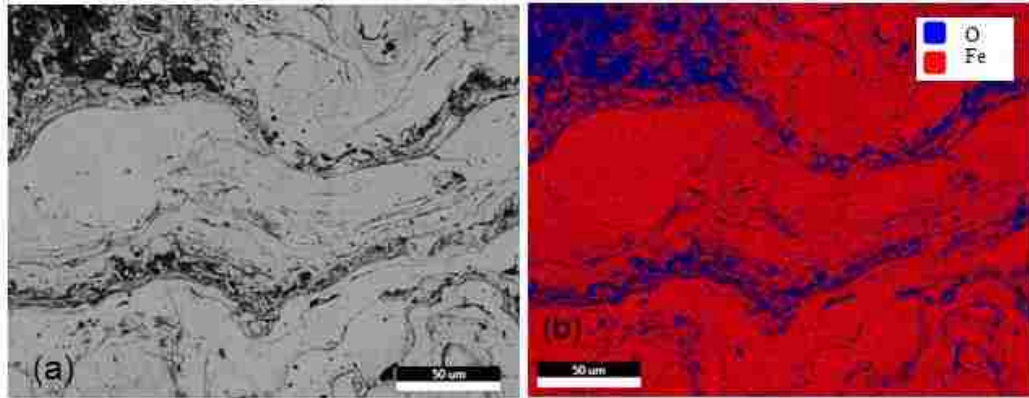


Figure 4-32 (a) A cross-sectional microstructure (back-scattered SEM image) of the PTWA-B coating, (b) corresponding energy dispersive x-ray spectroscopy (EDS) map of the same area showing that the light areas were rich in iron and the dark grey regions consisted of oxygen. (c), (d) Typical EDS spectra of the O-rich (blue)

and Fe-rich (red) regions indicating that the O-rich veins consisted of iron oxides and the Fe-rich regions were steel splats

#### 4.4 Hardness tests

Macro-hardness measurements on the surface were carried out using Rockwell B scale testing according to the ASTM E18 standard based on seven measurements. The average hardness value of the PTWA-A coating was  $71.71 \pm 3.44$  HRB, while the average hardness of cast iron was  $79.78 \pm 9.37$  HRB. It was also found that the average hardness of the PTWA-B coating was  $90.4 \pm 0.3$  HRB, and the depths of the indents of PTWA-A coating, cast iron, and PTWA-B coating were 0.116 mm, 0.100 mm, and 0.079 mm respectively.

#### 4.5 Adhesion tests

PTWA-A coating and PTWA-B coating were subjected to adhesion testing. The adhesion strength of the coatings was evaluated according to ASTM C633 using a uniaxial tensile machine as discussed in section 3.5.4.

The coating thickness of the PTWA-A coating was approximately 240  $\mu\text{m}$  with an average fraction of porosity within the coating of 5.8 %. The average hardness value was  $71.71 \pm 3.44$  HRB. The coating thickness of the PTWA-B coating was about 500  $\mu\text{m}$  with an average fraction of porosity within the coating of 2.5 %. The average hardness value was  $90.4 \pm 0.3$  HRB.

The adhesion test results revealed that the failure for the PTWA-B coating occurred at 4.4 kN of the applied load, corresponding to a bond strength (i.e., (failure load)/ (failure area)) of 44 MPa. The cohesive failure and adhesive failure for the PTWA-A coating

occurred at 1.951 kN applied load (corresponding to 19.51 MPa) and 2.903 kN applied load (corresponding to 29.03 MPa) respectively. The results are tabulated in Table 4-1.

Figure 4-33 shows that the stereo micrographs of the failed surfaces indicate that the coating was detached from the aluminum substrate at the coating/substrate interface (i.e., adhesive type of failure). Figure 4-33(a) is a top view of the failed surface and illustrates the keyhole pattern made on the aluminum prior to the deposition of the PTWA-B coating. Figure 4-33(b) is a side view of the failed surface and shows the detachment of the PTWA-B coating from the substrate at the coating/substrate interface and Figure 4-33(c) is a high magnification view of the failed surface shown in “b” that illustrates the detachment of the coating at the aluminum substrate interface and the keyhole pattern made on the Al surface prior to the coating deposition. Figure 4-34 shows that the coating was detached from the aluminum substrate in PTWA-A coating at the coating/substrate interface (i.e., adhesive type of failure). Additionally, Figure 4-35 highlights the failure happened within the coating in PTWA-A coating (i.e., cohesive type of failure). Figure 4-35(a) offers a top view of the failed surface showing the failure on PTWA-A coating, while Figure 4-35(b) offers a side view of the partial detachment of the PTWA-A coating from the substrate.

Table 4-1 Results of adhesion pull tests

<b>Samples</b>	<b>Failure load( kN)</b>	<b>Failure strength (MPa)</b>	<b>Failure type</b>
PTWA-B coating	4.4	44	Adhesion failure
PTWA-A coating (test #1)	2.903	29.03	Adhesion failure

PTWA-A coating (test #2)	1.951	19.51	Cohesion failure
--------------------------	-------	-------	------------------

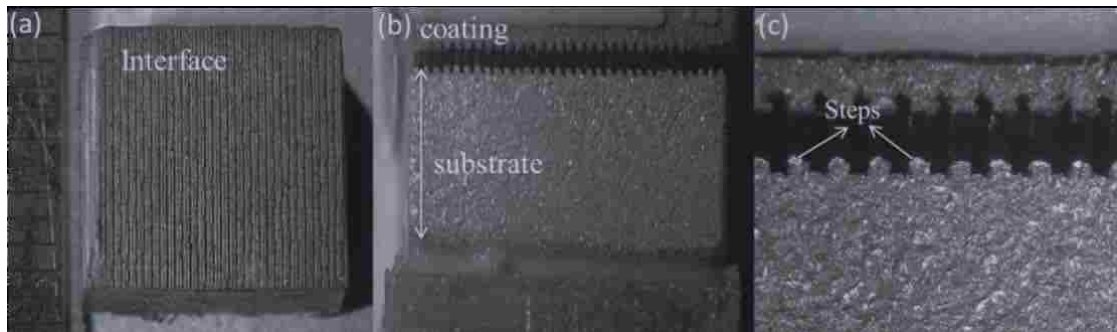


Figure 4-33 Stereo micrographs taken from the failure surfaces of the PTWA-B coating. (a) Top view of the failed surface showing the keyhole pattern made on aluminum prior to the deposition of the PTWA-B coating, (b) side view of the failed surface showing the detachment of the PTWA-B coating from the substrate at the coating/substrate interface; (c) a high magnification view of the failed surface shown in “b” illustrating the detachment of the coating at the aluminum substrate interface and the keyhole pattern made on the Al surface prior to the coating deposition.



Figure 4-34 Adhesive failure surface of PTWA-A coating: (a) Top view of the failed surface, (b) side view of the failed surface showing the coating/substrate interface

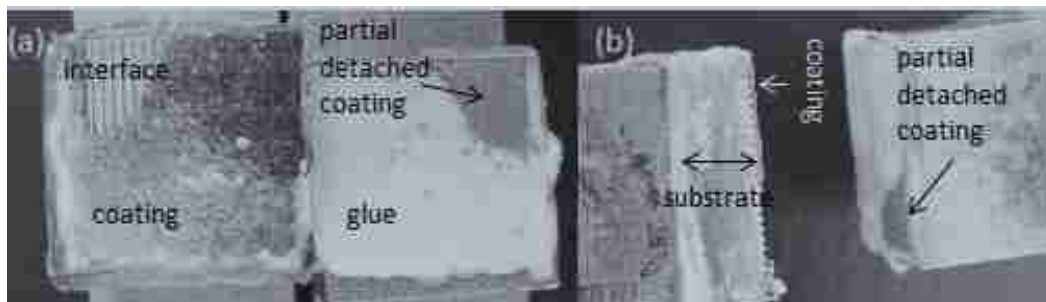


Figure 4-35 Cohesive failure surface of PTWA-A coating (a) Top view of the failed surface showing the failure on PTWA-A coating, (b) side view of the partial detachment of the PTWA-A coating from the substrate



## CHAPTER 5 DISCUSSION

This section discusses the results obtained during this research investigation. The first section encompasses the results obtained during observation of the surfaces and cross sectional microstructure to study the wear mechanisms. The second section includes the lubrication conditions. In the remaining sections, the comparison between the PTWA-A coating bore and the PTWA-B coating bore are given in order to address the possibility of putting the PTWA-A coating engine bore in to production.

### 5.1 Sliding Behavior of PTWA-A coating engine bore in comparison with Cast Iron engine bore

The friction force of the PTWA-A coating engine bore (the initial friction force of the PTWA-A coating engine bore was 230 N) was lower than that of the cast iron engine (the initial friction force of the cast iron engine was 269 N). The surface roughness of the PTWA-A coating engine bore showed higher core roughness depth, higher reduced peak height and higher reduced valley depth compared to that the cast iron engine both before and after the non-firing floating-liner tests (Figure 4-5, 6). The parameters of roughness illustrate that the surface of the PTWA-A coating engine bore has sharp asperities and deep pores. The surface of the PTWA-A coating engine bore is more capable of storing oil than the cast iron sample. This demonstrates that the rougher and porous surface helps the PTWA-A coating engine store oil and in turn provides better lubrication and protects engine.

The friction force of the PTWA-A coating engine bore is stable (approximately 205 N) with some fluctuations after the break-in period. However, the friction force of the cast iron engine decreases dramatically (269 N to 190 N) (Figure 4-15). The porous surface of the PTWA-A coating engine bore helps decrease friction force in break-in period. This proves that the roughness is needed only in the early stages of engine operation to enhance the removal of cylinder wall and ring material in places of high interference between these components to produce conformity between each [46]. Therefore, roughness allows an initial high wear rate.

The depths of valleys on the engine surface influence the oil retention capacity. As the surface valley parameter determines the volume of oil reserve, increasing the depth of the valleys, the oil retention capacity would be increased [40]. The surface of the PTWA-A coating engine bore (number of pores at TDC and mid-stroke were  $703.50 \pm 131.70$  and  $677.00 \pm 32.76$  before the non-firing floating-liner tests), when compared with the cast iron surface shows porous structure. This porous microstructure of the PTWA-A coating engine bore results in an increased lube oil consumption and exhaust emission of soot and particles, carbon oxides and hydrocarbons during the non-firing floating-liner test [40]. Oil retention volumes of the PTWA-A coating engine bore are higher than that of the cast iron engine, which means there was higher oil consumption and greater emission of CO and HC during non-firing floating-liner tests.

The surface of the PTWA-A coating engine bore contributes to the low friction force of the PTWA-A coating engine bore during the non-firing floating-liner tests. This low and

constant friction force of PTWA-A coating engine bore makes it a promising replacement for the traditional cast iron engine. However, the rough and porous surface results in higher oil consumption and exhaust emission of soot and particles, carbon oxides and hydrocarbons of the PTWA-A coating engine bore. This has to be solved in replacing the tradition cast iron engine.

### **5.1.1 Wear mechanism**

Honing marks are observed running up and down at an angle in the unworn surface morphology (Figure 4-1, 3, 16). The honing marks are produced to store oil, which in turn improve the lubrication condition. The honing grooves also trap wear debris (Figure 4-19) to remove them from the contact interface between the cylinder wall and the piston during piston movement [57].

Micro cracks are presented in different directions suggesting that micro cracks are not only created by the honing process but also during the manufacturing processes. The honing process also reveals the micro cracks generated in manufacturing processes, especially on the cast iron bore surface, on which the micro cracks are the graphite flakes revealed by the honing processes (Figure 4-19, 27).

The wear scars on the worn surfaces (Figure 4-17, 19) shows that wear scars with different width and length are produced along the wear direction (piston sliding direction) after the non-firing floating-liner tests. Wear debris is found “sitting” on the worn surfaces, which indicates that wear scars are actually abrasive scratches parallel to the ring motion

direction. The wear that occurred during the non-firing floating-liner tests can be attributed to abrasive wear.

In the normal wear region, the peaks on the surface were broken off during the break-in period, then the piston, the broken off debris and the cylinder wall surface formed a three-body abrasive wear. The wear debris was free to roll and slide between the two sliding surfaces or was carried by the piston at every stroke resulting in wear on surface of the cylinder. The ploughed and piled aside ridges and micro-cracks were also observed (Figure 4-16) along the honing grooves produced during the honing process and around the pores. The ploughed-aside ridges and micro cracks were partially worn and partially plastic deformed. This proves that the folded materials created by manufacturing and honing processes are the weakest points on the surface, which are the first to be worn off during non-firing floating-liner tests. The breaking-off folded materials along the honing grooves and weak edge materials around the pores act as the debris in abrasive wear between engine bore surface and piston surface [51]. The abrasive wear mechanism is the principal wear mechanism for the PTWA-A coating engine bore and cast iron engine bore during the non-firing floating-liner tests.

However, it was observed that the pores on the PTWA-A coating engine bore surface merged into each other after the non-firing floating-liner test (Figure 4-17) and became a large surface defect. Thus, material from inside the pores was forced out of the surface, i which is demonstrated by the increase of  $S_{vk}$  after the non-firing floating-liner test. As a

result, deep and wide wear scars formed. This is because the reciprocating motion creates a changing stress field [59] underneath the surface in the internal combustion engine system.

The forming of large surface defects initiates surface cracks, which propagate along the splat boundaries during the non-firing floating-liner tests (Figure 4-17). The cross-section microstructures clearly show that the near surface splats at normal wear region are gradually flaked off the coating. Moreover, the cross-section view of the surface appears to be more damaged than the virgin surface, which was caused by the splat delamination. This was also demonstrated by the height scanning results (Figure 4-26), which show that gaps exist between the splats and coating. Eventually, micro cracks can result in the top lamellar flaking off the coating surface. In addition, the smooth layers within the PTWA-A coating hinder the interlocking between layers, which leads to the failure of preventing the removal of the whole splat particle from the substrate.

This surface delamination corresponds to splat delamination wear. The failure of the PTWA-A coating engine bore surface is initiated by the undersurface shear stresses and enhanced by the surface defects produced during the manufacturing and honing processes [58].

The wear of the cast iron engine is attributed to abrasive wear. The peaks on the surface of cast iron engine bore were removed in the break-in period and formed a three-body abrasive with the two counterfaces. The wear of the PTWA-A coating engine bore is attributed to the co-work of abrasive wear and splat delamination wear. The peaks on the surface, the weak ridges around the honing grooves, and surface pores are removed,

resulting in abrasive wear. The abrasive wear debris and the extreme loading condition of the engine bore accelerate the propagation of cracks, resulting in the splat delamination wear. The flaked off splats would, in turn, enhance the abrasive wear as particles.

### **5.1.2 Lubrication conditions**

The lubrication condition influenced the wear behavior of the engines during the non-firing floating-liner tests. The cross section microstructure of the PTWA-A coating engine bore after the non-firing floating-liner test showed a more damaged surface at TDC than that at mid-stroke. The pressure at TDC is higher than that at mid-stroke and the speed is lower at TDC than that at mid-stroke. This results in lubrication starvation at TDC.

At TDC, speed decreases to zero and the pressure that is generated in the lubrication gap squeezes the lubricated oil out of the gap [39]. In this situation, the oil film thickness is less than the surface roughness, the metal-to-metal contact occurs, and because the contact area between the two surfaces is limited to the contacting peaks of the asperities, a mixed lubrication mechanism is observed. As a result, there is an occurrence of abrasive wear caused by the rubbing the hard piston-ring surface or the hard particles in the lubricate oil. While at mid-stroke, the piston increased to the maximum speed, a hydrodynamic lubrication mechanism was observed, and the surface was lubricated enough. Upon competition, the wear was less severe than at TDC.

The friction force result of the cast iron engine shows continuous decrease after the break-in period, which is attributed to the feeding of graphite flakes during the non-firing

floating-liner test. The lubricate condition of the cast iron engine changes from oil lubricate to oil plus graphite lubricate after the break-in period, while the lubricate condition of the PTWA-A coating engine bore is oil lubricate throughout the non-firing floating-liner test.

## 5.2 Evaluation of adhesion strength

The three most common failure types found in adhesion tests are epoxy failure, cohesive failure, and adhesive failure. When the failure happens within the adhesive film, it is epoxy failure. When the failure happens within the coating, it is called cohesive failure. When the failure happens at the coating and substrate interface, it is referred as adhesive failure.

The adhesion test results of the PTWA-A coating show two types of failures happened in the tests. One failure happened at the interface between coating and substrate, corresponding to an adhesive type of failure and one failure happened within coating, corresponding to a cohesive type of failure. The adhesion strength was 29.03 MPa and adhesion strength was 19.51 MPa. The result of the B sample shows that the failure happened at the interface between coating and substrate, corresponding to an adhesive type of failure. The adhesion strength was 44 MPa. It is clear that the PTWA-B coating has higher adhesion strength than the PTWA-A coating.

The presence of hone marks and surface porosity are observed on the virgin surfaces of the PTWA-A coating and the PTWA-B coating. The layered structures and presence of porosity are evident in the cross-sectional microstructural analysis of both samples. The presence of unmelted particles, micro cracks, and oxides are also clear. The PTWA-B

coating has a dense coating with an average fraction of porosity within the coating of 2.5 %. However, the PTWA-A coating shows more porous coating with an average fraction of porosity within the coating of 5.8 %, especially along the interface between coating and substrate. In addition, the grooves of the PTWA-B coating are machined to match a tooth-like shape with round corners, which allows a wider angle for the gun head that sprays more evenly and provides better adhesion during the thermal spray process.

The cohesion failure of the PTWA-A coating is attributed to the pores and micro-cracks in the coating. During the adhesion tests, a tension load applies perpendicular to the coating, resulting in stress concentration around those defects. The cracks would propagate easily around those defects as the areas around defects are weaker and bear more comparisons to the defect-free areas. As a result, failure happens and partial coating is pulled off the main coating.

The adhesion strength measures the bond between the coating and substrate. The tension load applies perpendicular to the coating and tries to break the mechanical interlock between coating and substrate. When compared to the PTWA-B coating, more pores and micro cracks are observed along the interface between coating and substrate in the PTWA-A coating. This means the coating of the PTWA-A sample poorly adheres to the substrate.



## CHAPTER 6 CONCLUSIONS

### 6.1 Conclusions

The lubricated sliding behaviour and wear mechanisms of the PTWA-A coating deposited on aluminum engine after the non-firing floating-liner test were studied and compared to traditional cast iron engine bore. The microstructures of surface and the cross-section of coated engine bores were analyzed before and after the non-firing floating-liner tests. The following conclusions are presented:

- The microstructure of the PTWA coating shows a lamellae structure in which splats, pores, oxides, and unmelt particles were embedded. The thickness of PTWA-A coating is approximately 237.6  $\mu\text{m}$  and the volume fraction of porosity within the coating is 5.8%.
- The PTWA-A coating engine bore shows lower friction force (the initial friction force of the PTWA-A coating engine bore is 230 N) when compared to the cast iron engine bore (the initial friction force of the cast iron engine is 269 N). This is attributed to the surface porosity and the surface roughness of the PTWA-A coating. The average number of pores for PTWA-A coating engine bore at TDC and mid-stroke are  $703.50 \pm 131.70$  and  $677.00 \pm 32.76$ . The  $S_{vk}$  of PTWA-A coating engine bore at TDC and mid-stroke are  $1.872 \pm 0.513 \mu\text{m}$  and  $1.705 \pm 0.102 \mu\text{m}$ . Surface porosity serves well for oil storage and helps the PTWA-A coating engine bore improve the lubrication condition.

- The oil retention volume of the PTWA-A coating engine bore is larger than that of cast iron. This suggests that the PTWA-A coating engine bore consumes more oil and produces more emission compared to the cast iron engine bore.
- The micromechanisms of wear for PTWA-A coating engine bore:
  - 1) The wear is initiated by abrasive wear. Surface peaks, weak edges of cracks, and pores are removed during the break-in period and become wear debris while creating wear scars on the surface.
  - 2) The wear is then enhanced by splats separation, which is caused by the propagation of cracks at splat interfaces along the oxides. The PTWA coating layers are removed as a result of surface fatigue and act as the third body particle in later abrasive wear process.
- The PTWA-A coating with an interfacial morphology of square shape shows the adhesion strength of 29.5 MPa, however, PTWA-B coating with an interfacial morphology of dovetail shape shows much higher adhesion of 44 MPa. This suggests the adhesion strength of PTWA coating depends on the shape of the pre-machined interfacial morphology prior to the thermal spray processes and it can be improved by changing the interfacial morphology.

The work presented in this thesis has shown that the PTWA-A coating engine bore does have the promising potential to replace cast-iron cylinder liners in production vehicles, although some improvements are needed for the coating processes. It is remarkable that the friction force of the PTWA-A coating engine bore is lower than that of the traditional

cast iron engine bore. In addition, this research has provided insight into the wear mechanisms of the PTWA-A coating engine bore. Moreover, a specific design criterion for thermal spray coated Al-Si engine has been developed by comparing the PTWA-A coating engine bore with the PTWA-B coating engine bore. This suggests the pre-machined grooves on the substrate need to be shaped with round corners and wide angles to provide better mechanical interlocks for the coating.

## 6.2 Recommendations for future research

The following work is suggested for future research:

- Microstructural and chemical analysis of piston rings can provide more insight into the wear mechanism of the coating.
- No obvious wear was present but it would be valuable to check the time dependant wear volume of the PTWA-A coating engine bore. This would help to quantify wear results of the PTWA-A coating engine bore.

## REFERENCES

- [1] Lenny Jr J. Replacing the cast iron liners for aluminum engine cylinder blocks: a comparative assessment of potential candidates[D]. Rensselaer Polytechnic Institute, 2011: 2-3.
- [2] Bobzin K, Ernst F, Zwick J, et al. Coating bores of light metal engine blocks with a nanocomposite material using the plasma transferred wire arc thermal spray process[J]. *Journal of Thermal Spray Technology*, 2008, 17(3): 344-351.
- [3] Nylén P. Applications of thermal spray technology for aerospace and automotive industry[C]//1st International Conference and Exhibition on Heat Treatment and Surface Engineering, HT and SE 2013; Chennai Trade CentreChennai; India; 16 May 2013 through 18 May 2013; Code 109410. 2013: 65-68.
- [4] Fauchais P.L, Heberlein J.V, Boulos M.I, *Combustion Spraying Systems, Thermal Spray Fundamentals*, Springer, 2014: 227-303.
- [5] Schoop M U. Apparatus for spraying molten metal and other fusible substances, U.S. Patent 1, 1915: 507-508.
- [6] Taylor T A, Bettridge D F, Tucker Jr R C. Coating composition having good corrosion and oxidation resistance, U.S. Patent 5,1995: 118-119.
- [7] Pierre Fauchais, J.V.R. Heberlein, M. Boulos. *Thermal Spray Fundamentals. From powder to part*, Springer, 2013: 7-20.
- [8] Davis J.R, *Handbook of thermal spray technology*, ASM international, 2004:3-13.
- [9] Pawlowski L, *The science and engineering of thermal spray coatings*, John Wiley & Sons, 2008: 35-42.
- [10] Ducos M, Durand J P. Thermal coatings in Europe: a business perspective[J]. *Journal of Thermal Spray Technology*, 2001, 10(3): 407.
- [11] Walser B. The importance of thermal spray for current and future applications in key industries[J]. *Spraytime*, 2004, 10(4): 1-7.
- [12] Herman H, Sampath S, McCune R. Thermal spray: current status and future trends[J]. *Mrs Bulletin*, 2000, 25(07): 17-25.
- [13] [http://www.upc.edu/sct/en/documents\\_equipament/d\\_324\\_id-804-2.pdf](http://www.upc.edu/sct/en/documents_equipament/d_324_id-804-2.pdf). (courtesy of Sulzer Metco [Switzerland] cited in 2016-May).
- [14] Bobzin K, Ernst F, Zwick J, et al. Thermal spraying of cylinder bores with the PTWA internal coating system[C]//ASME 2007 Internal Combustion Engine Division Fall Technical Conference. American Society of Mechanical Engineers, 2007: 697-704.
- [15] Fauchais P. Understanding plasma spraying[J]. *Journal of Physics D: Applied Physics*, 2004, 37(9): P86.
- [16] Boulos M I, Fauchais P, Pfender E. *Thermal Plasma-Fundamental and Applications-Vol. 1*[J]. 1994: 244-248.
- [17] Darut G, Liao H, Coddet C, et al. Steel coating application for engine block bores by Plasma Transferred Wire Arc spraying process[J]. *Surface and Coatings Technology*, 2015, 268: 115-122.

- [18] Bobzin K, Ernst F, Zwick J, et al. Coating bores of light metal engine blocks with a nanocomposite material using the plasma transferred wire arc thermal spray process[J]. *Journal of Thermal Spray Technology*, 2008, 17(3): 344-351.
- [19] Chow R, Decker T A, Gansert R V, et al. Properties of aluminum deposited by a HVOF process[J]. *Journal of thermal spray technology*, 2003, 12(2): 208-213.
- [20] Wang L. Erosion testing and surface preparation using abrasive water-jetting[J]. *Journal of materials engineering and performance*, 2004, 13(1): 103-106.
- [21] Bellman R, Levy A. Erosion mechanism in ductile metals[J]. *Wear*, 1981, 70(1): 1-27.
- [22] Griffiths B J, Gawne D T, Dong G. The erosion of steel surfaces by grit-blasting as a preparation for plasma spraying[J]. *Wear*, 1996, 194(1): 95-102.
- [23] ASTM C366 / C366M-11, Standard Test Methods for Measurement of Thickness of Sandwich Cores, ASTM International, West Conshohocken, PA, 2011, [www.astm.org](http://www.astm.org)
- [24] Pasandideh-Fard M, Pershin V, Chandra S, et al. Splat shapes in a thermal spray coating process: simulations and experiments[J]. *Journal of Thermal Spray Technology*, 2002, 11(2): 206-217.
- [25] Fauchais P, Vardelle A, Vardelle M, et al. Knowledge concerning splat formation: an invited review[J]. *Journal of Thermal Spray Technology*, 2004, 13(3): 337-360.
- [26] Scrivani A, Bardi U, Carrafiello L, et al. A comparative study of high velocity oxygen fuel, vacuum plasma spray and axial plasma spray for the deposition of CoNiCrAlY bond coat alloy[J]. *Journal of thermal spray technology*, 2003, 12(4): 504-507.
- [27] de Villiers Lovelock H L. Powder/processing/structure relationships in WC-Co thermal spray coatings: A review of the published literature[J]. *Journal of thermal spray technology*, 1998, 7(3): 357-373.
- [28] Berndt C C. Tensile adhesion testing methodology for thermally sprayed coatings[J]. *Journal of materials engineering*, 1990, 12(2): 151-158.
- [29] McMurchie D. Development of a 1080 steel plasma sprayed coating for slide/roll wear conditions[J]. 1996: 145
- [30] Henne R H, Bouyer E, Borck V, et al. Influence of anode nozzle and external torch contour on the quality of the atmospheric dc plasma spray process[J]. *New Surfaces for a New Millennium*, 2001: 471-478.
- [31] Schwenk A, Gruner H, Zimmermann S, et al. Improved nozzle design of de-Laval-type nozzles for the atmospheric plasma spraying[C]//ITSC 2004: International Thermal Spray Conference 2004: Advances in Technology and Application. 2004: 600-605.
- [32] Lin C K, Berndt C C. Measurement and analysis of adhesion strength for thermally sprayed coatings[J]. *Journal of Thermal Spray Technology*, 1994, 3(1): 75-104.
- [33] Sampath S, Jiang X Y, Matejicek J, et al. Substrate temperature effects on splat formation, microstructure development and properties of plasma sprayed coatings Part I: Case study for partially stabilized zirconia[J]. *Materials Science and Engineering: A*, 1999, 272(1): 181-188.
- [34] Lima C R C, Guilemany J M. Adhesion improvements of thermal barrier coatings with HVOF thermally sprayed bond coats[J]. *Surface and Coatings Technology*, 2007, 201(8): 4694-4701.

- [35] Zaat J H. A quarter of a century of plasma spraying[J]. Annual Review of Materials Science, 1983, 13(1): 9-42.
- [36] Lugschedier E, Kvernes I. Thermal barrier coatings: powder spray process and coating technology[J]. Materials engineering, 1999, 13: 267-306.
- [37] Tung S C, McMillan M L. Automotive tribology overview of current advances and challenges for the future[J]. Tribology International, 2004, 37(7): 517-536.
- [38] Edrisy A. Investigation of wear and scuffing behaviour of ferrous thermal spray coatings for aluminum engines[M]. 2004: 6-47.
- [39] Slattery B. Linerless Eutectic Al-Si Engine Wear: Microstructural Evolution[J]. 2009: 10-81
- [40] Woś P, Michalski J. Effect of initial cylinder liner honing surface roughness on aircraft piston engine performances[J]. Tribology letters, 2011, 41(3): 555-567.
- [41] ASTM G40-15, Standard Terminology Relating to Wear and Erosion, ASTM International, West Conshohocken, PA, 2015, [www.astm.org](http://www.astm.org)
- [42] Hutchings I M. Tribology: friction and wear of engineering materials[J]. 1992: 62-76.
- [43] Rabiei A, Mumm D R, Hutchinson J W, et al. Microstructure, deformation and cracking characteristics of thermal spray ferrous coatings[J]. Materials Science and Engineering: A, 1999, 269(1): 152-165.
- [44] Ashby M F, Lim S C. Wear-mechanism maps[J]. Scripta Metallurgica et Materialia, 1990, 24(5): 805-810.
- [45] So H, Yu D S, Chuang C Y. Formation and wear mechanism of tribo-oxides and the regime of oxidational wear of steel[J]. Wear, 2002, 253(9): 1004-1015.
- [46] Prasad B K. Sliding wear behaviour of a cast iron as affected by test environment and applied load[J]. Industrial Lubrication and Tribology, 2009, 61(3): 161-172.
- [47] L. Bianchi, F. Blein, P. Lucchese, M. Vardelle, A. Vardelle, P. Fauchais, ASM International, Materials Park, OH (United States), 1994: 569-574
- [48] Han W, Rybicki E F, Shadley J R. An improved specimen geometry for ASTM C633-79 to estimate bond strengths of thermal spray coatings[J]. Journal of Thermal Spray Technology, 1993, 2(2): 145-150.
- [49] <http://www.leekeegroup.com/eng/company/pdf/02.pdf> (cited in 2016-May)
- [50] Burton C L, Jones M K, Oglesby D L, et al. Failure Analysis of a Cast A380 Aluminum Alloy Casting Using a Microstructurally Based Fatigue Model[J]. TRANSACTIONS-AMERICAN FOUNDRYMENS SOCIETY, 2006, 114: 97.
- [51] Papadopoulos P, Priest M, Rainforth W M. Investigation of fundamental wear mechanisms at the piston ring and cylinder wall interface in internal combustion engines[J]. Proceedings of the Institution of Mechanical Engineers, Part J: Journal of Engineering Tribology, 2007, 221(3): 333-343.
- [52] ASTM E1920-03(2014), Standard Guide for Metallographic Preparation of Thermal Sprayed Coatings, ASTM International, West Conshohocken, PA, 2014, [www.astm.org](http://www.astm.org)
- [53] ASTM E2109-01(2014), Standard Test Methods for Determining Area Percentage Porosity in Thermal Sprayed Coatings, ASTM International, West Conshohocken, PA, 2014, [www.astm.org](http://www.astm.org)

- [54] ASTM E110-14, Standard Test Method for Rockwell and Brinell Hardness of Metallic Materials by Portable Hardness Testers, ASTM International, West Conshohocken, PA, 2014, [www.astm.org](http://www.astm.org)
- [55] Bairo F, Vitale-Brovarone C. Feasibility of glass–ceramic coatings on alumina prosthetic implants by airbrush spraying method[J]. *Ceramics International*, 2015, 41(2): 2150-2159.
- [56] <http://www.makeitfrom.com/compare/380.0-SC84B-A03800-Cast-Aluminum/Grey-Cast-Iron/> ( cited in 2016-May)
- [57] Barber G C, Lee J C, Ludema K C. Materials and surface finish effects in the breaking-in process of engines[J]. *Journal of engineering for gas turbines and power*, 1987, 109(4): 380-387.
- [58] Etsion I. State of the art in laser surface texturing[J]. *Journal of tribology*, 2005, 127(1): 248-253..
- [59] Henein N A. Time Dependent Wear and Its Mechanisms in Engine Cylinders[R]. WAYNE STATE UNIV DETROIT MI CENTER FOR AUTOMOTIVE RESEARCH, 1997: 34-77

## VITA AUCTORIS

NAME: Jianping Zou

PLACE OF BIRTH: Chengdu, China

DATE OF BIRTH: 1989

EDUCATION: Bachelor of Engineering,  
Material Science and Engineering  
Southwest Jiaotong University  
Chengdu, Sichuan, China  
2013

Master of Applied Science  
Engineering Materials  
University of Windsor  
Windsor, ON, Canada  
2016